



저작자표시-비영리-변경금지 2.0 대한민국

이용자는 아래의 조건을 따르는 경우에 한하여 자유롭게

- 이 저작물을 복제, 배포, 전송, 전시, 공연 및 방송할 수 있습니다.

다음과 같은 조건을 따라야 합니다:



저작자표시. 귀하는 원저작자를 표시하여야 합니다.



비영리. 귀하는 이 저작물을 영리 목적으로 이용할 수 없습니다.



변경금지. 귀하는 이 저작물을 개작, 변형 또는 가공할 수 없습니다.

- 귀하는, 이 저작물의 재이용이나 배포의 경우, 이 저작물에 적용된 이용허락조건을 명확하게 나타내어야 합니다.
- 저작권자로부터 별도의 허가를 받으면 이러한 조건들은 적용되지 않습니다.

저작권법에 따른 이용자의 권리는 위의 내용에 의하여 영향을 받지 않습니다.

이것은 [이용허락규약\(Legal Code\)](#)을 이해하기 쉽게 요약한 것입니다.

[Disclaimer](#)

공학박사 학위논문

**Synthesis and Applications of
Two-Dimensional Nanostructures of
Molybdenum Disulfide and
Tin Selenide**

이황화 몰리브데넘 및 셀레늄화 주석의
이차원 나노구조 합성 및 응용

2020년 2월

서울대학교 대학원

화학생물공학부

채수인

Synthesis and Applications of Two-Dimensional Nanostructures of Molybdenum Disulfide and Tin Selenide

지도 교수 현택환

이 논문을 공학박사 학위논문으로 제출함
2020 년 1 월

서울대학교 대학원
화학생물공학부
채수인

채수인의 공학박사 학위논문을 인준함
2020 년 1 월

위원장	성영은	
부위원장	현택환	
위원	김대형	
위원	정인	
위원	손재성	

Abstract

Synthesis and Applications of Two-Dimensional Nanostructures of Molybdenum Disulfide and Tin Selenide

Sue In Chae

School of Chemical and Biological Engineering

The Graduate School

Seoul National University

Two-dimensional nanomaterials have attracted tremendous interest from researchers in various fields, due to their unique properties. Recently, studies on the synthesis of two-dimensional semiconductor nanomaterials using colloidal chemistry have been reported. This dissertation demonstrates the large-scale colloidal chemical synthesis and applications of two-dimensional nanostructures of molybdenum disulfide (MoS_2) and tin selenide (SnSe).

Firstly, I present the large-scale synthesis of uniform-sized MoS₂ nanosheets using colloidal chemistry and their integration to fabricate flexible resistance random access memory (RRAM) array. The synthesized MoS₂ nanosheets exhibit much narrower size and thickness distributions than the exfoliated MoS₂. In addition, the colloidal stability of the synthesized MoS₂ nanosheets and the high reproducibility of the synthetic method enable the solution-processed fabrication of the memory device. The RRAM using the synthesized MoS₂ nanosheets shows a ~10,000 times higher on/off ratio than that based on exfoliated MoS₂. Furthermore, the good uniformity of the colloidal MoS₂ nanosheets allows the fabrication of the wafer-scale flexible RRAM array.

Secondly, I demonstrate the synthesis, surface treatment, and thermoelectric characterization of SnSe nanoplates with dislocations. A simple solution-phase synthesis enables the large-scale production of SnSe nanoplates with many dislocations. Transmission electron microscopy reveals that a high density of dislocations retains even after consolidation of the nanoplates by spark plasma sintering. Post-treatment with ammonia solution can effectively remove the impurities such as iodide and long-chain organic ligands and undesired oxides from the

surface of SnSe nanolates, leading to enhancement in electrical conductivity of the consolidated pellet along with an increase in hole concentration. Cooperated with ultralow lattice thermal conductivity ($\sim 0.23 \text{ W m}^{-1} \text{ K}^{-1}$) of the unique nanostructured bulk materials, a high thermoelectric figure of merit ZT of ~ 1.1 at 873 K is achieved. This study will offer new opportunities for the controlled synthesis of defective nanomaterials and facilitate the understanding of the surface chemistry, contributing to better performance of the electronic devices.

Keywords: MoS₂, nanosheets, RRAM, SnSe, nanoplates, dislocations, surface treatment, thermoelectric properties.

Student Number: 2012-23981

Contents

Chapter 1 Review on Recent Advances in the Nanostructured Materials for Thermoelectric applications	1
1.1 Introduction.....	1
1.2 Transport Mechanisms in Nanostructured Materials	10
1.2.1 Quantum Confinement Effect	10
1.2.2 Carrier filtering.....	15
1.2.3 Nanostructuring.....	19
1.3 Strategies by the Use of Nanomaterials for Enhancement on Thermoelectric Properties.....	24
1.3.1 Surface Treatment	28
1.3.2 Nanocrystals Blending	34
1.3.3 Heterostructured Nanocrystals	40
1.4 Dissertation Overview	44
1.5 References.....	46

Chapter 2 Synthesis of Uniform-Sized Molybdenum

Disulfide Nanosheets and Applications for Wafer-scale Nonvolatile Memory	53
2.1 Introduction.....	53
2.2 Experimental Section.....	56
2.3 Results and Discussion	62
2.4 Conclusion	96
2.5 References.....	97
Chapter 3 Synthesis and Surface Treatment of SnSe Nanoplates for Thermoelectric Application.....	106
3.1 Introduction.....	106
3.2 Experimental Section.....	111
3.3 Results and Discussion	117
3.4 Conclusion	156
3.5 References.....	157
Bibliography	163
국문 초록 (Abstract in Korean)	168

List of Tables

Table 3.1	Fitting results of O1s XPS spectra of the SnSe nanoplates	135
Table 3.2	Chemical composition of the SnSe nanoplates, NH ₃ -SnSe nanoplates, and SPSed samples	137

List of Figures

Figure 1.1	Schematic illustration for thermoelectric module.....	6
Figure 1.2	The calculated ZT value as a function of characteristic length for 1D and 2D Bi_2Te_3	7
Figure 1.3	Various nanomaterials synthesized by colloidal chemistry. (PbS and PbTe nanocrystals, Bi_2Te_3 nanoplates, and Bi_2Te_3 nanotubes).....	8
Figure 1.4	Schematic band structures as a function of size and dimension in metal and semiconductor	13
Figure 1.5	The relationship of the Seebeck coefficient and the size of PbSe nanocrystals	14
Figure 1.6	Carrier filtering effect in Ag/oxide/ Sb_2Te_3 -Te film.....	18
Figure 1.7	Schematic illustration of electrons and phonons transport .	22
Figure 1.8	TEM analysis and thermal conductivity of nanostructured $\text{Bi}_x\text{Sb}_{2-x}\text{Te}_3$	23
Figure 1.9	Schematic illustration of the relation between the carrier concentration and the ZT value	26
Figure 1.10	Models of the proposed doping mechanism in semiconductor nanocrystals	27

Figure 1.11	Inorganic nanocrystals dispersed in polar solvents after treatment with chalcogenidometallates ligand ($\text{Sn}_2\text{S}_6^{4-}$)	32
Figure 1.12	TEM analysis of off-stoichiometric $\text{K}_{0.06}\text{Bi}_2\text{Te}_{3.18}$	33
Figure 1.13	ZT value for Ag-PbS nanocomposites	39
Figure 2.1	Schematic illustration for the synthesis of colloidal MoS_2 nanosheets.....	64
Figure 2.2	TEM image of the synthesized MoS_2 nanosheets.....	65
Figure 2.3	XRD, Raman, and XPS anlysis of the synthesized MoS_2 nanosheets.....	66
Figure 2.4	Observation of the growth of MoS_2 nanosheets	68
Figure 2.5	Effect of solvent and sulfur precursor in the synthesis of the MoS_2 nanosheets.....	69
Figure 2.6	Colloidal stability of the MoS_2 nanosheets dispersed in solution.....	70
Figure 2.7	Distribution of diameter and number of layers for the synthesized and exfoliated MoS_2 nanosheets.	73
Figure 2.8	Fundamental properties of the synthesized MoS_2 nanosheets produced in a scaled-up batch.....	74
Figure 2.9	Resistive switching of the MoS_2 - MoO_x heterostructure.	78
Figure 2.10	Fabrication process for the MoS_2 RRAM device	79

Figure 2.11	TEM image of the exfoliated MoS ₂ RRAM and I-V characteristics of the RRAM device in log scale	80
Figure 2.12	Depth profiles of the Mo ⁶⁺ population and retention test in the MoS ₂ RRAM device	82
Figure 2.13	Characterization of the conducting filaments through CAFM analysis.....	84
Figure 2.14	An image of wafer-scale MoS ₂ RRAM arrays	87
Figure 2.15	Raman and XPS analysis at different five points on MoS ₂ -MoO _x heterostructure assembled by the spray-coating on a Si wafer	88
Figure 2.16	Image for the MoS ₂ -MoO _x layer patterned by standard photolithography and RIE (CF ₄ plasma)	89
Figure 2.17	Film thickness of the spray-coated MoS ₂ -MoO _x heterostructure measured at five different regions <i>via</i> Atomic force microscopy (AFM)	90
Figure 2.18	The cumulative probability of the resistance and switching voltage for the RRAM devices	91
Figure 2.19	Cumulative probability plot of the switching voltage and resistance from the synthesized MoS ₂ RRAM devices and crossbar arrays with three different cell sizes.....	92

Figure 2.20	Bending test and a photograph of the flexible MoS ₂ RRAM arrays formed on a PET substrate	94
Figure 2.21	Transfer process of the MoS ₂ array from the mother substrate onto skin using a thermal release tape	95
Figure 3.1	TEM image and XRD analysis of SnSe nanoplates	119
Figure 3.2	TEM analysis of dislocations at grain boundary of SnSe nanoplates	122
Figure 3.3	TEM images of dislocations inside SnSe nanoplates	123
Figure 3.4	Time-dependent TEM observation of SnSe nanoplates....	126
Figure 3.5	TEM analysis of SnSe nanoplates in the early growth stage	127
Figure 3.6	FTIR spectra and elemental analysis of SnSe nanoplates and NH ₃ -SnSe nanoplates.....	130
Figure 3.7	TGA and XPS spectra of SnSe nanoplates and NH ₃ -SnSe nanoplates	131
Figure 3.8	XPS and Raman spectra of supernatant after surface treatment and Sn concentration of SnO, SnO ₂ , and SnSe nanoplates in ammonia solution.....	136
Figure 3.9	STEM images and elemental mapping of SnSe and NH ₃ -SnSe nanoplates	139

Figure 3.10	XRD patterns of SnSe and NH ₃ -SnSe nanoplates	140
Figure 3.11	A photograph of NH ₃ -SnSe pellet.....	142
Figure 3.12	SEM images of sintered SnSe.....	143
Figure 3.13	XRD patterns of SPSed SnSe and NH ₃ -SnSe.....	144
Figure 3.14	FTIR spectrum of SPSed NH ₃ -SnSe.....	145
Figure 3.15	Atomic-resolution scanning TEM image of the cross section of SPSed NH ₃ -SnSe	147
Figure 3.16	Cross-sectional TEM images of the SPSed NH ₃ -SnSe showing mesoscale grains and dislocations.....	148
Figure 3.17	XRD patterns and temperature-dependent thermoelectric properties of SPSed NH ₃ -SnSe depending on measurement direction	152
Figure 3.18	Temperature-dependent thermoelectric properties of SPSed SnSe and NH ₃ -SnSe.....	153
Figure 3.19	Hole concentration and electrical conductivity of SPSed SnSe and NH ₃ -SnSe at room temperature.....	154
Figure 3.20	XPS spectra of SPSed SnSe and NH ₃ -SnSe	155

Chapter 1. Review on Recent Advances in the Nanostructured Materials for Thermoelectric applications

1.1 Introduction

The foundation of modern technologies has been established on the fossil fuels that produce air pollutants and damage earth environments. To alleviate the issues, the development for the sustainable energy source has been globally progressed. In this respect, the thermoelectric technology is a promising energy converter that transforms heat to electrical energy and vice versa.^[1a-h] More than 60% of energy produced from various sources, including fossil fuels, has been dissipated as heat.^[1i] Therefore, the recovery of waste heat through thermoelectric devices would increase the efficiency of the energy systems. Further, thermoelectric generators are reliable and environmentally clean because they have no moving parts and noise and do not release toxic gases. In addition, thermoelectric devices that provide targeted cooling in many devices are advantageous in that current cooling systems are bulky and

inefficient and typically cool the entire device parts rather than local hot spots.^[1j,k] Despite the advantages of thermoelectric technology, it is difficult to use it into the industry owing to the poor efficiency of the current thermoelectric materials.

The efficiency of the thermoelectric device depends on the active materials, size, configuration, and contacts.^[1e] Among them, the device efficiency is strongly dependent on the properties of thermoelectric materials, for which the semiconducting materials are typically used (Fig. 1.1). The maximum power-generation efficiency of a thermoelectric material, η , is thermodynamically limited by the Carnot efficiency and η is defined as

$$\eta = \frac{T_{hot} - T_{cold}}{T_{hot}} \cdot \frac{\sqrt{1 + ZT_{avg}} - 1}{\sqrt{1 + ZT_{avg}} + (T_{cold}/T_{hot})} \quad (\text{eq. 1})$$

where T_{hot} and T_{cold} are the temperature of hot and cold end of the thermoelectric module, respectively, and ZT is the dimensionless figure of merit a thermoelectric material. The ZT is defined as

$$ZT = \frac{S^2 \sigma T}{\kappa_{tot}} \quad (\text{eq. 2})$$

where S is the Seebeck coefficient, σ is the electrical conductivity, $S^2 \sigma$ is the power factor (PF), T is the absolute temperature, and κ_{tot} is the total thermal conductivity. Two approaches to improve the thermoelectric

performance include either the increase of power factor or the decrease of thermal conductivity. However, the strong interrelationship between the material properties makes the improvement of efficiency very difficult. For example, the Seebeck coefficient of a degenerate semiconductor depends on the carrier concentration and the effective mass of carriers, as shown in eq. 3,

$$S = \frac{8\pi^2 k_B^2}{3eh^2} m^* T \left(\frac{\pi}{3n} \right)^{2/3} \quad (\text{eq. 3})$$

where n is the carrier concentration, k_B is the Boltzmann constant, h is the Plank constant, and m^* is the effective mass of carriers. The decrease of carrier concentration increases the Seebeck coefficient but decreases the electrical conductivity, as shown in eq. 4,

$$\sigma = ne\mu \quad (\text{eq. 4})$$

where e is the electric charge and μ is the carrier mobility. Furthermore, the strategies to increase the electrical conductivity cause the increase of thermal conductivity because the thermal conductivity is directly connected to the electrical conductivity by the Wiedemann–Franz law, as show in eq. 5,

$$\kappa_{tot} = \kappa_{elec} + \kappa_{latt} \quad \text{and} \quad \kappa_{elec} = L\sigma T \quad (\text{eq. 5})$$

where κ_{elec} and κ_{latt} are the thermal conductivities contributed by the carrier transports and the lattice vibrations, respectively, and L is the

Lorenz number. As a result, it is very challenging to enhance the thermoelectric performance.

In the 1990s, the concept “low dimensionality” has received a great attention as an innovative strategy proposed by Hicks and Dresselhaus to improve the thermoelectric efficiency.^[2a,b] Prior to their theoretical predictions, thermoelectric researches had been stagnant due to the aforementioned difficulties in improving the thermoelectric performance, but the situation changed. They suggested that reducing the dimensionality of a semiconductor can increase the density of electronic states near the Fermi level, thereby improving the power factor (Fig. 1.2). In addition, the thermal conductivity can be effectively reduced by scattering the phonons at a high density of interfaces in the nanostructured materials. Namely, decoupling the entangled physical quantities in the nanostructured materials is expected to achieve higher thermoelectric performance. Experimental evidences in the superlattices grown by molecular beam epitaxy (MBE) have supported the theoretical expectations: Venkatasubramanian group observed a high ZT of ~ 2.4 in $\text{Bi}_2\text{Te}_3/\text{Sb}_2\text{Te}_3$ superlattices,^[2c] and Harman group achieved ZT of ~ 1.6 in $\text{PbSeTe}/\text{PbTe}$ superlattices.^[2d] However, this fabrication technique is complicated and expensive, making it difficult to apply in the large-scale

industry. In order to solve the problem, various preparation methods have been developed. For example, a physical approach such as ball milling has been employed to create the nanoscale materials in large quantities.^[3] However, ball-milling process is disadvantageous to produce the uniform and complex nanostructured materials.

Colloidal chemical synthesis is an effective method to prepare the high-quality nanomaterials with a tunable structure and composition.^[4a-c] This protocol is capable of a large-scale production of nanoparticles. In addition, the preparation of multicomponent nanoparticles as well as single-component nanoparticles is feasible through the advanced nanochemistry. The structural and compositional complexity of the nanoparticles has been necessitated for the optimization of the performance in a wide range of applications (Fig. 1.3). The nanostructured materials are prepared by assembling and sintering the colloidal nanoparticles into the form of either a film or a bulk.^[4d] In the next chapter, the representative transport mechanisms working in the nanostructured materials will be reviewed. Then, several strategies by the use of colloidal nanoparticles for thermoelectric applications will be covered.

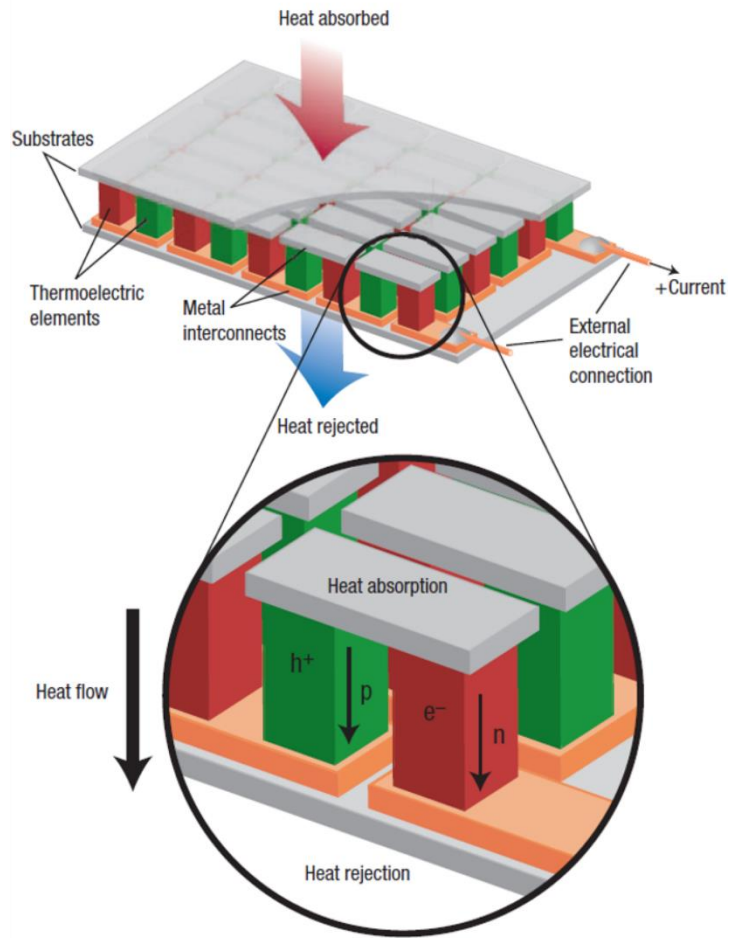


Figure 1.1 Thermoelectric module made up of p- and n-type semiconductor blocks and metal junctions. Carriers are thermally diffused from a top to a bottom electrode during power generation whereas external power supply drives both carriers and heat flow during cooling. (from Ref. [1f] Snyder, G. J.; Toberer, E. S. *Nat. Mater.* **2008**, *7*, 105.)

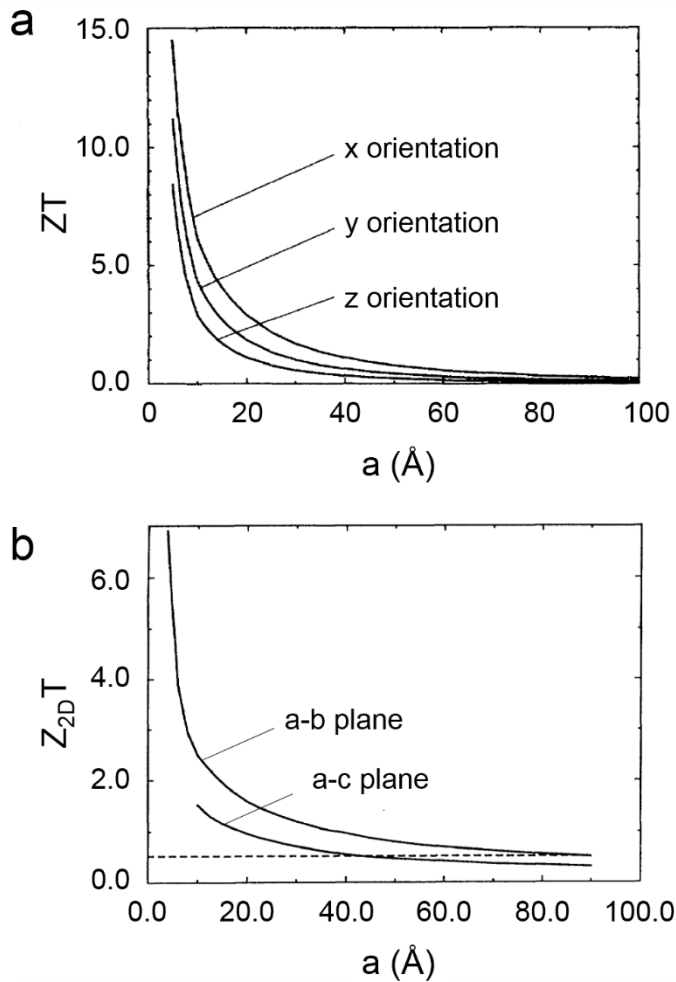


Figure 1.2 The calculated ZT value as a function of characteristic length for (a) 1D and (b) 2D Bi_2Te_3 . (from Ref. [2a] Hicks, L. D.; Dresselhaus, M. S. *Phys. Rev. B* **1993**, *47*, 12727.; [2b] Hicks, L. D.; Dresselhaus, M. S. *Phys. Rev. B* **1993**, *47*, 16631.)

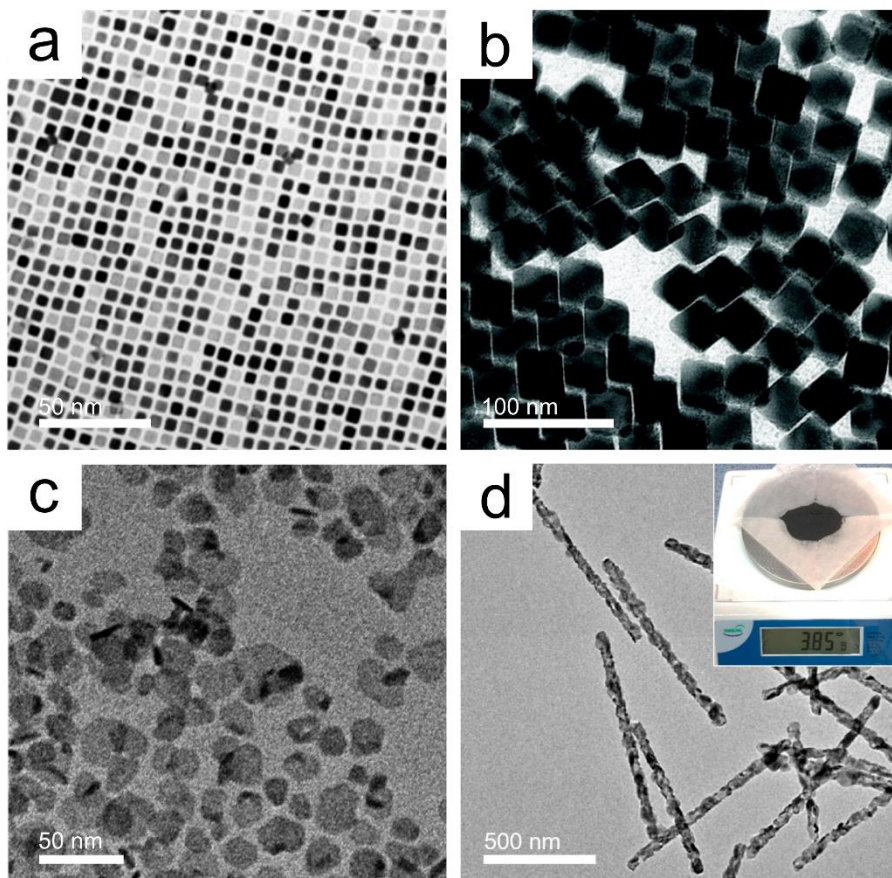


Figure 1.3 Various nanomaterials synthesized by colloidal chemistry. TEM images of (a) PbS and (b) PbTe nanocrystals, (c) Bi₂Te₃ nanoplates, and (d) Bi₂Te₃ nanotubes. The photo demonstrating the large-scale production of Bi₂Te₃ nanotubes is shown in the inset. (from Ref. [8a] Ibanez, M.; Korkosz, R. J.; Luo, Z.; Riba, P.; Cadavid, D.; Ortega, S.; Cabot, A.; Kanatzidis, M. G. *J. Am. Chem. Soc.* **2015**, *137*, 4046.; [7e]

Scheele, M.; Oeschler, N.; Veremchuk, I.; Peters, S. O.; Littig, A.; Kornowski, A.; Klinke, C.; Weller, *ACS Nano* **2011**, *5*, 8541.; [6d] Son, J. S.; Choi, M. K.; Han, M. K.; Park, K.; Kim, J. Y.; Lim, S. J.; Oh, M.; Kuk, Y.; Park, C.; Kim, S. J.; Hyeon, T. *Nano Lett.* **2012**, *12*, 640.; [8f] Park, K.; Ahn, K.; Cha, J.; Lee, S.; Chae, S. I.; Cho, S. P.; Ryee, S.; Im, J.; Lee, J.; Park, S. D.; Han, M. J.; Chung, I.; Hyeon, T. *J. Am. Chem. Soc.* **2016**, *138*, 14458.)

1.2 Transport Mechanisms in Nanostructured Materials

Understanding the charge and thermal transport in the nanostructured materials is essential to control and optimize the thermoelectric properties. Nanostructured materials have unique properties because of the nanoscale structural elements and a high density of interfaces. This chapter overviews the fundamental transport mechanisms that has been observed in the nanostructured materials.

1.2.1 Quantum Confinement Effect

In the nanoscale regime, the material properties of the semiconductor including electrical transport are different from those of bulk phase. The electrical and thermal transport is strongly related to the band structure of the material, and the semiconductor nanocrystals have a different band structure from that of bulk but similar to that of atoms or molecules.^[4e] While the bulk solids have the continuous bands, which consist of numerous energy levels, the semiconductor nanocrystals have discrete energy states because of the decreased overlap of the energy states. The spacing between the energy levels of the nanocrystals cannot be negligible and the electrons or holes are confined in the quantized levels.

Furthermore, the dimensionality of nanocrystals influences the band structure, and the density of states depending on the dimensionality is shown in Figure 1.4. Based on the simple calculation by a particle-in-a-box model in quantum mechanics, the parabolic bands for three-dimensional solids are separated into discrete states in zero-dimensional materials. Due to the quantum confinement effect, the nanocrystals with the sharply-peaked density of electronic states have been predicted to maximize the thermoelectric properties.^[2e] Linke group anticipated the high thermoelectric efficiencies in the low-dimensional materials with a delta-like density of states.^[2f,g] Recently, the electronic efficiency of a device composed of the InP/InAs heterostructured nanowires has been experimentally observed to exceed 70% of Carnot efficiency near 2 K.^[2h]

Talapin group revealed that the Seebeck coefficient is tunable by controlling the size of the nanocrystals. PbSe nanocrystals were used as a model system, and the Seebeck coefficient of the nanocrystals was measured on the film by coating the nanocrystals.^[2i] Figure 1.5 shows the dependence of the Seebeck coefficient on the nanocrystal size. As the size of PbSe nanocrystals decreases from 8.6 nm to 4.8 nm, the Seebeck coefficient increases from 700 to 1150 $\mu\text{V}/\text{K}$ at room temperature. The Seebeck coefficients of the nanocrystals are significantly higher than that

of bulk PbSe (400–600 $\mu\text{V/K}$) with comparable carrier concentrations. The sharp density of states in the PbSe nanocrystals contributes to the enhancement in the Seebeck coefficient. The Seebeck coefficient is approximately proportional to the difference between the average carrier energy and the Fermi level. The size-dependent band gap explains the size-dependent Seebeck coefficient in the nanocrystals. Because of the quantum confinement effect, as the size decreases, the band gap of the nanocrystals increases, and the valence band edge shifts away from Fermi level, which causes large spacing between the Fermi level and the average carrier energy. Therefore, as the size of nanocrystals decreases, the Seebeck coefficient increases. This also explains the decrease of carrier concentration with negligible variations in the mobility of the small PbSe nanocrystals.

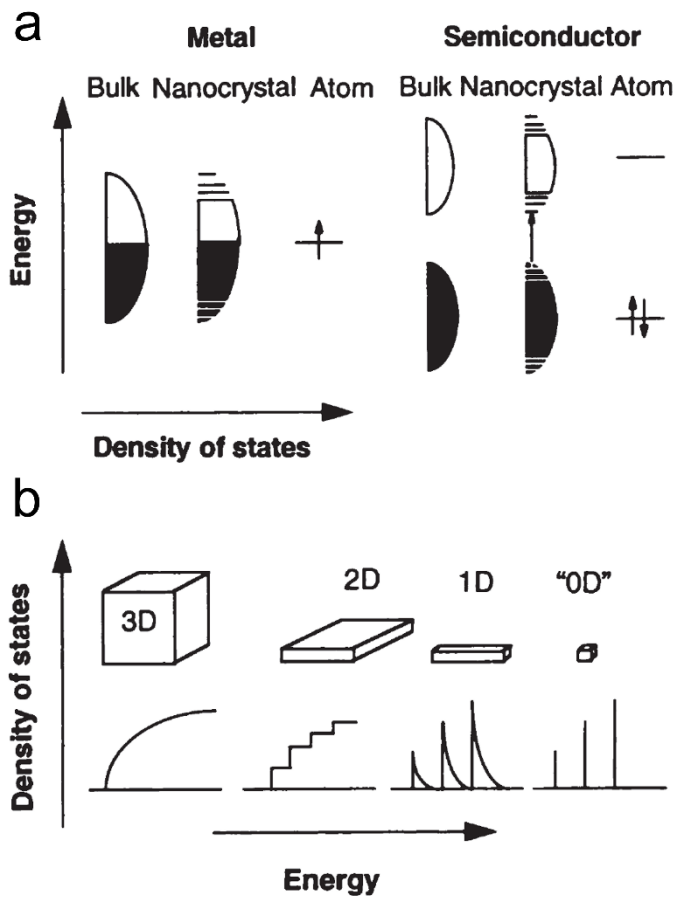


Figure 1.4 Schematic illustration of (a) band structures in metal and semiconductor in various size regime and (b) density of states dependent on the dimensions in semiconductors. (from Ref. [4e] Alivisatos, A. P. *Science* **1996**, 271, 933.)

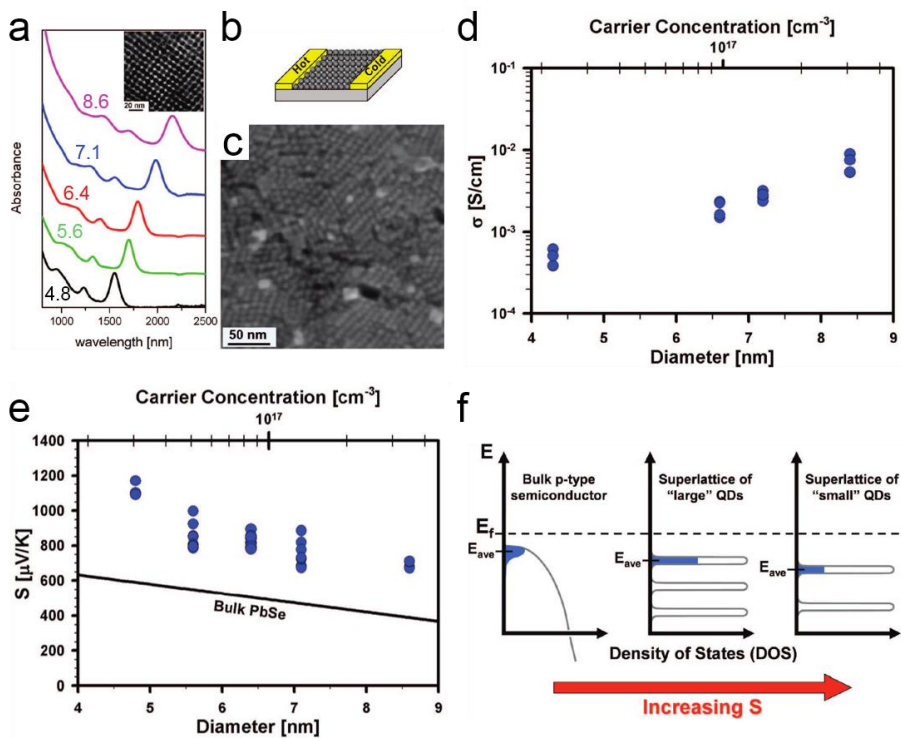


Figure 1.5 (a) Absorption spectra of PbSe nanocrystals with different size. (b) Schematic illustration and (c) TEM image for the PbSe nanocrystals film. (d) Electrical conductivity and (e) Seebeck coefficient of PbSe nanocrystals film as a function of nanocrystal size. (f) Schematic illustration to explain the size dependence of Seebeck coefficient in the PbSe nanocrystals. (from Ref. [2i] Wang, R. Y.; Feser, J. P.; Lee, J. S.; Talpin, D. V.; Segalman, R.; Majumdar, A. *Nano Lett.* **2008**, *8*, 2283.)

1.2.2 Carrier filtering

Because the density of interfaces between grains increases as the grain size decreases, the interfaces are heavily present in the nanostructured materials. The charge carriers interact with the interfaces, *i.e.* scattering process, and their behaviors are strongly influenced in the nanostructured materials. Due to the decrease of mobility by carrier scattering at the interface, a high density of interfaces is regarded as a detrimental structure for the high electrical conductivity. However, the interface plays a positive role in improving the Seebeck coefficient by filtering the low-energy carriers.^[5a] The carriers with sufficiently high energy can overcome the energy barriers at the interface and continue their motion, which is a kind of the thermionic emission. Namely, low-energy carriers are filtered out so that they do not contribute to the electrical conduction. The carrier filtering results in the increase of the average energy per carrier, which contributes to the enhancement on the Seebeck coefficient. A. J. Minnich calculated a function of the Seebeck coefficient distribution as a carrier energy in a heavily doped n-type $\text{Si}_{80}\text{Ge}_{20}$ and explained that low-energy electrons damage the Seebeck coefficient.^[1d] Using the carrier filtering concept, increasing the Seebeck coefficient is possible, but the decrease of electrical conductivity is inevitable in the

case of single-phase materials. However, because this concept can be applied in the multiphase materials, the adequate selection among candidate materials enables the enhancement on both the Seebeck coefficient and the electrical conductivity.

A wide range of material combinations such as metal-semiconductor and semiconductor-semiconductor have been investigated to achieve the filtering effect. For example, $\text{In}_{0.53}\text{Ga}_{0.47}\text{As}/\text{In}_{0.53}\text{Ga}_{0.28}\text{Al}_{0.19}\text{As}$ films grown by molecular beam epitaxy system exhibits the larger cross-plane Seebeck coefficient than the in-plane Seebeck coefficient, indicating the carrier filtering effect.^[5a] The nanocomposites, where the nanoparticles are embedded in the semiconducting host, show similar result. The Pt- Sb_2Te_3 film simply prepared *via* solution process exhibits the larger Seebeck coefficient than Sb_2Te_3 film ($167 \mu\text{V K}^{-1}$ for Pt- Sb_2Te_3 and $124 \mu\text{V K}^{-1}$ for Sb_2Te_3 at room temperature).^[5b] Similar result was reported in $\text{Ag}_x\text{Te}_y\text{-Sb}_2\text{Te}_3$ film, resulting in the 50% enhancement in power factor ($\sim 2 \mu\text{W cm}^{-1} \text{K}^{-2}$ at $150 \text{ }^\circ\text{C}$).^[5c] Galen D. Stucky group performed the theoretical and experimental demonstration of a filtering effect in thermally stable Ag/oxide/ Sb_2Te_3 -Te films (Fig. 1.6).^[5d] Coating the Ag nanoparticles in a thin oxide layer ($\sim 3 \text{ nm}$) prevents Ag atoms from alloying with Te during annealing, thereby reducing the unwanted

doping effect by Ag. Pisarenko plot clearly shows the increase of the Seebeck coefficient in Ag/oxide/Sb₂Te₃-Te films. The theoretical calculation suggests that the band offset at the interface between Ag nanoparticles and Sb₂Te₃ matrix is ~0.2 eV for filtering the hot carriers.

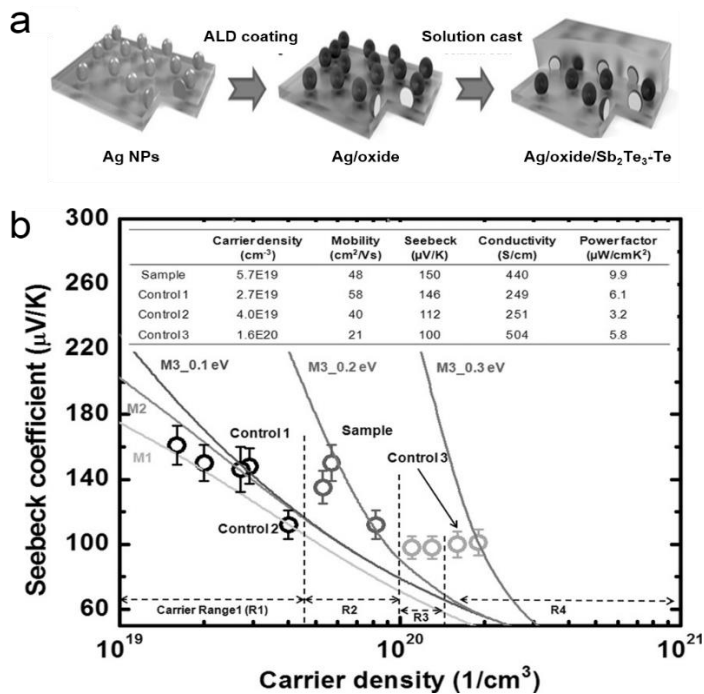


Figure 1.6 (a) Schematic illustration of the synthetic procedure for Ag/oxide/Sb₂Te₃-Te. (b) Pisarenko plot at room temperature. Control 1: Sb₂Te₃-Te (same process without Ag and oxide), Control 3: Ag/Sb₂Te₃-Te (same process without oxide). Control 2: Sb₂Te₃-Te with conversional Ag doping. The curve shows the calculated Seebeck coefficient; M1: without ionized scattering strength, M2: with ionized scattering strength, and M3_x eV: carrier filtering with a cut-off potential of x eV. (from Ref. [5d] Zhang, Y.; Bahk, J. H.; Lee, J.; Birkel, C. S.; Snedaker, M. L.; Liu, D.; Zeng, H.; Moskovits, M.; Shakouri, A.; Stucky, G. D. *Adv. Mater.* **2014**, *26*, 2755.)

1.2.3 Nanostructuring

The biggest benefit in the nanostructured materials is the reduction in the lattice thermal conductivity.^[1d] High-density interfaces not only scatter charge carriers but also hinder the thermal transport. The total thermal conductivity is composed of the electronic thermal conductivity and the lattice thermal conductivity. While the electronic thermal conductivity is strongly related to the electrical conductivity by Wiedemann–Franz law (eq. 5), the lattice thermal conductivity is not influenced by charge transport but phonon transport. It is necessary to know “phonons” to understand the thermal transport in a material. A phonon is a quantum mechanical concept to describe the vibrational motion of a lattice composed of atoms or molecules in either solid or liquid.^[6a] The phonons have a wavelength spectrum, and the degree to which the phonon contributes to lattice thermal conductivity differs depending on the wavelength of the phonon. Because the energy of the phonons affects the way of interaction with the structural elements in the material, engineering the structural elements allows a dramatic reduction of the lattice thermal conductivity. For example, the short-wavelength phonons are strongly scattered by the impurity atoms in the alloyed material, but medium- and long-wavelength phonons are less affected.

Medium- and long-wavelength phonons are mainly scattered at the interface (Fig. 1.7). Therefore, producing a high-density interface *via* nanostructuring is an effective strategy for reducing the lattice thermal conductivity.

The effective decrease of the thermal conductivity has been found in various nanostructured materials. Zhifeng Ren group prepared the p-type nanostructured $\text{Bi}_{0.5}\text{Sb}_{1.5}\text{Te}_3$ by hot-pressing the ball-milled $\text{Bi}_{0.5}\text{Sb}_{1.5}\text{Te}_3$. The lattice thermal conductivity of the nanostructured $\text{Bi}_{0.5}\text{Sb}_{1.5}\text{Te}_3$ is decreased by half compared to that of the ingot. Cross-sectional transmission electron microscope image clearly shows the nanosized grains, nanodots, and Te precipitates (Fig. 1.8).^[3] Kanatzidis group reported the high ZT of ~ 2.2 (800 K) in $\text{AgPb}_{18}\text{SbTe}_{20}$ due to the low thermal conductivity, which is related to the nanostructure of a Sb, Ag-rich phase in a PbTe matrix.^[6b]

The nanostructured bulk materials produced from chemically synthesized nanomaterials also have shown similar results. The synthesized $\text{Sb}_{(2-x)}\text{Bi}_x\text{Te}_3$ nanoplatelets were sintered into the nanostructured bulk materials, which retains the nanostructures, thereby showing very polycrystalline properties and a high density of grain boundaries. The lattice thermal conductivity of the nanostructured $\text{Sb}_{(2-x)}$

x) Bi_xTe_3 is $0.31 \text{ W m}^{-1} \text{ K}^{-1}$ at 300 K, which is much lower than the bulk $\text{Sb}_{1.5}\text{Bi}_{0.5}\text{Te}_3$ ingot.^[6c] The nanostructured Bi_2Te_3 produced from ultrathin Bi_2Te_3 nanoplates also shows the lower thermal conductivity than the bulk Bi_2Te_3 . In these nanostructured bulks, sintering temperature influences the electrical transport *via* the interface effects proposed as a potential barrier and a doping effect. Therefore, the interface (grain size and interface property) must be carefully designed to finely control both the electrical and thermal transport.^[6d] Regardless of the morphology of building blocks, the nanostructured Bi_2Te_3 obtained from ultrathin Bi_2Te_3 nanowires similarly exhibits a significant reduction of the thermal conductivity.^[6e]

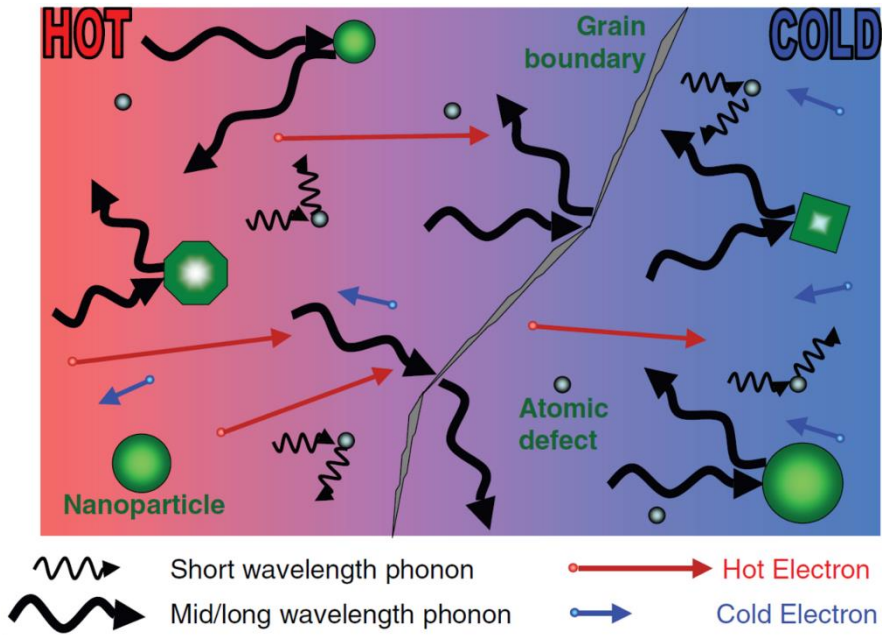


Figure 1.7 Schematic illustration for scattering of electrons and phonons. Phonons are scattered by various defects (grain boundary, nanoparticle, and atomic impurity) more than electrons. (from Ref. [1a] Vineis, C. J.; Shakouri, A.; Majumdar, A.; Kanatzidis, M. G. *Adv. Mater.* **2010**, *22*, 3970.)

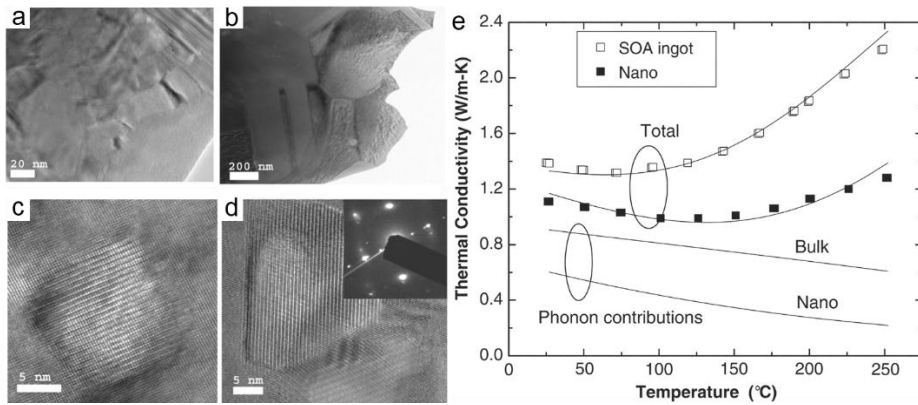


Figure 1.8 Low-magnification TEM images showing (a) nanograins and (b) larger grains. High-magnification TEM images showing (c) nanodots and (d) Te precipitates. (e) Thermal conductivity of $\text{Bi}_x\text{Sb}_{2-x}\text{Te}_3$ nanostructured materials compared with that of the ingot. (from Ref. [3] Poudel, B.; Hao, Q.; Ma, Y.; Lan, Y.; Minnich, A.; Yu, B.; Yan, X.; Wang, D.; Muto, A.; Vashaee, D.; Chen, X.; Liu, J.; Dresselhaus, M. S.; Chen, G.; Ren, Z. *Science* **2008**, 320, 634.)

1.3. Strategies by the Use of Nanomaterials for Enhancement on Thermoelectric Properties

To produce the best thermoelectric performance, first of all, the carrier concentration needs to be optimized (Fig.1.9).^[1f] In the case of a bulk phase, doping is a common method to control the carrier concentration. The nanostructured bulk materials are fabricated by assembling or sintering the various nanomaterials and used as the thermoelectric materials.^[4d] Although many processing parameters during fabrication of the nanomaterials into the nanostructured bulk materials affect the properties of the nanostructured bulk materials, the properties of the nanomaterials are closely related to those of the nanostructured materials. Therefore, it is intuitive to modify the carrier concentration of the nanocrystals for optimization of that of the nanostructured bulk materials. However, unlike the bulk phase, though there have been a few successful syntheses of the doped nanocrystals, doping the nanoparticles is generally considered difficult to achieve (Fig. 1.10).^[4f,g] As the synthesis of nanocrystals is performed at the low temperature, kinetics dominates the growth of the nanocrystals. Therefore, the introduction of dopants inside the lattice of nanocrystal is possible only when the growth rate of dopant and host is well balanced during the growth of nanocrystals.

Because the synthesis of doped nanocrystals is in an early stage, alternative approaches have enabled to tune the properties in the nanostructured bulk materials. These approaches include chemically treating the nanocrystal surface, blending different nanocrystals, and synthesizing heterostructured nanocrystals. In this chapter, we will review the strategies by the use of the nanomaterials to optimize thermoelectric properties in nanostructured bulk materials.

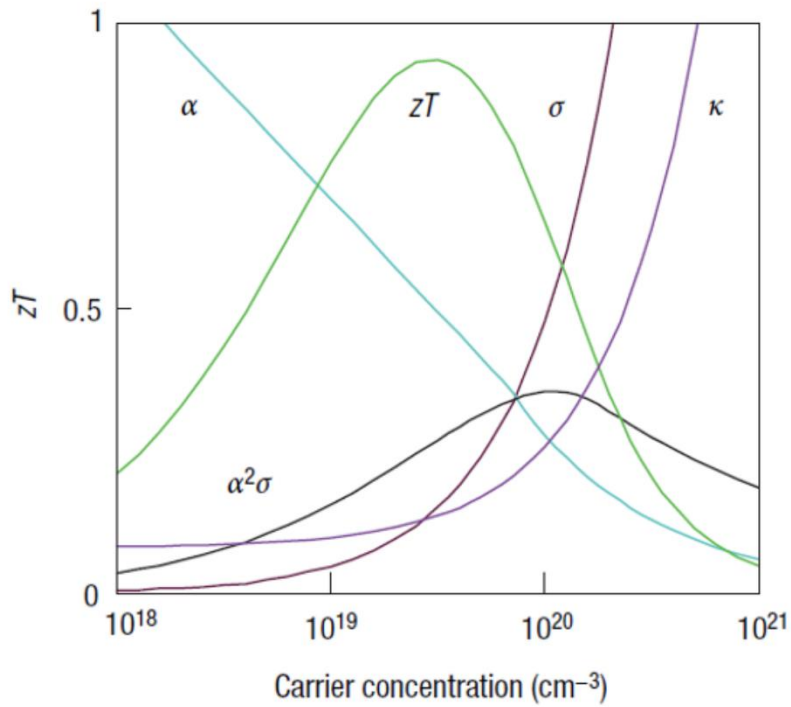


Figure 1.9 Schematic illustration of the relation between the carrier concentration and the ZT value. Optimum carrier concentration to maximize the ZT value is present between 10^{19} and 10^{21} cm^{-3} . (from Ref. [1f] Snyder, G. J.; Toberer, E. S. *Nat. Mater.* **2008**, 7, 105.)

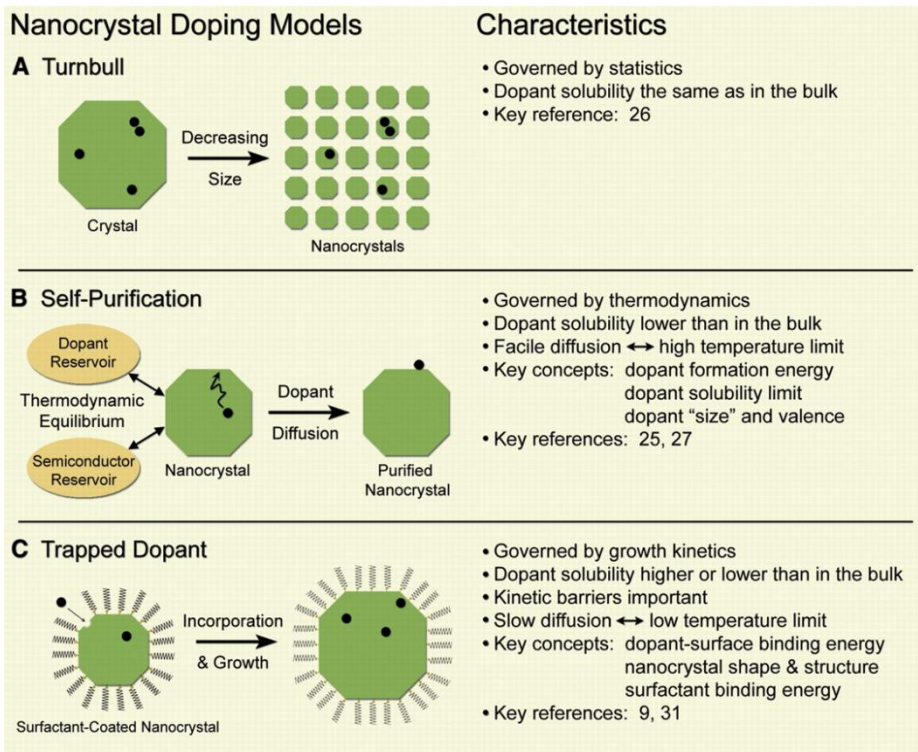


Figure 1.10 Models to explain the doping in semiconductor nanocrystals. (a) Turnbull model, where the probability of doping decreases as the size is reduced. (b) Self-purification, where thermodynamics is assumed during the nanocrystal growth. (c) Trapped dopant model, where kinetics is assumed during the nanocrystal growth. (from Ref. [4f] Norris, D. J.; Efros, A. L.; Erwin, S. C. *Science* **2008**, 319, 1776.)

1.3.1 Surface Treatment

The physicochemical properties of the nanocrystals are strongly influenced by the surface chemistry in addition to their morphology and composition because the ratio of surface area to volume increases as the size decreases.^[7a] Therefore, understanding the surface chemistry of nanocrystals is key for engineering the nanocrystal properties. Colloidal synthesis typically produces the nanocrystals capped with the long-chain organic ligands, which play an important role in controlling the nucleation and growth during the formation of nanocrystals.^[7b] However, because the bulky organic ligands are usually an electrical insulator, they hinder the charge transport in the nanocrystal-based electronic device. Thus, many studies have been reported on modifying the surface of colloidal nanocrystals. Several inorganic ligands and short ligands such as pyridine,^[7c] hydrazine,^[7d] ammonia,^[6c,7e] short-chain alkyl thiol,^[7f] chalcogenidometallates,^[7g,h] halometallates,^[7i,j] pseudohalide,^[7i] chalcogenide,^[7k] (poly)oxometalates,^[7l] halide,^[7m,n] and metal ions,^[7o] and tetrafluoroborate^[7p,q] salts have been used to replace the organic ligands. A simple phase-transfer procedure in two-phase liquid is typically used for the ligand exchange of the nanocrystals. For examples, by mixing the nanocrystals in a nonpolar solvent and the target ligands

in a polar solvent, the original bulky ligands are replaced by the targeted ligands. The surface-modified nanocrystals exhibit a shorter interparticle distance, making the nanocrystal coupling stronger (Fig. 1.11). Interestingly, the material properties of the nanocrystals are strongly dependent on the ligand species because the interaction between the surface atoms and the ligands modifies the electronic structure and the atomic arrangement. Furthermore, the ligands can provide a multiple functionality. For examples, CdCl_3^- ligands of CdCl_3^- -capped CdTe nanocrystals act not only as a sintering promoter but also as a dopant, thereby improving the quality of the CdTe film and the solar cell performance.^[7r]

In the nanostructured bulk materials assembled by the nanocrystals, the doping effect can be achieved through the surface treatment of nanoparticles. The pellet obtained from the oleic acid-capped PbS nanocrystals without surface treatment shows a p-type nature at room temperature and a n-type conductivity at high temperature.^[8a] When the PbS nanocrystals are treated with hydrochloric acid, the pellet exhibits a n-type nature in the whole temperature range and the electrical conductivity at room temperature increases 10^1 – 10^3 times. Furthermore, the electron concentration can be finely modified by adjusting the

amount of hydrochloric acid.

Brock group demonstrated that the carrier type of PbTe changes depending on the ligand species that are used for the surface treatment of PbTe nanocrystals.^[8b] The PbTe nanocrystals treated with ammonium sulfide (NH₄S) show a p-type conduction, whereas the PbTe nanocrystals treated with tetrabutylammonium iodide (TBAI) exhibit a n-type character. The pellet does not show the high *ZT* due to its low electrical conductivity, but the results share the similar idea to the previous report in that the carrier type of the PbSe nanocrystals can be changed by the ligand exchange.^[8c]

Ligand exchange using alkali metal chalcogenide is effective to modulate the p-type electrical conductivity of PbS nanocrystals.^[8d] Substitutional doping with Na and K is achieved by the ligand exchange followed by subsequent annealing procedure. Through this treatment, the hole concentration is controlled up to $3 \times 10^{19} \text{ cm}^{-2}$. Recently, it was reported that, in the PbS-Ag₂S heterostructured nanocrystals, the carrier type changes from n-type to p-type after K₂Te treatment, and the electrical conductivity is dramatically improved from 0.3 S cm^{-1} to 4 S cm^{-1} at room temperature with a high hole density of $\sim 1 \times 10^{19} \text{ cm}^{-3}$.^[8e]

Hyeon group synthesized a novel bulk material, K_{0.06}Bi₂Te_{3.18}, which

violates the phase diagram, by the surface treatment on the $\text{Bi}_2\text{Te}_{3.14}$ nanotubes.^[8f] The surface treatment with KOH not only removes polyvinylpyrrolidone (PVP) ligands on the surface of the $\text{Bi}_2\text{Te}_{3.14}$ nanotubes but improves the power factor accompanied by the increase of both the electron concentration and the mobility due to excess K and Te inserted into the $\text{K}_{0.06}\text{Bi}_2\text{Te}_{3.18}$. Furthermore, TEM analysis of the cross section of the $\text{K}_{0.06}\text{Bi}_2\text{Te}_{3.18}$ helps to understand the unusual composition and the thermoelectric properties (Fig. 1.12). The surface treatment not only enables to incorporate the impurity atoms inside the lattice, but also allows for the multiphase bulk materials.^[8g-i] The properties of the nanostructured bulk materials are also affected by the ligands left on the surface after synthesis of the nanocrystals.^[8j,k]

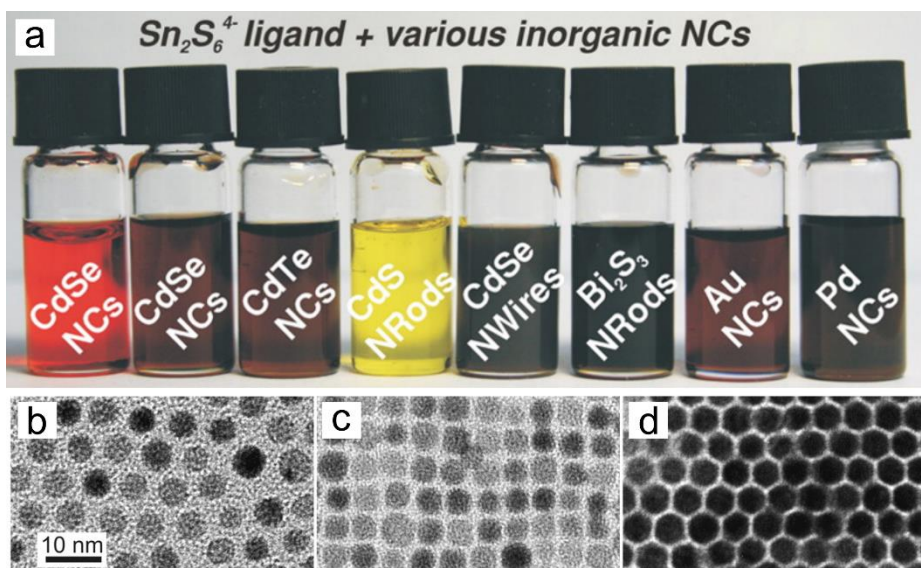


Figure 1.11 (a) Various inorganic nanocrystals dispersed in polar solvents after treatment with chalcogenidometallates ligand ($\text{Sn}_2\text{S}_6^{4-}$). TEM images of Au nanocrystals capped with (b) dodecanethiol and (c) $(\text{N}_2\text{H}_5)_4\text{Sn}_2\text{S}_6$. (d) TEM image of a three-dimensional superlattice composed of Au nanocrystals capped with $(\text{N}_2\text{H}_5)_4\text{Sn}_2\text{S}_6$. (from Ref. [7g] Kovalenko, M. V.; Scheele, M.; Talapin, D. V. *Science* **2009**, *324*, 1417.)

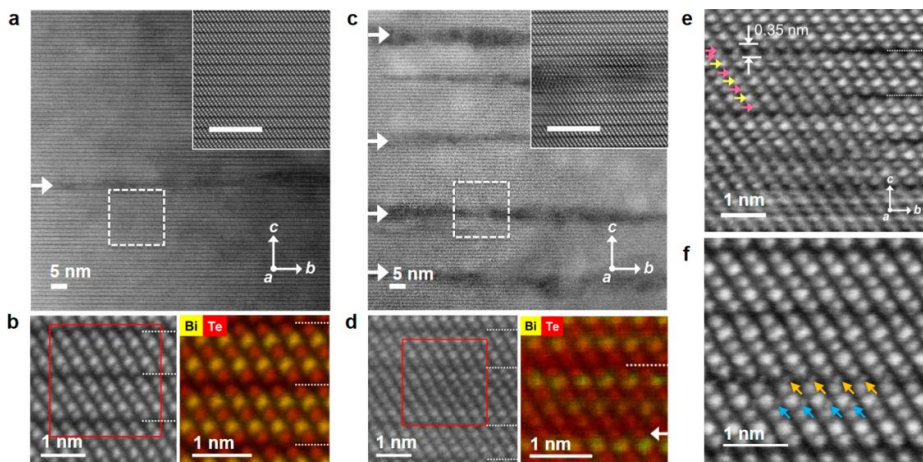


Figure 1.12 Cross-section scanning TEM images showing atomic structure of (a, b) bulk $\text{Bi}_2\text{Te}_{3.14}$ (BT) and (c–f) $\text{K}_{0.06}\text{Bi}_2\text{Te}_{3.18}$ (KBT). Elemental mapping of (b) BT and (d) KBT. (e) Septuple atomic layer of $[\text{Bi}_3\text{Te}_4]$ and intercalation of Te in the van der Waals gap. Color code: Bi, yellow and Te, pink. (f) Interlayer (orange) and interstitial (blue) sites of potassium in KBT. (from Ref. [8f] Park, K.; Ahn, K.; Cha, J.; Lee, S.; Chae, S. I.; Cho, S. P.; Ryee, S.; Im, J.; Lee, J.; Park, S. D.; Han, M. J.; Chung, I.; Hyeon, T. *J. Am. Chem. Soc.* **2016**, *138*, 14458.)

1.3.2 Nanocrystals Blending

Mixing different kinds of nanocrystals is the other method to control the transport properties in the nanostructured bulk materials. Because a variety of the nanocrystals that have already been reported is available to use, it is readily accessible to prepare the novel nanostructured bulk materials *via* blending different nanocrystals. The material type (metal and semiconductor) and the mixing ratio of nanocrystals are important factors in determining the properties of the resultant pellets.

Ramanath group reported that the ratio of n-type Bi_2Te_3 and p-type Sb_2Te_3 nanoplates determines the carrier type of the $\text{Bi}_{2-x}\text{Sb}_x\text{Te}$ pellet and the lattice thermal conductivity is reduced by ~40% due to alloying and nanostructuring.^[8k] When the ratio of Sb_2Te_3 nanoplates in the mixture of Bi_2Te_3 and Sb_2Te_3 nanoplates exceeds 20%, the major carrier changes from electrons (n-type) to holes (p-type). Thus, a high ZT of 1.1 at room temperature is measured for the p-type $\text{Bi}_{0.5}\text{Sb}_{1.5}\text{Te}_3$ obtained from a mixture of 1:3 Bi_2Te_3 : Sb_2Te_3 nanoplates.

Jeong group successfully synthesized the $\text{Bi}_2\text{Te}_3/\text{Bi}_2\text{Se}_3$ nanocomposites by blending the Bi_2Te_3 and Bi_2Se_3 nanoflakes with controlled compositions *via* simply tuning the mixing ratio. TEM analysis confirmed the heterostructures formed by the Bi_2Te_3 and Bi_2Se_3

nanostructures.^[9a] The maximum power factor was measured at an optimum mixing ratio ($\text{Bi}_2\text{Te}_3:\text{Bi}_2\text{Se}_3=85:15$). Furthermore, a high ZT of ~ 0.7 at 400 K was obtained due to the rise of Seebeck coefficient by the carrier filtering effect at the interface and the decrease of the lattice thermal conductivity by nanostructuring.

The nanostructured materials combined with metal nanocrystals and semiconductor nanocrystals have been prepared for thermoelectric characterization. Cabot group demonstrated the synthesis and characterization of the nanocomposites prepared by blending the PbS nanocrystals with the Ag nanocrystals (Fig. 1.13).^[9b] All nanocomposites mixed with Ag nanoparticles show n-type conduction. It is because electrons are injected from Ag into the conduction band of PbS and act as major carriers. Interestingly, the enhancement on both electron concentration and mobility were observed with the implantation of Ag nanocrystals. They explain that the inclusion of Ag nanograins reduces the effective height of the energy barrier formed at the interface with the rise of Fermi level. This strategy yielded a high power factor of $1.68 \text{ mW m}^{-1} \text{ K}^{-2}$ at 850 K, which cannot be achieved by impurity doping. They also explained that the selection of metal nanocrystals with appropriate work functions plays an important role in carrier injection.

The introduction of metal nanoparticles to Bi_2Te_3 nanomaterials also increases the thermoelectric efficiency. The Ag nanocrystals-dispersed Bi_2Te_3 nanocomposite was prepared by evenly mixing Ag nanocrystals in Bi_2Te_3 nanopowder *via* a solution-based ultrasonic-dispersion method.^[9c] The hierarchical structure of the heterostructured bulk effectively reduces the thermal conductivity to $0.41 \text{ W m}^{-1} \text{ K}^{-1}$ (room temperature) in Bi_2Te_3 containing 2 vol% Ag nanocrystals. In addition, due to the improved electrical conductivity and carrier filtering effect, a high power factor of $1.14 \text{ mW m}^{-1} \text{ K}^{-2}$ was measured at 475K.

In addition to mixing different nanocrystals, research has been carried out to mix nanoparticles with micro/meso-scale particles. Mixing particles with different size scales has several advantages. Firstly, the nano-sized particles act as a scattering point for phonons to lower the thermal conductivity. Secondly, micro/mesoscale particles can reduce the loss of the electrical conductivity. Third, the reduced melting point of the nanoparticles lowers the sintering temperature and at the same time a relatively high packing density is possible (>90%) by the micro/meso-scale particles.

The Stucky group synthesized the Bi_2Te_3 -Te nano-heterostructures by a galvanic replacement reaction using Ni nanoparticles as templates and

reducing agents.^[9d] The pellet prepared by mixing the Bi₂Te₃-Te nanoheterostructures with the microscale Bi₂Te₃ has a high density of ~93%. Microscale particles with nanoplate structures were present inside the pellet, resulting in the low lattice thermal conductivity of 0.5 W m⁻¹ K⁻¹.

Talopin group performed the interfacial engineering by mixing Bi_{2-x}Sb_xTe₃ ball-milled particles with Bi nanocrystals (~ 10 nm) capped with the inorganic Sb₂Te₇⁴⁻ ligands.^[9e] Sb₂Te₇⁴⁻-capped Bi nanocrystals are attached to ball-milled particles and make possible the sintering temperatures below 400 °C. The relative density of the pellet is 92–95%. Annealing the Sb₂Te₇⁴⁻-capped Bi nanocrystals at the high temperature yield a phase with a Bi_{3.2}Sb_{0.8}Te_{2.9} composition. In a similar way, Sb₂Te₇⁴⁻-capped Bi nanocrystals on the surface of stoichiometric Bi_{0.5}Sb_{1.5}Te₃ ball-milled particles (~50 nm) generate Bi-rich phases at the interface through chemical transformation during annealing. Excess Bi condition at the interface causes the formation of Bi_{Te} antisites, which act as an acceptor, resulting in the hole doping from the surface to the matrix. As the ratio of Bi nanocrystals increases, the hole concentration increases and the mobility decreases. If off-stoichiometric Bi_{0.5}Sb_{1.5}Te_{3.2} ball-milled particles (~70 nm) are used instead of Bi_{0.5}Sb_{1.5}Te₃ particles,

excess Te reacts with Bi nanocrystals. In this case, the surface composition is nearly stoichiometric and has little doping effect.

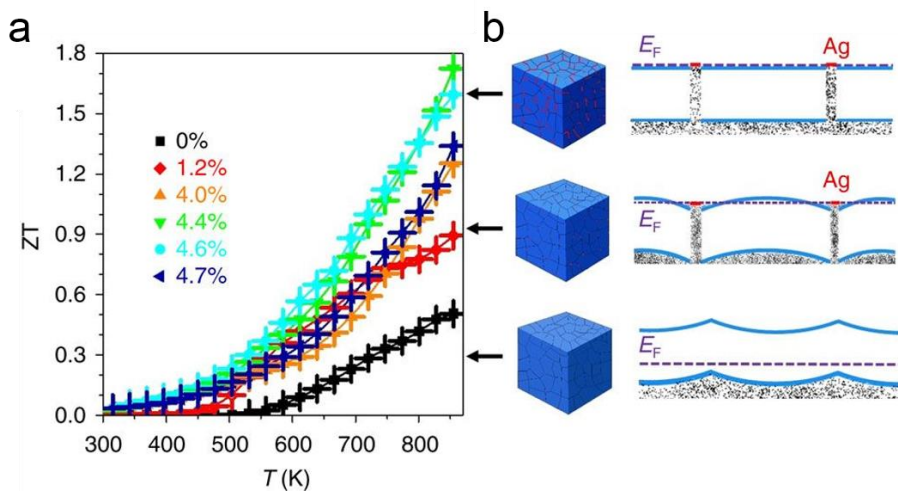


Figure 1.13 (a) ZT value as a function of temperature for PbS and Ag-PbS nanocomposites. (b) Schematic band structure with different volume fraction of Ag at the interface. (from Ref. [9b] Ibanez, M.; Luo, Z.; Genc, A.; Piveteau, L.; Ortega, S.; Cadavid, D.; Dobrozhan, O.; Liu, Y.; Nachtegaal, M.; Zebarjadi, M.; Arbiol, J.; Kovalenko, M. V.; Cabot, A. *Nat. Commun.* **2016**, *7*, 10766.)

1.3.3 Heterostructured Nanocrystals

Combinatorial blending has allowed the transport properties of nanostructured bulk to be controlled, but still limited to achieving a uniform distribution at the nano/meso-scale. A suitable strategy to overcome this limitation is to design and synthesize the heterostructured nanomaterials composed of the desired phases.

The carrier type and concentration are influenced by the ratio of the phases of which the heterostructured nanomaterials are composed. For example, PbTe nanomaterials show p-type characteristics, whereas nanoparticles with more than 33% contents of PtTe₂ show n-type conduction, and the carrier concentration increases.^[10a] Ramanath group demonstrated the possibility of tuning the Seebeck coefficient *via* Te heterostructuring. The absolute value of the Seebeck coefficient for the n-type Bi₂Te₃ nanoplates decreases after Te heterostructuring, whereas the Seebeck coefficient increases for the p-type Sb₂Te₃ nanoplates.^[10b]

In PbTe@PbS core-shell nanocrystals, the transport properties are dependent on the ratio of PbS and PbTe.^[10c] When the ratio of PbS is less than 0.4, it exhibits p-type property at room temperature and changes to the n-type conduction at an inversion temperature. The inversion temperature decreases with increasing the PbS content, probably due to

the increased ratio of the minor carrier (electron) involved in the Seebeck coefficient. Samples with PbS content greater than 0.4 have n-type properties at the whole temperatures range. In addition, the thermal conductivity is lower than that of the single component, and the thermal conductivity of $0.53 \text{ W m}^{-1} \text{ K}^{-1}$ at 710 K was measured in $(\text{PbTe})_{0.28}(\text{PbS})_{0.72}$ (vs. 1.2 for PbTe and 0.77 for PbS). It resulted in a high ZT of ~ 1.1 at 710 K through controlling the phase ratio without doping strategy.

Interfaces formed by different phases selectively scatter carriers. According to the formula of Seebeck coefficient $S = (S_1\sigma_1 + S_2\sigma_2)/(\sigma_1 + \sigma_2)$, this filtering effect affects the Seebeck coefficient.^[10d] For example, the Seebeck coefficient in $\text{Ag}_2\text{Te-PbTe}$ heterostructured bulk ($271 \mu\text{V K}^{-1}$ at 380 K) is greater than that in Ag_2Te bulk ($192 \mu\text{V K}^{-1}$ at 380 K). Theoretical calculations based on the Boltzmann transport equation (BTE) support the experimental results. The interfacial energy barriers for both the electron and hole is formed by Ag_2Te and PbTe and affects the Seebeck coefficient. The electron conduction adversely affects p-type Seebeck coefficient. Higher interfacial barrier for electrons reduces the contribution of electrons to the electrical conductivity, thereby increasing the Seebeck coefficient in the heterostructured bulk.

In Bi₂Te₃-Te heterostructured nanowires, the electrical conductivity (3.05 S cm⁻¹ and 600 μV K⁻¹) and the Seebeck coefficient at room temperature are larger than those of single-component Te nanowires (0.08 S cm⁻¹ and 408 μV K⁻¹).^[10e] It is explained by the fact that the electrical conductivity of Bi₂Te₃ is larger than that of Te, and low-energy holes are filtered out at the interface. In addition, the low thermal conductivity of 0.365 W m⁻¹ K⁻¹ at 300 K was obtained due to the various interfaces formed between nanostructures (nanowire-nanowire, nanowire-nanoplate, and nanoplates-nanoplate). By the similar reasons, Bi₂Se₃@Bi₂Te₃ nanoplates, synthesized by epitaxial growth, have n-type thermoelectric properties with a high *ZT* of ~0.71 K at 450 K.^[10f] Epitaxial heterostructure is an important structure that helps to increase power factor while minimizing loss in the electrical conductivity. This effect was observed in PbSe/Bi₂Se₃ heterostructure.^[10g]

In heterostructured materials in combination with appropriate phases, the onset temperature occurring the bipolar effect can be increased. The bipolar effect is detrimental in the thermoelectric performance because thermally activated electrons and holes contribute to the electrical conduction, thereby decreasing the Seebeck coefficient and increasing the thermal conductivity. Therefore, reducing the bipolar effect is an

important issue in the thermoelectric materials. In PbTe-Bi_{0.7}Sb_{1.3}Te₃ nano-heterostructures, the delayed bipolar effects were found.^[10h] By controlling the ratio of Pb, Sb, Bi, and Te precursors, the ratio of PbTe and BiSbTe was controlled. As the content of PbTe increases, the hole concentration increases due to the Pb doping effect. The increase in the optical band gap due to the Burstein-Moss shift is in line with the Hall measurement, confirming the hole doping. Due to the enlarged band gap by the doping effect, the temperature at which the bipolar effect occurs increases. Accordingly, the temperature showing the maximum Seebeck coefficient and the onset temperature at which the thermal conductivity rises shift to the higher temperature. In addition, the lattice thermal conductivity is reduced by small grain sizes and large amounts of defects. Because of these factors, a high ZT over 1 is obtained at 500–600 K, which is 100 K higher than the operating temperature of the existing Bi_{2-x}Sb_xTe₃ material.

1.4 Dissertation Overview

Over the last three decades, nanoscience and nanotechnology have been rapidly developed. With the advance in nanochemistry, colloidal chemistry has provided an effective synthetic route to produce the nanomaterials with the precisely tuned structures and compositions. In the current dissertation, the synthesis and applications of two-dimensional nanostructures have been studied. The thesis is composed of two chapters.

In the first part (Chapter 2), I demonstrate that the MoS₂ nanosheets with uniform size and thickness are synthesized in a large scale *via* a colloidal chemical method. The synthesized MoS₂ nanosheets exhibit much narrower size and thickness distribution than those of exfoliated MoS₂. Additionally, the colloidal stability and the reproducibility allow the solution-processed fabrication and integration for a flexible RRAM array. The RRAM using the synthesized MoS₂ nanosheets presents a much higher on/off ratio than that based on exfoliated MoS₂. Furthermore, the synthesized MoS₂ nanosheets are assembled for the wafer-scale integration of the RRAM array.

In the second part (Chapter 3), I describe that SnSe nanoplates with dislocations are synthesized *via* a simple heat-up method. A facile

solution synthesis results in the formation of dislocations in SnSe nanoplates. TEM analysis demonstrates that the many dislocations are left after the consolidation of the SnSe nanoplates by spark plasma sintering. Surface treatment with ammonia solution removes the impurities on the surface such as oleylamine, iodide ligands, and unwanted oxides from nanoplate surface, thereby enhancing the electrical conductivity of the sintered pellet accompanied with an increased hole concentration. With the ultralow lattice thermal conductivity ($\sim 0.23 \text{ W m}^{-1} \text{ K}^{-1}$) of the unique nanostructured materials, a high thermoelectric figure of merit ZT of ~ 1.1 at 873 K is achieved.

1.5 References

- [1] (a) Vineis, C. J.; Shakouri, A.; Majumdar, A.; Kanatzidis, M. G. *Adv. Mater.* **2010**, *22*, 3970. (b) Yang, L.; Chen, Z.-G.; Dargusch, M. S.; Zou, J. *Adv. Energy Mater.* **2018**, *8*, 1701797. (c) Zeier, W. G.; Zevalkink, A.; Gibbs, Z. M.; Hautier, G.; Kanatzidis, M. G.; Snyder, G. J. *Angew. Chem. Int. Ed.* **2016**, *55*, 6826. (d) Minnich, A. J.; Dresselhaus, M. S.; Ren, Z. F.; Chen, G. *Energy Environ. Sci.* **2009**, *2*, 466. (e) Zebarjadi, M.; Esfarjani, K.; Dresselhaus, M. S.; Ren, Z. F.; Chen, G. *Energy Environ. Sci.* **2012**, *5*, 5147. (f) Snyder, G. J.; Toberer, E. S. *Nat. Mater.* **2008**, *7*, 105. (g) Bell, L. E. *Science* **2008**, *321*, 1457. (h) He, J.; Tritt, T. M. *Science* **2017**, *357*, eaak9997. (i) Lawrence Livermore National Laboratory Energy Flow Charts: Charting the Complex Relationships among Energy, Water, and Carbon. <https://flowcharts.llnl.gov/home> (accessed 20 May, 2019). (j) Chowdhury, I.; Prasher, R.; Lofgreen, K.; Chrysler, G.; Narasimhan, S.; Mahajan, R.; Koester, D.; Alley, R.; Venkatasubramanian, R. *Nat. Nanotechnol.* **2009**, *4*, 235. (k) Majumdar, A. *Nat. Nanotechnol.* **2009**, *4*, 214.
- [2] (a) Hicks, L. D.; Dresselhaus, M. S. *Phys. Rev. B* **1993**, *47*, 12727. (b) Hicks, L. D.; Dresselhaus, M. S. *Phys. Rev. B* **1993**, *47*, 16631. (c) Venkatasubramanian, R.; Siivola, E.; Colpitts, T.; O'Quinn, B. *Nature*

2001, *413*, 597. (d) Harman, T. C.; Taylor, P. J.; Walsh, M. P.; LaForge, B. E. *Science* **2002**, *297*, 2229. (e) Mahan, G. D.; Sofo, J. O. *Proc. Natl. Acad. Sci. U. S. A.* **1996**, *93*, 7436. (f) Nakpathomkun, N.; Xu, H. Q.; Linke, H. *Phys. Rev. B* **2010**, *82*, 235428. (g) Humphrey, T. E.; Linke, H. *Phys. Rev. Lett.* **2005**, *94*, 096601. (h) Josefsson, M.; Svilans, A.; Burke, A. M.; Hoffmann, E. A.; Fahlvik, S.; Thelander, C.; Leijnse, M.; Linke, H. *Nat. Nanotechnol.* **2018**, *13*, 920. (i) Wang, R. Y.; Feser, J. P.; Lee, J. S.; Talapin, D. V.; Segalman, R.; Majumdar, A. *Nano. Lett.* **2008**, *8*, 2283.

[3] Poudel, B.; Hao, Q.; Ma, Y.; Lan, Y.; Minnich, A.; Yu, B.; Yan, X.; Wang, D.; Muto, A.; Vashaee, D.; Chen, X.; Liu, J.; Dresselhaus, M. S.; Chen, G.; Ren, Z. *Science* **2008**, *320*, 634.

[4] (a) Kovalenko, M. V.; Manna, L.; Cabot, A.; Hens, Z.; Talapin, D. V.; Kagan, C. R.; Klimov, V. I.; Rogach, A. L.; Reiss, P.; Milliron, D. J.; Guyot-Sionnest, P.; Konstantatos, G.; Parak, W. J.; Hyeon, T.; Korgel, B. A.; Murray, C. B.; Heiss, W. *ACS Nano* **2015**, *9*, 1012. (b) Talapin, D. V.; Lee, J. S.; Kovalenko, M. V.; Shevchenko, E. V. *Chem. Rev.* **2010**, *110*, 389. (c) Lee, J.; Yang, J.; Kwon, S. G.; Hyeon, T. *Nat. Rev. Mater.* **2016**, *1*, 16034. (d) Ortega, S.; Ibanez, M.; Liu, Y.; Zhang, Y.; Kovalenko, M. V.; Cadavid, D.; Cabot, A. *Chem. Soc. Rev.* **2017**, *46*,

3510. (e) Alivisatos, A. P. *Science* **1996**, *271*, 933. (f) Norris, D. J.; Efros, A. L.; Erwin, S. C. *Science* **2008**, *319*, 1776. (g) Buonsanti, R.; Milliron, D. J. *Chem. Mater.* **2013**, *25*, 1305.
- [5] (a) Zide, J. M. O.; Vashaee, D.; Bian, Z. X.; Zeng, G.; Bowers, J. E.; Shakouri, A.; Gossard, A. C. *Phys. Rev. B* **2006**, *74*, 205335. (b) Ko, D. K.; Kang, Y.; Murray, C. B. *Nano Lett.* **2011**, *11*, 2841. (c) Zhang, Y.; Snedaker, M. L.; Birkel, C. S.; Mubeen, S.; Ji, X.; Shi, Y.; Liu, D.; Liu, X.; Moskovits, M.; Stucky, G. D. *Nano Lett.* **2012**, *12*, 1075. (d) Zhang, Y.; Bahk, J. H.; Lee, J.; Birkel, C. S.; Snedaker, M. L.; Liu, D.; Zeng, H.; Moskovits, M.; Shakouri, A.; Stucky, G. D. *Adv. Mater.* **2014**, *26*, 2755.
- [6] (a) Kasap, S. O., *Principles of electronic materials and devices*. 2018. (b) Hsu, K. F.; Loo, S.; Guo, F.; Chen, W.; Dyck, J. S.; Uher, C.; Hogan, T.; Polychroniadis, E. K.; Kanatzidis, M. G. *Science* **2004**, *303*, 818. (c) Scheele, M.; Oeschler, N.; Veremchuk, I.; Reinsberg, K. G.; Kreuziger, A. M.; Kornowski, A.; Broekaert, J.; Klinke, C.; Weller, H. *ACS Nano* **2010**, *4*, 4283. (d) Son, J. S.; Choi, M. K.; Han, M. K.; Park, K.; Kim, J. Y.; Lim, S. J.; Oh, M.; Kuk, Y.; Park, C.; Kim, S. J.; Hyeon, T. *Nano Lett.* **2012**, *12*, 640. (e) Zhang, G.; Kirk, B.; Jauregui, L. A.; Yang, H.; Xu, X.; Chen, Y. P.; Wu, Y. *Nano Lett.* **2012**, *12*, 56.

[7] (a) Boles, M. A.; Ling, D.; Hyeon, T.; Talapin, D. V. *Nat. Mater.* **2016**, *15*, 141. (b) Kwon, S. G.; Hyeon, T. *Small* **2011**, *7*, 2685. (c) Katari, J. E. B.; Colvin, V. L.; Alivisatos, A. P. *J. Phys. Chem.* **1994**, *98*, 4109. (d) Talapin, D. V.; Murray, C. B. *Science*, **2005**, *310*, 86. (e) Scheele, M.; Oeschler, N.; Veremchuk, I.; Peters, S. O.; Littig, A.; Kornowski, A.; Klinke, C.; Weller, H. *ACS Nano* **2011**, *5*, 8541. (f) Webber, D. H.; Brutchey, R. L. *J. Am. Chem. Soc.* **2012**, *134*, 1085. (g) Kovalenko, M. V.; Scheele, M.; Talapin, D. V. *Science* **2009**, *324*, 1417. (h) Dolzhenkov, D. S.; Zhang, H.; Jang, J.; Son, J. S.; Panthani, M. G.; Shibata, T.; Chattopadhyay, S.; Talapin, D. V. *Science* **2015**, *347*, 425. (i) Zhang, H.; Jang, J.; Liu, W.; Talapin, D. V. *ACS Nano* **2014**, *8*, 7359. (j) Dirin, D. N.; Dreyfuss, S.; Bodnarchuk, M. I.; Nedelcu, G.; Papagiorgis, P.; Itskos, G.; Kovalenko, M. V. *J. Am. Chem. Soc.* **2014**, *136*, 6550. (k) Nag, A.; Kovalenko, M. V.; Lee, J. S.; Liu, W.; Spokoyny, B.; Talapin, D. V. *J. Am. Chem. Soc.* **2011**, *133*, 10612. (l) Huang, J.; Liu, W.; Dolzhenkov, D. S.; Protesescu, L.; Kovalenko, M. V.; Koo, B.; Chattopadhyay, S.; Shenchenko, E. V.; Talapin, D. V. *ACS Nano* **2014**, *8*, 9388. (m) Tang, J.; Kemp, K. W.; Hoogland, S.; Jeong, K. S.; Liu, H.; Levina, L.; Furukawa, M.; Wang, X.; Debnath, R.; Cha, D.; Chou, K. W.; Fischer, A.; Amassian, A.; Asbury, J. B.; Sargent, E. H. *Nat. Mater.*

2011, *10*, 765. (n) Ning, Z.; Voznyy, O.; Pan, J.; Hoogland, S.; Adinolfi, V.; Xu, J.; Li, M.; Kirmani, A. R.; Sun, J. P.; Minor, J.; Kemp, K. W.; Dong, H.; Rollny, L.; Labelle, A.; Carey, G.; Sutherland, B.; Hill, I.; Amassian, A.; Liu, H.; Tang, J.; Bakr, O. M.; Sargent, E. H. *Nat. Mater.* **2014**, *13*, 822. (o) Nag, A.; Chung, D. S.; Dolzhenkov, D. S.; Dimitrijevic, N. M.; Chattopadhyay, S.; Shibata, T.; Talapin, D. V. *J. Am. Chem. Soc.* **2012**, *134*, 13604. (p) Dong, A.; Ye, X.; Chen, J.; Kang, Y.; Gordon, T.; Kikkawa, J. M.; Murray, C. B. *J. Am. Chem. Soc.* **2011**, *133*, 998. (q) Rosen, E. L.; Buonsanti, R.; Llodes, A.; Sawvel, A. M.; Milliron, D. J.; Helms, B. A. *Angew. Chem. Int. Ed.* **2012**, *51*, 684. (r) Zhang, H.; Kurley, J. M.; Russell, J. C.; Jang, J.; Talapin, D. V. *J. Am. Chem. Soc.* **2016**, *138*, 7464.

[8] (a) Ibanez, M.; Korkosz, R. J.; Luo, Z.; Riba, P.; Cadavid, D.; Ortega, S.; Cabot, A.; Kanatzidis, M. G. *J. Am. Chem. Soc.* **2015**, *137*, 4046. (b) James, D.; Lu, X.; Nguyen, A. C.; Morelli, D.; Brock, S. L. *J. Phys. Chem. C* **2015**, *119*, 4635. (c) Oh, S. J.; Berry, N. E.; Choi, J. H.; Gaulding, E. A.; Lin, H.; Paik, T.; Diroll, B. T.; Muramoto, S.; Murray, C. B.; Kagan, C. R. *Nano Lett.* **2014**, *14*, 1559. (d) Ibanez, M.; Hasler, R.; Liu, Y.; Dobrozhan, O.; Nazarenko, O.; Cadavid, D.; Cabot, A.; Kovalenko, M. V. *Chem. Mater.* **2017**, *29*, 7093. (e) Ibanez, M.; Genc,

A.; Hasler, R.; Liu, Y.; Dobrozhan, O.; Nazarenko, O.; Mata, M.; Arbiol, J.; Cabot, A.; Kovalenko, M. V. *ACS Nano* **2019**, *13*, 6572. (f) Park, K.; Ahn, K.; Cha, J.; Lee, S.; Chae, S. I.; Cho, S. P.; Ryee, S.; Im, J.; Lee, J.; Park, S. D.; Han, M. J.; Chung, I.; Hyeon, T. *J. Am. Chem. Soc.* **2016**, *138*, 14458. (g) Ibanez, M.; Hasler, R.; Genc, A.; Liu, Y.; Kuster, B.; Schuster, M.; Dobrozhan, O.; Cadavid, D.; Arbiol, J.; Cabot, A.; Kovalenko, M. V. *J. Am. Chem. Soc.* **2019**, *141*, 8025. (h) Kovalenko, M. V.; Spokoyny, B.; Lee, J. S.; Scheele, M.; Weber, A.; Perera, S.; Landry, D.; Talapin, D. V. *J. Am. Chem. Soc.* **2010**, *132*, 6686. (i) Han, M.-K.; Kim, S.; Kim, H.-Y.; Kim, S.-J. *RSC Adv.* **2013**, *3*, 4673. (j) Chandra, S.; Banik, A.; Biswas, K. *ACS Energy Lett.* **2018**, *3*, 1153. (k) Mehta, R. J.; Zhang, Y.; Karthik, C.; Singh, B.; Siegel, R. W.; Borca-Tasciuc, T.; Ramanath, G. *Nat. Mater.* **2012**, *11*, 233.

[9] (a) Min, Y.; Roh, J. W.; Yang, H.; Park, M.; Kim, S. I.; Hwang, S.; Lee, S. M.; Lee, K. H.; Jeong, U. *Adv. Mater.* **2013**, *25*, 1425. (b) Ibanez, M.; Luo, Z.; Genc, A.; Piveteau, L.; Ortega, S.; Cadavid, D.; Dobrozhan, O.; Liu, Y.; Nachtegaal, M.; Zebarjadi, M.; Arbiol, J.; Kovalenko, M. V.; Cabot, A. *Nat. Commun.* **2016**, *7*, 10766. (c) Zhang, Q.; Ai, X.; Wang, L.; Chang, Y.; Luo, W.; Jiang, W.; Chen, L. *Adv. Funct. Mater.* **2015**, *25*, 966. (d) Zhang, Y.; Wang, H.; Kraemer, S.; Shi, Y.; Zhang, F.;

Snedaker, M.; Ding, K.; Moskovits, M.; Snyder, G. J.; Stucky, G. D. *ACS Nano* **2011**, *5*, 3158. (e) Son, J. S.; Zhang, H.; Jang, J.; Poudel, B.; Waring, A.; Nally, L.; Talapin, D. V. *Angew. Chem. Int. Ed.* **2014**, *53*, 7466.

[10] (a) Zhou, W.; Zhu, J.; Li, D.; Hng, H. H.; Boey, F. Y. C.; Ma, J.; Zhang, H.; Yan, Q. *Adv. Mater.* **2009**, *21*, 3196. (b) Mehta, R. J.; Karthik, C.; Singh, B.; Teki, R.; Borca-Tasciuc, T.; Ramanath, G. *ACS Nano* **2010**, *4*, 5055. (c) Ibanez, M.; Zamani, R.; Gorse, S.; Fan, J.; Ortega, S.; Cadavid, D.; Morante, J. R.; Arbiol, J.; Cabot, A. *ACS Nano* **2013**, *7*, 2573. (d) Yang, H.; Bahk, J. H.; Day, T.; Mohammed, A. M.; Snyder, G. J.; Shakouri, A.; Wu, Y. *Nano Lett.* **2015**, *15*, 1349. (e) Zhang, G.; Fang, H.; Yang, H.; Jauregui, L. A.; Chen, Y. P.; Wu, Y. *Nano Lett.* **2012**, *12*, 3627. (f) Min, Y.; Park, G.; Kim, B.; Giri, A.; Zeng, J.; Roh, J. W.; Kim, S. I.; Lee, K. H.; Jeong, U. *ACS Nano* **2015**, *9*, 6843. (g) Lin, Z.; Yin, A.; Mao, J.; Xia, Y.; Kempf, N.; He, Q.; Wang, Y.; Chen, C. Y.; Zhang, Y.; Ozolins, V.; Ren, Z.; Huang, Y.; Duan, X. *Sci. Adv.* **2016**, *2*, e1600993. (h) Xu, B.; Agne, M. T.; Feng, T.; Chasapis, T. C.; Ruan, X.; Zhou, Y.; Zheng, H.; Bahk, J. H.; Kanatzidis, M. G.; Snyder, G. J.; Wu, Y. *Adv. Mater.* **2017**, *29*, 1605140.

Chapter 2. Synthesis of Uniform-Sized Molybdenum Disulfide Nanosheets and Applications for Wafer-scale Nonvolatile Memory

2.1 Introduction

Molybdenum disulfide (MoS_2) has garnered tremendous attention as the key material for post-silicon electronics^[1-3] and optoelectronics,^[4,5] including flexible devices,^[6-10] owing to its unique band structure,^[11,12] high electron mobility,^[13,14] atomic-scale thickness,^[15,16] and superb photoluminescence properties.^[17,18] It has been reported that devices based on exfoliated MoS_2 exhibit excellent performance,^[19-21] although most of these results have been from individual devices rather than from large-scale device arrays. Recent progress in the large-area synthesis of MoS_2 *via* chemical vapor deposition (CVD) suggests the possibility of fabricating wafer-scale device arrays.^[13] However, the performance of devices based on CVD MoS_2 is still lower than that of devices using exfoliated MoS_2 . The high cost of vapor-phase synthesis in an ultrahigh-vacuum chamber is another critical issue. The assembly of exfoliated MoS_2 nanosheets may solve these issues. Nevertheless, the non-

uniformity observed in large-area device arrays, which is caused by the intrinsic polydispersity of the exfoliated MoS₂, remains a critical problem.^[22,23] Therefore, a breakthrough in the uniform synthesis and integration of high quality of MoS₂ through colloidal chemistry is highly desired.^[24,25]

Recently, MoS₂-based nonvolatile memory device has been considered as a next-generation memory module owing to its excellent electrical and mechanical performance even beyond state-of-the-art silicon electronic devices.^[19] In addition, tremendous efforts to integrate novel switching materials such as protein^[26] and graphene oxide^[27] for memory devices have been made to overcome the limitation of the conventional devices.

Here, we will demonstrate a large-scale colloidal synthesis of uniform-sized MoS₂ nanosheets and their wafer-scale integration to fabricate a flexible resistive random access memory (RRAM) array. The synthesized MoS₂ nanosheets exhibit excellent uniformity in their size and thickness distributions, in comparison with exfoliated MoS₂. Spray-coating of the well-dispersed nanosheets forms a uniform film over a 4-inch wafer. The memory device made from the synthesized MoS₂

nanosheets outperforms a control device based on exfoliated MoS₂, such as the extremely high on/off ratio of the RRAM. In addition, the ultrathin nature of the assembled MoS₂ nanosheets allows the fabrication of deformable devices. These results can provide new opportunities for the mass-production of uniform and high-quality nanomaterials as well as enable the development of deformable electronic devices for future wearable and/or mobile devices.

2.2 Experimental Section

2.2.1 Chemicals

Oleic acid (90%, Sigma-Aldrich, USA), oleylamine (80–90%, Acros Organics, USA), MoCl_5 (99.6%, Strem Chemicals, USA), tetradecylphosphonic acid (98%, Alfa-Aesar, USA), CS_2 (>99%, Sigma-Aldrich), trioctylphosphine (97%, Sigma-Aldrich), 1-butanol (Samchun), ethanol (Samchun).

2.2.2 Synthesis of Colloidal MoS_2 Nanosheets

All the procedures for synthesizing the MoS_2 nanosheets were performed under inert conditions using an argon-filled glove box and a Schlenk line technique. Oleic acid and oleylamine were degassed before the use. The precursor solution was prepared as follows. MoCl_5 (0.675 mmol) and tetradecylphosphonic acid (0.06 mmol) in 7.5 mL of oleic acid and 50 mL of oleylamine were degassed overnight. After this solution mixture was cooled, 1 mL of CS_2 was injected into it. Next, 50 mL of oleylamine in a 250 mL three-neck round-bottom flask was heated to 320 °C, and the precursor solution was slowly injected into it using a syringe pump for 30 min. After aging for 1.5 h at the same temperature, the solution was cooled, and a small amount of trioctylphosphine was added to remove the extra sulfur. The MoS_2 nanosheets were separated

by adding 1-butanol to the solution followed by subsequent centrifugation. The nanosheets were then washed with ethanol three times and dispersed in various organic solvents such as toluene, pyridine, chloroform, and tetrahydrofuran. Exfoliated MoS₂ as a control was prepared by following a method in the previously reported paper.^[22]

2.2.3 Characterization

The TEM images were obtained on a JEOL 2100F electron microscope operated at 200 kV. High-resolution TEM and scanning TEM for statistical analysis were performed using the same microscope. High-resolution TEM and high-angle annular dark-field STEM images for structural analysis were acquired using a JEM-ARM200F system with a spherical aberration corrector (operated at 80 kV) installed at the National Center for Inter-university Research Facilities (NCIRF) at Seoul National University. The XRD patterns were obtained using a D/Max-3C diffractometer equipped with a rotating anode and a Cu K α radiation source ($\lambda = 0.15418$ nm). XPS was performed using a Sigma Probe (ThermoVG, U.K.) equipped with an Al K α (1486.8 eV) X-ray source. All spectra were corrected using the binding energy of adventitious carbon 1s at 284.8 eV. The Raman spectrum was recorded

using a LabRam Aramis (Horiba Jobin Yvon) system equipped with an Ar-ion laser ($\lambda = 514.5$ nm). The optical absorption spectra were obtained using a Cary 5000E UV-VIS-NIR spectrophotometer.

2.2.4 Spray-Coating of MoS₂ Nanosheets

The substrate was placed on a hot plate that was preheated to 200 °C. MoS₂ dispersed in pyridine was spray-coated from a distance of 20 cm using an airbrush at a pressure of 40 psi (HP-BCP, ANEST IWATA-MEDEA, Japan). The substrate was placed again on the hot plate for 5 min to remove the remaining solvent completely.

2.2.5 Fabrication of Flexible MoS₂ RRAM

First, a polyimide (PI) precursor solution (polyamic acid, Sigma Aldrich, USA) was spin-coated at 4000 rpm for 60 s on a SiO₂/Si substrate (4science, Korea), and the formed film was annealed. This was followed by the thermal evaporation of a 100-nm-thick Al film. The Al film was patterned by photolithography and wet etching to construct the bottom Al electrode. Then, MoS₂ nanosheets were spray-coated on the substrate and patterned using reactive-ion etching (RIE) (CF₄ plasma, flow rate of 50 sccm, chamber pressure of 55 mTorr, and RF power of 100 W for 2 min). Then, an epoxy film (SU-8 2000.5, MicroChem, USA)

was spin-coated, and via-holes were patterned. The substrate was subsequently annealed on a hot plate at 200 °C for 3 h to fabricate the MoS₂-MoO_x heterostructure. The top Al electrode (100 nm in thickness) was deposited and patterned using the same method as that employed for the bottom electrode. Finally, a PI layer was spin-coated again and cured at 250 °C for 1 h, followed by patterning using RIE (O₂ plasma). The device, which was now sandwiched between two PI layers, was picked up using a piece of thermal-release tape (TW-50R150, Tape world, Republic of Korea) and transferred to a flexible substrate (PET) on a hotplate at 100 °C. Finally, the electrical measurements were performed using a parameter analyzer (B1500A, Agilent, USA).

2.2.6 Depth Profile Analysis of MoS₂-MoO_x Heterostructure

The samples for XPS depth profile analysis were prepared as follows. Solutions of the synthesized and exfoliated MoS₂ nanosheets with equal concentration were prepared. The concentration of MoS₂ was estimated by elemental analysis using inductively coupled plasma-atomic emission spectroscopy (Shimadzu). The same amount of each solution was sprayed onto the silicon wafer and subsequently annealed under the same

condition as mentioned above. The XPS depth profile analysis was performed using a K-alpha (Thermo U.K.) system with an Al K α (1486.8 eV) X-ray source. The synthesized and exfoliated MoS₂-MoO_x heterostructures were etched by Ar-ion sputtering at 500 eV. The photoelectrons were collected from an area with a diameter of 400 μ m.

2.2.7 Measurement of Nanoscale Resistive Switching

The nanoscale filamentary switching was analyzed in the synthesized MoS₂-MoO_x heterostructure over an area of 600 \times 600 nm² using a local-current measurement setup consisting of an AFM system (XE-7, Park system, Republic of Korea), preamplifier (SR570, Stanford Research Systems, USA), and high-voltage source meter (2410, Keithley, USA). During the SET operation, a voltage of -10 V was applied to the surface of the MoS₂-MoO_x heterostructure with a compliance current of -0.1 mA, while the bottom Al electrode was connected to the ground. The scanning rate and force for CAFM in the contact mode were 0.5 Hz and 831 nN, respectively. After the SET operation had been performed over the entire surface, the current was measured by applying a read voltage (V_{read}) of -0.1 V to the MoS₂-MoO_x heterostructure. The conducting filaments could be eliminated by applying a voltage of -2 V by scanning the

conducting AFM tip over the selected area (Fig. 2.13a). It is also confirmed that the synthesized $\text{MoS}_2\text{-MoO}_x$ heterostructure exhibits typical URS behavior (Fig. 2.13c).

2.3 Results and Discussion

The colloidal MoS₂ nanosheets were synthesized by slowly injecting a precursor solution into hot oleylamine using a syringe pump. A detailed description of the synthesis and its related schematic illustration are supplied in Fig. 2.1. Colloidal chemistry enables the synthesis of MoS₂ nanosheets at a lower temperature than that used in the CVD process, and precise control of the synthesis conditions allows large-scale production of up to ~2.2 g (inset in Fig. 2.2.a). Low-magnification transmission electron microscope (TEM) image (Fig. 2.2a) reveals that the nanosheets are mostly two-dimensional, round, and either partly aggregated or folded. High-resolution TEM (HRTEM) and corresponding fast Fourier transform (FFT) pattern reveal various crystal facets on edge sides and lateral planes of the MoS₂ nanosheets. Specifically, lattice fringes with a spacing of 0.27 nm and 0.16 nm at the lateral planes that correspond to (10 $\bar{1}$ 0) and (11 $\bar{2}$ 0) facets of hexagonal 2H-MoS₂, respectively, are observed (Fig. 2.2b and its inset). The nanosheets are vertically stacked with an interlayer spacing of 0.7 nm, as observed by scanning TEM (STEM) (Fig. 2.2e). The anisotropic nature of the synthesized MoS₂ nanosheets can be further characterized by the relative intensity and sharpness of peaks in the X-ray diffraction (XRD)

pattern (Fig. 2.3a). The reflections of $(10\bar{1}0)$ and $(11\bar{2}0)$ peaks from the lateral plane are strong and sharp, while the (0002) peak for the vertical axis (inset in Fig. 2.3a) is weak and broad.^[28] Furthermore, the number of the synthesized MoS_2 layers is estimated by using Raman spectroscopy.^[29] Typical vibrations of hexagonal MoS_2 , E_{2g}^1 and A_{1g} , are observed clearly in the Raman spectrum (Fig. 2.3b), with the peak difference of $\sim 22 \text{ cm}^{-1}$, which indicates that the synthesized MoS_2 nanosheets have approximately two layers. Finally, the X-ray photoemission spectroscopy (XPS) analysis in Fig. 2.3c and d shows that the chemical states and coordination geometry of the synthesized MoS_2 nanosheets are the same as those of the exfoliated MoS_2 , demonstrating that oxidation does not occur during the synthesis and purification process.

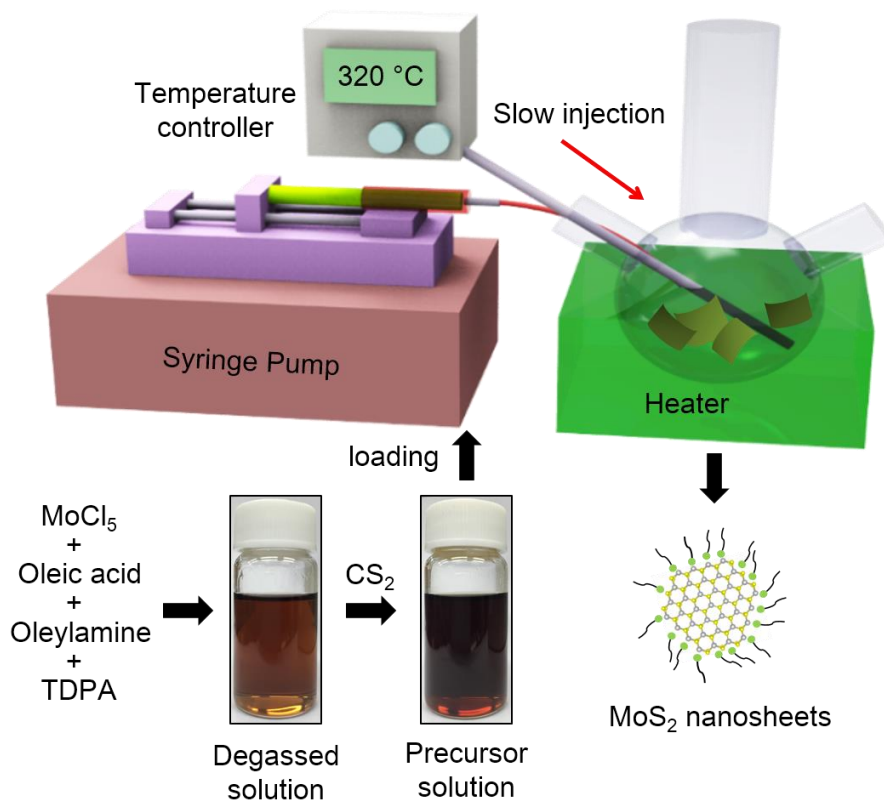


Figure 2.1 Schematic illustration for the synthesis of colloidal MoS₂ nanosheets. The sequential synthesis procedures of colloidal MoS₂ nanosheets are shown, which are synthesized by slowly injecting a precursor solution into the hot oleylamine by using a syringe pump. Photos of degassed solution and precursor solution are shown.

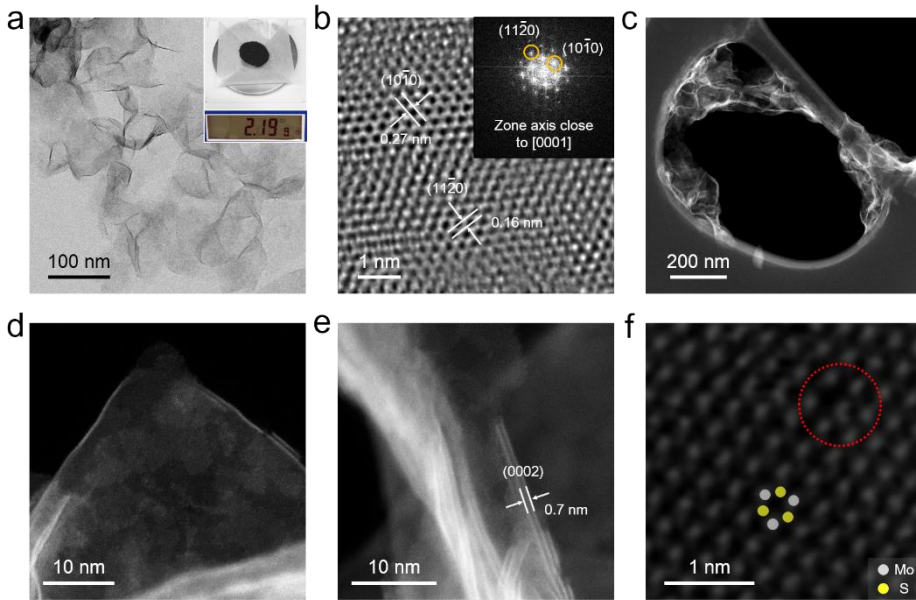


Figure 2.2 (a) Low-magnification TEM image of the synthesized MoS₂ nanosheets. The inset shows the amount of MoS₂ produced by the large-scale synthesis. (b) HRTEM image showing the (0001) plane of the MoS₂ nanosheets. The corresponding FFT pattern is shown in the inset. (c–e) STEM images of MoS₂ nanosheets on the lacey carbon TEM grid from low to high magnification. Polycrystalline and stacking nature of nanosheets are observed. (f) A HAADF-STEM image of the MoS₂ nanosheets indicates the atomic structure of MoS₂ (The image is filtered using FFT mask for clarity). Since MoS₂ nanosheets are partly bent, hexagonal structure is slightly distorted. Defect sites such as vacancies and antisites are found such as in a red dashed circle.^[30]

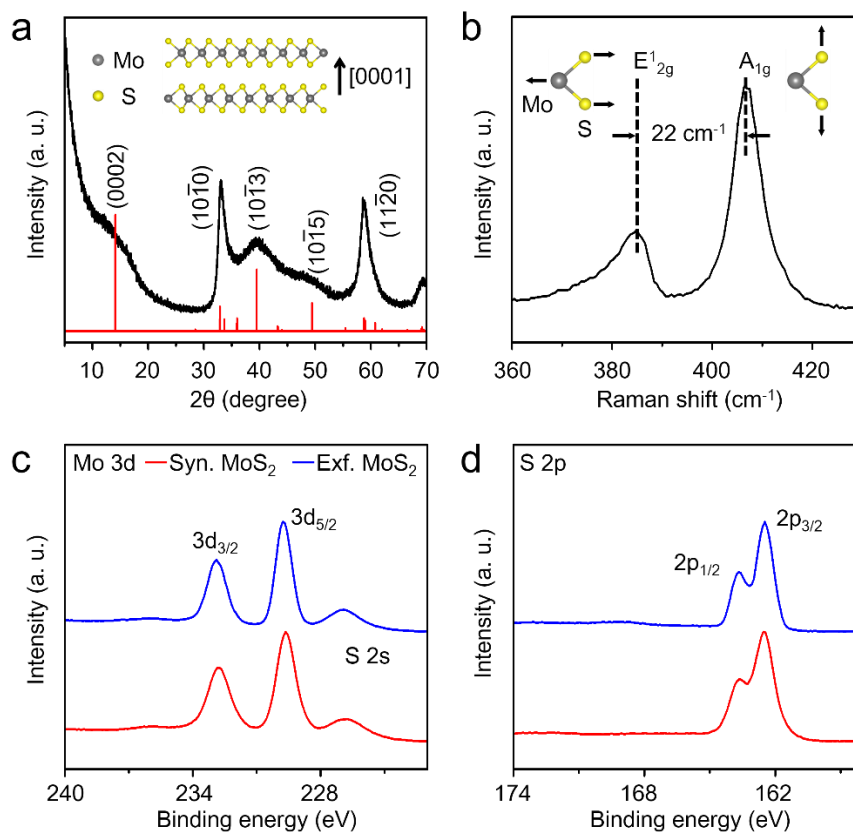


Figure 2.3 (a) XRD pattern of the synthesized MoS₂ nanosheets; the vertical lines (red) represent the reference pattern of hexagonal 2H-MoS₂ (JCPDS 75-1539). The inset shows a schematic illustration of the structure. (b) Raman spectrum showing the vibration modes E¹_{2g} and A_{1g}. The inset shows each vibration mode using the ball-and-stick model. (c) The Mo 3d and S 2s and (d) S 2p XPS peaks of the synthesized (red) and exfoliated (blue) MoS₂ nanosheets.

In an effort to understand the formation mechanism of the MoS₂ nanosheets, aliquots taken at different aging periods were investigated by using the UV-visible (UV-vis) absorption spectra, Raman spectra, and TEM images. The A and B excitonic peaks^[11] observed between 600 and 700 nm in the absorption spectra are red-shifted and become narrower after aging for 2 h (Fig. 2.4b). In addition, TEM images and Raman spectra indicate that the mixture of amorphous particles and crystalline MoS₂ nanosheets formed at an early stage grows into a lateral direction and becomes more crystalline with aging (Fig. 2.4a and c). This growth process is similar to that of other transition metal selenide nanosheets.^[31] Apart from the aging time, it is also important to understand the role of solvents and precursors as can be seen in Fig. 2.5. The resulting colloidal MoS₂ nanosheets are well-dispersed in various organic solvents without any aggregation for a few weeks (Fig. 2.6), which is highly advantageous for further processing and device applications.

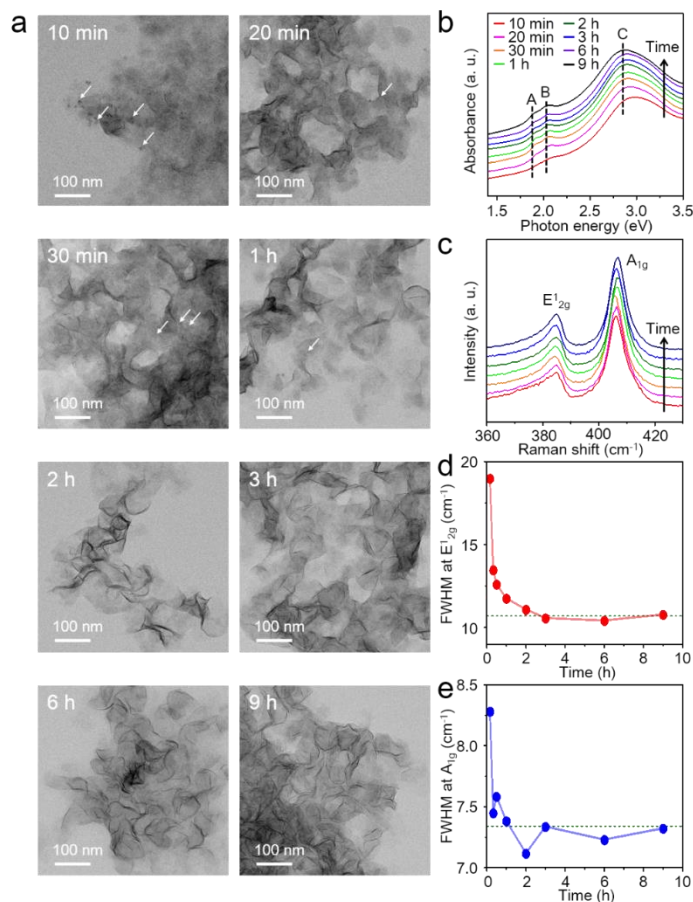


Figure 2.4 (a) TEM images, (b) UV-vis absorption spectra (c) Raman spectra of the aliquots extracted from the reaction batch along aging time. White arrows indicate the primary particles, which disappear during aging. Full-width at half maximum (FWHM) at (d) E_{2g}^1 and (e) A_{1g} is observed during reaction time. Saturated FWHM value is visualized by green dashed lines.

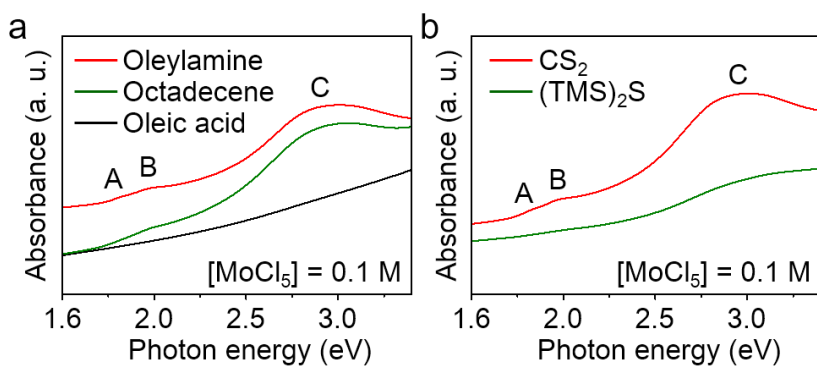


Figure 2.5 UV-vis spectra of the MoS₂ nanosheets, which were synthesized using different (a) solvents and (b) sulfur precursors ((TMS)₂S is the abbreviation of bis(trimethylsilyl)sulfide). When Oleylamine and CS₂ is used, typical absorption spectra of MoS₂ is observed, showing the high quality of synthesized MoS₂ nanosheets. Oleylamine acts as a both solvent and reducing agent, and CS₂ is the reactive precursors to successfully synthesize MoS₂ nanosheets.

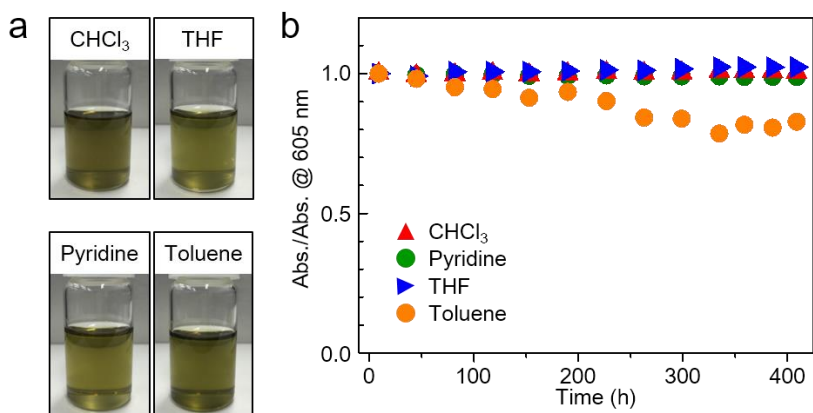


Figure 2.6 (a) Photographs of the MoS₂ nanosheets dispersed in 4 different organic solvents (CHCl₃, THF, pyridine, and toluene). (b) Normalized absorbance of MoS₂ nanosheets dispersion in 4 different organic solvents at 605 nm as a function of time. All absorbance values are divided by the intensities of corresponding solvent dispersions measured at the first time. Each MoS₂ nanosheets dispersion is stable for at least 400 h. Since MoS₂ nanosheets dispersed in toluene are readily adsorbed on the surface of a cuvette, absorbance decreases during each measurement, but no visible precipitation was observed.

The uniformity of semiconducting materials used in devices is an important factor affecting the performance and yield of microelectronics, particularly for mass-produced devices such as random access memory. To determine the uniformity of the synthesized MoS₂ nanosheets, their size and thickness distributions, and thereby their morphological uniformity, are characterized and compared to those of exfoliated MoS₂ using STEM and HRTEM. Fig. 2.7a shows that the average lateral size of the synthesized nanosheets is ~89 nm and that their size distribution is much narrower than that of the exfoliated MoS₂. The average layer number of the synthesized MoS₂ nanosheets also shows a smaller deviance than that of the exfoliated MoS₂ (Fig. 2.7b). Furthermore, the size and thickness distributions of three different batches of the synthesized MoS₂ nanosheets overlap each other, suggesting that the proposed synthesis method is highly reproducible (inset in Fig. 2.7b).

Fig. 2.8 reveals the characterization of MoS₂ nanosheets that were synthesized in large scale. The resultant MoS₂ nanosheets (named as L-MoS₂ nanosheets) present the similar UV-vis absorption spectrum to that of MoS₂ nanosheets synthesized in small scale, showing the comparable quality each other (Fig. 2.8c). The lateral size of the L-MoS₂ nanosheets increases, whereas their thickness retains as two layers. It may result

from the larger temperature gradient as the reaction volume increases, and the nucleation and growth mechanism get influenced during the formation of MoS₂ nanosheets.

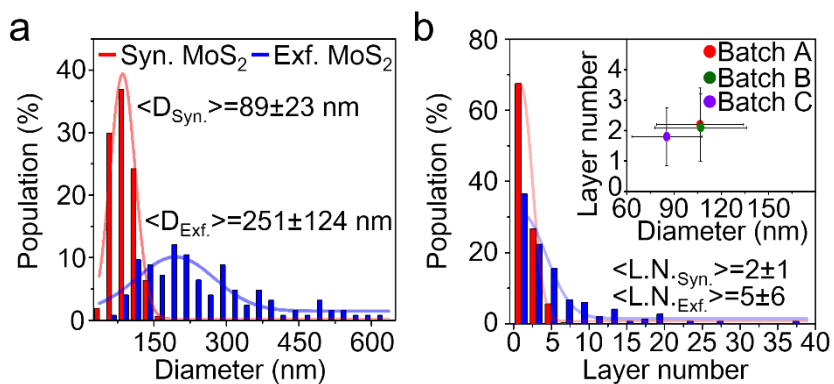


Figure 2.7 Statistical data of the (a) diameter and (b) number of layers of the synthesized (red) and exfoliated (blue) MoS₂ nanosheets. The inset in (b) shows the reproducibility, which was determined by measuring the diameter and number of layers of MoS₂ nanosheets produced from three different batches (red dot (batch A), green dot (batch B), purple dot (batch C)).

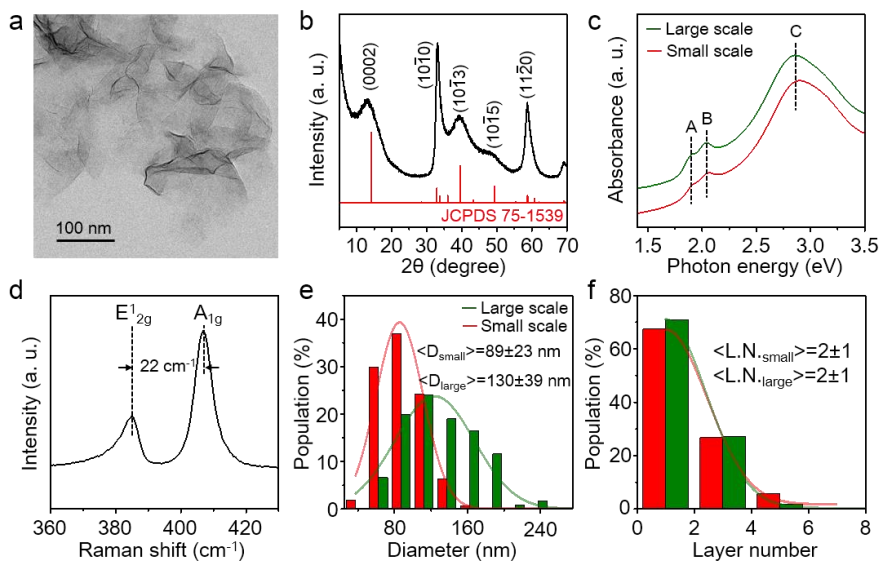


Figure 2.8 Fundamental properties of synthesized MoS₂ nanosheets produced in a scaled-up batch are measured through (a) TEM, (b) XRD, (c) UV-vis absorption spectroscopy, and (d) Raman spectroscopy. Statistical analysis of (e) size and (f) thickness distribution of MoS₂ nanosheets is performed. MoS₂ nanosheets with better crystallinity were synthesized through scale-up and similar relative standard deviations of both size and thickness of MoS₂ nanosheets were identified.

Uniform MoS₂ nanosheets can be used in various electronic devices.^[5,14,27,32] In this study, the next-generation nonvolatile data storage device, RRAM, is focused. MoS₂ nanosheets are assembled using a spray-coating method at a low temperature without additional surface treatment, which enables the facile fabrication on deformable plastic substrates. The optimized control of the junction interface of the MoS₂-MoO_x heterostructure, which contains defect-induced mobile carriers, enables the significant improvement of the RRAM performance. An ultrathin film of the layered MoS₂-MoO_x heterostructure is formed on a patterned Al bottom electrode through spray-coating and subsequent thermal annealing (200 °C, 3 h) of the synthesized MoS₂ nanosheets (Fig. 2.9a). This process oxidizes the surface of the MoS₂ nanosheets, thereby forming the heterostructure.^[19] The thermal evaporation and patterning of the Al top electrode completes the fabrication of the RRAM (Fig. 2.10). The HRTEM image in Fig. 2.9b shows the MoS₂-MoO_x heterostructure sandwiched between the top and bottom Al electrode. A similar structure is also fabricated using exfoliated MoS₂ (Fig. 2.11a) with the same fabrication process to serve as a control for the electrical characterization.

As can be seen from the current-voltage (I-V) curves (Fig. 2.9c and d), the initial state of the RRAM is the high-resistance state (HRS) and the application of a negative voltage (“SET”) causes a shift to a low-resistance state (LRS). A negative voltage (“RESET”) switches the device from the LRS back to the HRS. The I-V curves show unipolar-resistive-switching (URS) characteristics. The device without the MoS₂ nanosheets, *i.e.*, that with the Al-MoO_x-Al structure, does not show this switching behavior (Fig. 2.11b). The linear I-V curves are governed by ohmic conduction at low voltage (Fig. 2.11c and d) and by Poole-Frenkel emission at high voltage (Fig. 2.11e and f).^[33] This can be ascribed to the defect-induced mobile carriers in the MoS₂-MoO_x heterostructure and the Schottky barrier modulation between the Al electrode and the MoO_x layer.

The switching mechanism of the MoS₂-MoO_x heterostructure can be explained based on the migration of the oxygen vacancies. After spray-coating and the subsequent annealing process, the MoS₂-MoO_x heterostructure is formed. This heterostructure contains abundant oxygen vacancies, which act as electron-trapping sites. When a negative bias is applied to the top Al electrode under a compliance current (I_{cc}) of -1 mA, the oxygen vacancies move to the top electrode and become

aligned, forming a conducting filament. An ohmic contact is formed at the Al electrode/MoS₂ interface, since the work function of Al (4.3 eV) is similar to the conduction band minimum of MoS₂ (4.2 eV). MoS₂ plays a critical role as a buffer layer, providing electrons. The conduction mechanism can be better understood through an analysis of the I-V characteristics (Fig. 2.9c and d). Fig. 2.11c and d show the I-V characteristics plotted using log scales. Both the LRS and the HRS have linear regions with slopes of ~1. However, the HRS has a nonlinear region in the high-voltage region. This indicates that both the LRS and the HRS exhibit Ohmic behavior in the low-voltage regime and additional conduction mechanisms govern the HRS in the high-voltage regime. Fig. 2.11e and f suggest that the device exhibits the Poole-Frenkel emission at high voltages, which is primarily caused by the electrons hopping between the trap sites.^[33-35] When a negative bias is applied to the top Al electrode, the conducting filaments are ruptured by the Joule heating effect.

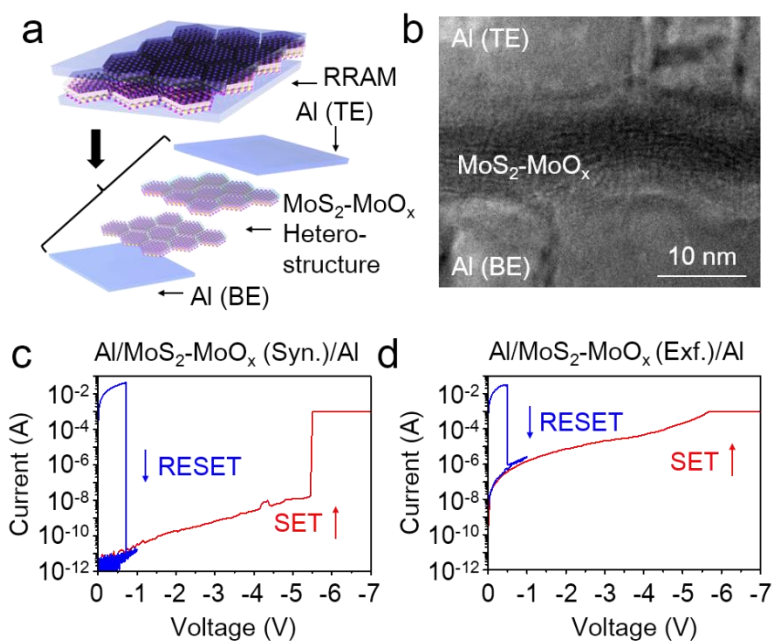


Figure 2.9 Resistive switching of the MoS₂-MoO_x heterostructure. (a) Schematic illustration of the RRAM (top) and an exploded view showing the layered structures (bottom). The layered MoS₂-MoO_x heterostructure is sandwiched between the top and bottom Al electrode. (b) Cross-sectional TEM image of the synthesized MoS₂ RRAM device. I-V characteristics of the RRAM devices based on (c) the synthesized and (d) exfoliated MoS₂ nanosheets. The SET (red) and RESET (blue) operations of each device exhibit the URS behavior. The SET operation is performed under a compliance current of -1 mA.

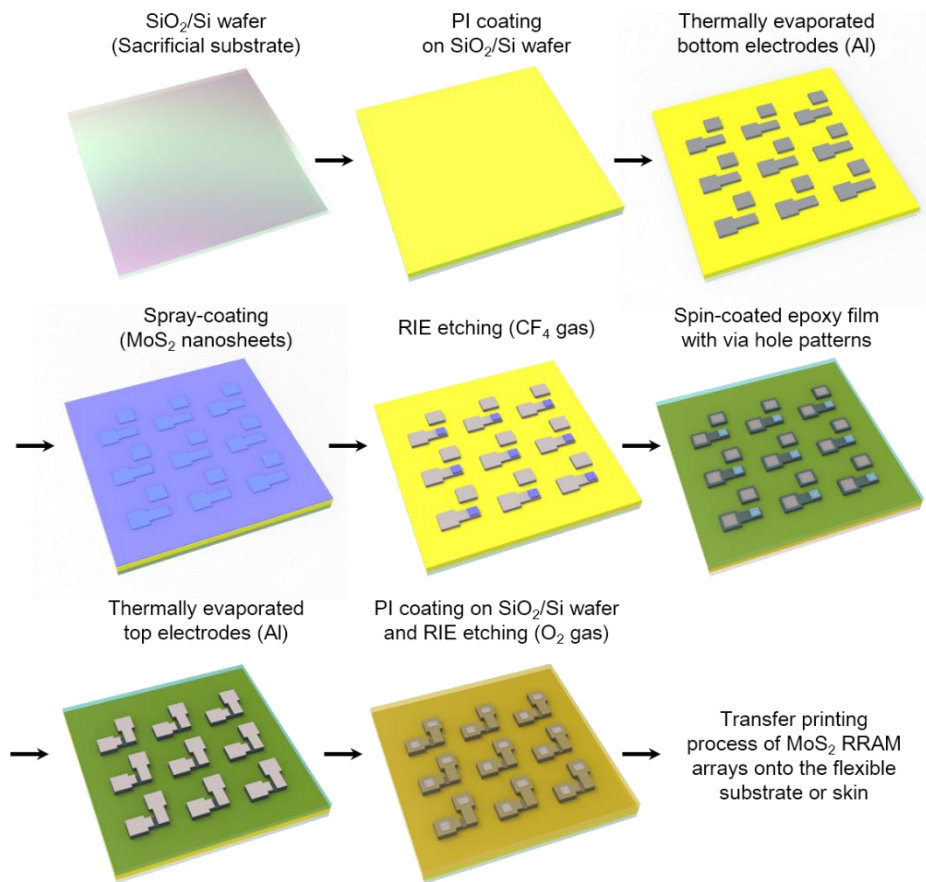


Figure 2.10 The bottom Al electrodes are firstly deposited and patterned on a PI/SiO₂/Si substrate, followed by spray-coating of the MoS₂ nanosheets. The nanosheets are subsequently patterned by RIE, and the epoxy film with via-holes is then generated. The top Al electrodes are deposited and patterned, and finally, a top PI layer is coated and the devices are transferred onto a flexible substrate.

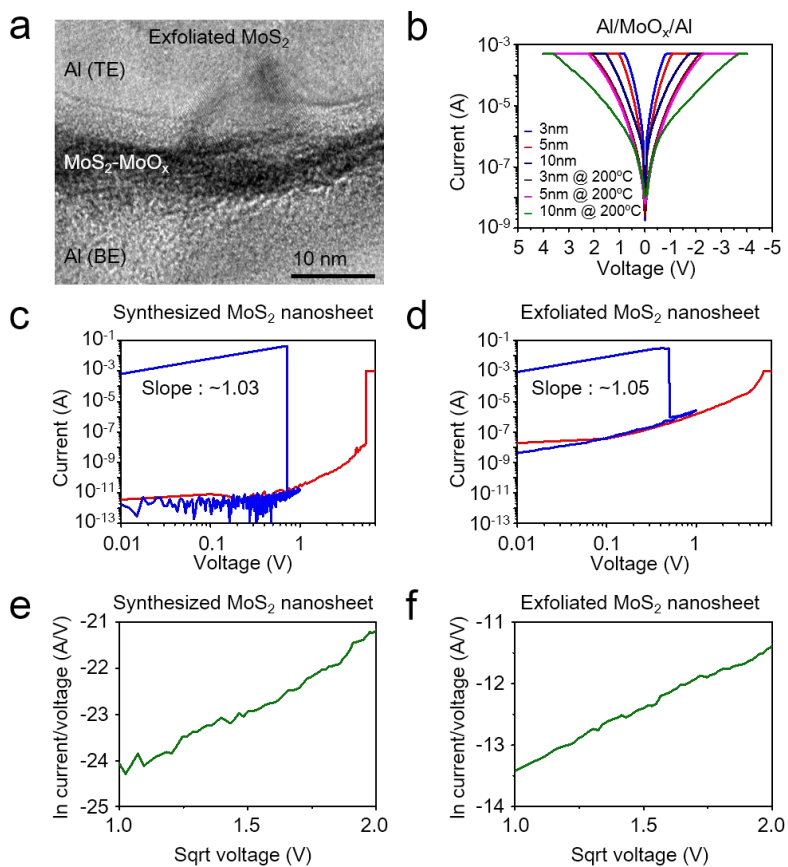


Figure 2.11 (a) A cross-sectional TEM image of the exfoliated MoS₂ RRAM device. (b) I-V characteristics of the device without the MoS₂ nanosheets. Log-log plots showing the HRS and LRS of (c) synthesized MoS₂ RRAM and (d) exfoliated MoS₂ RRAM. The plot of $\ln(I/V)$ as a function of the square root of V for (e) the synthesized MoS₂ RRAM and (f) the exfoliated MoS₂ RRAM. The linear fits show a Poole-Frenkel emission.

Several important performance factors of the RRAM are evaluated. The most noticeable point is the high on/off ratio of the synthesized MoS₂ RRAM, which is ~10,000 times higher than that of the memory based on exfoliated MoS₂ (Fig. 2.9c and d). This dramatic increase is attributed to the high density of oxidative sites in the synthesized MoS₂-MoO_x heterostructure, which increases the resistance in the low-voltage region. In that regard, the XPS depth profile confirms that the Mo⁶⁺ oxidation states of the synthesized MoS₂-MoO_x heterostructure are more densely populated than those of the exfoliated one (Fig. 2.12a). The high density of oxidative sites seems to be derived from the polycrystalline nature of the MoS₂ nanosheets, which have defect sites that are observed in the atomic-resolution STEM images (Fig. 2.2). The retention properties of the synthesized MoS₂ RRAM are characterized at elevated temperatures (85 and 150 °C). A retention time reaching 10,000 s is confirmed (Fig. 2.12b). Furthermore, the device exhibits reliable performance under repetitive sweeping over 100 cycles (inset in Fig. 2.12b).

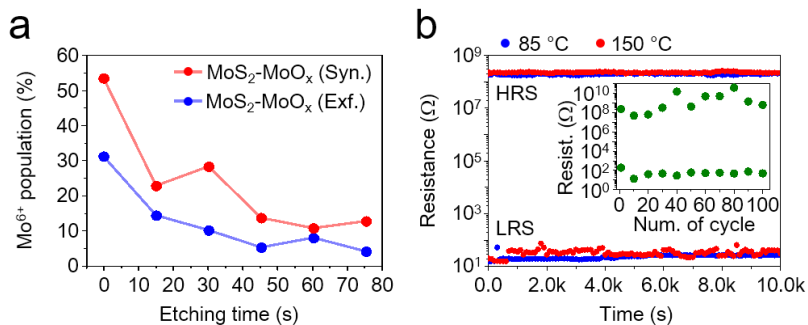


Figure 2.12 (a) Depth profiles of the Mo⁶⁺ population in the synthesized and the exfoliated MoS₂-MoO_x heterostructures. (b) Retention test of the RRAM based on the synthesized MoS₂ nanosheets at 85 and 150 °C. The inset shows the endurance performance under repetitive sweeping for 100 cycles at a read voltage of -0.1 V.

Scaling down device dimensions to the nanometer scale is important from a practical viewpoint. Conducting atomic force microscopy (CAFM) is used to verify the generation of conducting filaments at the submicron scale (Fig. 2.13).^[36] The density of the conducting filaments in the synthesized MoS₂-MoO_x heterostructure is high enough for the nanoscale operation of RRAM. The conducting filaments can be eliminated locally under the RESET bias (Fig. 2.13a).

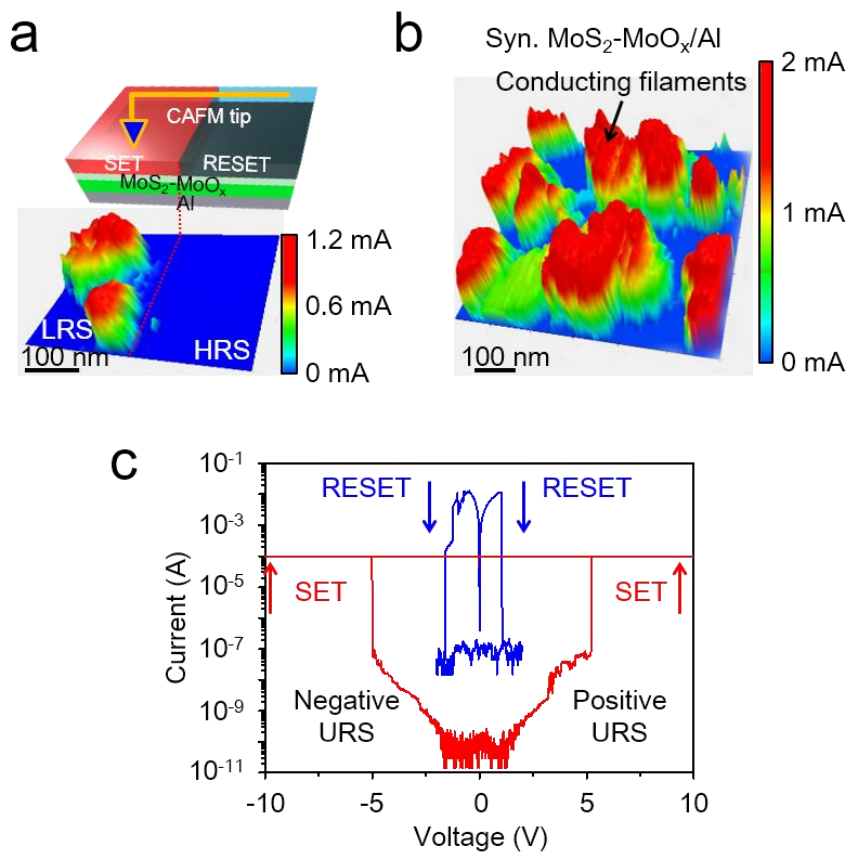


Figure 2.13 (a) CAFM analysis of the synthesized MoS₂ RRAM, which shows locally eliminated conducting filaments. (b) CAFM analysis of the synthesized MoS₂-MoO_x heterostructure in the LRS region. (c) I-V characteristics of the synthesized MoS₂ RRAM using a top Pt electrode.

Wafer-scale RRAM devices composed of 9 crossbar arrays (10×10 for each array) and 18,566 individual cells are shown in Fig. 2.14a. Photographs and magnified optical microscope images of the dotted box regions are shown in Fig. 2.14b and c. The spray-coating process is extremely advantageous in terms of scalability and throughput. Thus, this process is more suitable for highly uniform assembly of the synthesized MoS₂ nanosheets on 4-inch wafers than spin-coating method.^[37] The uniformity of the material properties of the assembled film is analyzed at five representative points of the 4-inch wafer (Fig. 2.15a) using Raman spectroscopy (Fig. 2.15a) and XPS (Fig. 2.15b). The E_{2g}¹ and A_{1g} Raman peaks and the Mo 3d and S 2s XPS peaks for the five locations are almost identical. The Mo 3d peaks correspond to the higher oxidation states of the MoS₂-MoO_x heterostructure. The assembled MoS₂-MoO_x film can be patterned using high-resolution photolithography and CF₄ plasma etching (Fig. 2.16). Although the film thickness of the spray-coated MoS₂-MoO_x heterostructure varies between tens and hundreds of nanometers (Fig. 2.17), the RRAM shows uniform electrical characteristics (Fig. 2.18), since the critical operation of the RRAM occurs at the junction interface. The uniformity of the film thickness can be improved using other integration processes such as the

wafer-scale Langmuir Blodgett assembly method.^[8] According to statistical data, the on/off ratio of the synthesized MoS₂ RRAM in the array is much higher than that of the device based on exfoliated MoS₂ (Fig. 2.18a), even though their operational voltages are similar (Fig. 2.18b). Furthermore, the statistical results indicate typical filamentary resistive switching behavior, since the LRS and HRS are independent of the cell area (Fig. 2.19a and b).^[38] The device characteristics of the 10 × 10 crossbar RRAM array are similar to those of the individual cells (Fig. 2.19c and d).

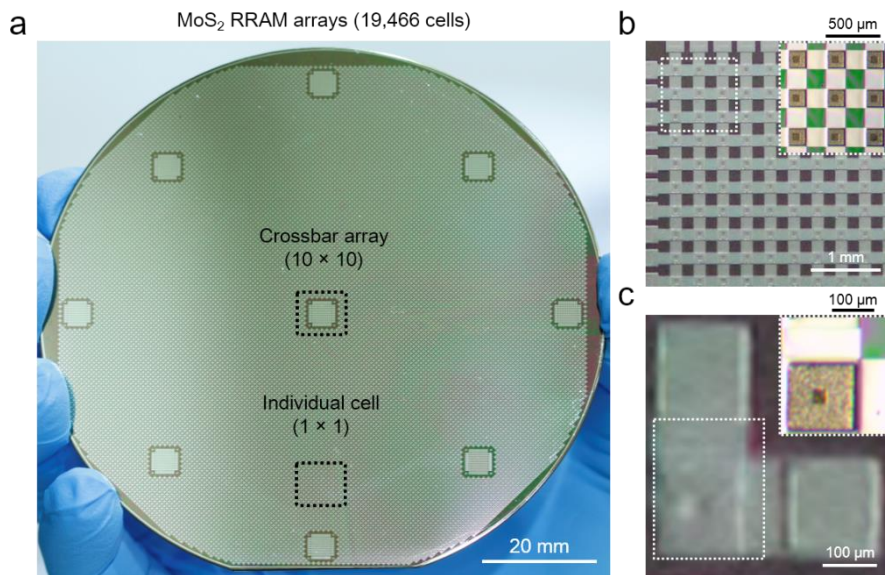


Figure 2.14 (a) An image of wafer-scale MoS₂ RRAM arrays composed of 9 crossbar arrays (10 × 10) and 18,566 individual cells. A magnified image of (b) a crossbar array (10 × 10) and (c) an individual cell. The inset in (b) and (c) shows a microscope image. The area of the cell is 3600 μm² in the crossbar array and 900 μm² in an individual cell.

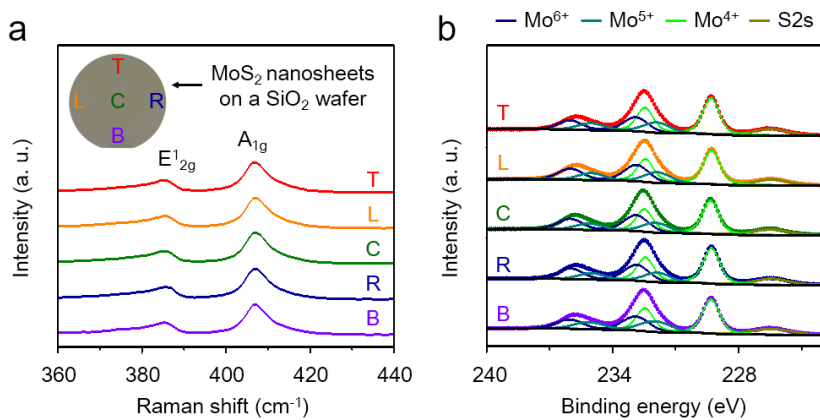


Figure 2.15 (a) Raman and (b) XPS spectra of a film of the MoS₂-MoO_x heterostructure assembled by the spray-coating on a Si wafer, showing good uniformity at five different points (T (top), L (left), C (center), R (right), and B (bottom)); inset). XPS peaks were deconvoluted to show oxidation states of molybdenum.

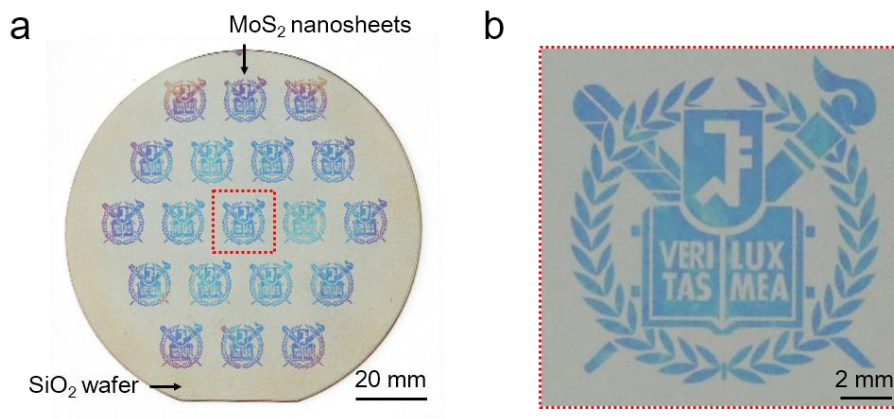


Figure 2.16 (a) An image taken using an optical camera and (b) an enlarged image of the dotted box. The MoS₂-MoO_x layer is patterned by standard photolithography and RIE (CF₄ plasma).

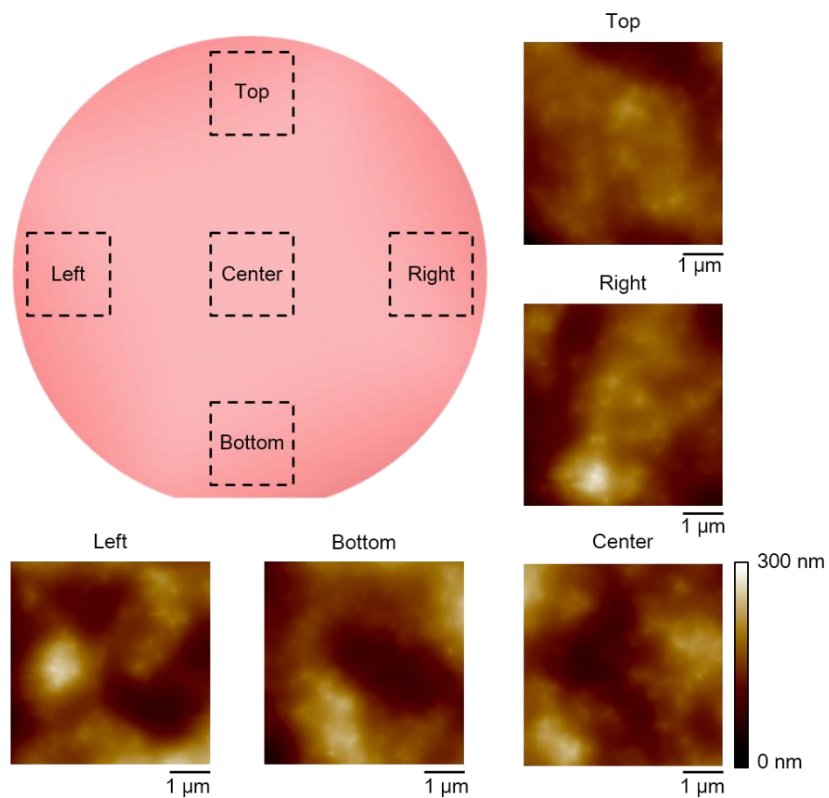


Figure 2.17 Atomic force microscopy (AFM) analysis of the spray-coated MoS₂. The film thicknesses of the spray-coated MoS₂-MoO_x are measured at five different regions.

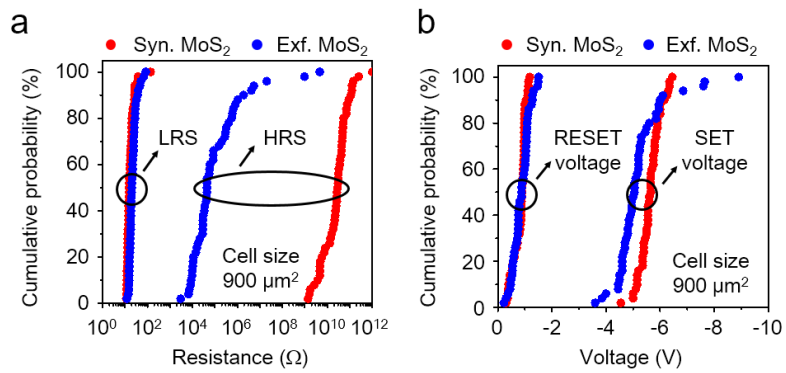


Figure 2.18 The cumulative probability of the (a) resistance and (b) switching voltage for the RRAM devices based on the synthesized (red, 50 cells) and exfoliated (blue, 50 cells) MoS₂ nanosheets.

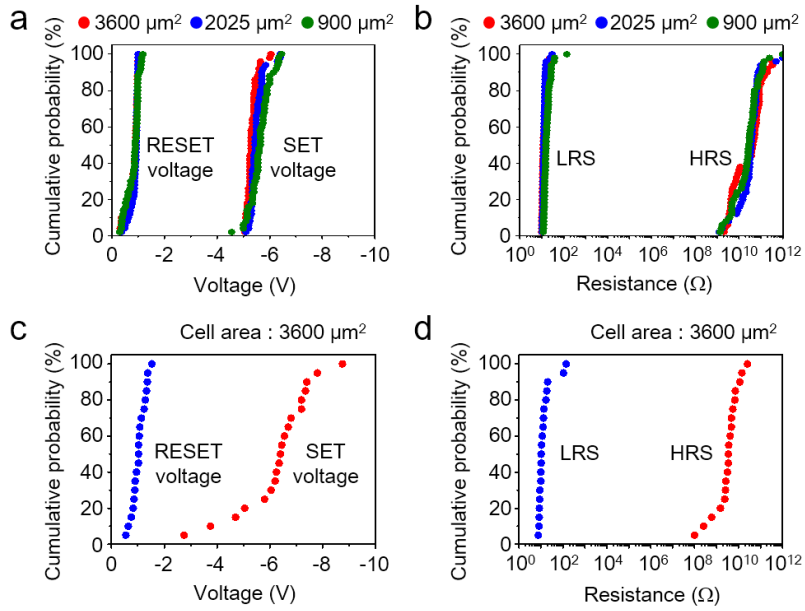


Figure 2.19 Cumulative probability plot of (a) the switching voltage and (b) resistance at a read voltage of -0.1 V measured from the synthesized MoS_2 RRAM devices. There are three different cell sizes and 50 cells from each size were randomly measured. Cumulative probability plot of (c) the switching voltage and (d) resistance at a read voltage -0.1 V measured from the crossbar arrays (10×10) of the synthesized MoS_2 RRAM. 20 cells were randomly measured.

The ultrathin nature of the MoS₂ RRAM devices makes them suitable for various applications, including deformable and/or wearable electronics.^[39-42] Fig. 2.20 shows a deformed RRAM array on a flexible polyethylene terephthalate (PET) substrate. As the substrate becomes thinner, the RRAM array becomes ultradeformable and can be laminated over curvilinear surfaces such as human skin (Fig. 2.21a). The ultralow thickness also minimizes the overall weight dramatically (Fig. 2.21b and d). To characterize the mechanical deformability of the memory array, the strain distribution on the surface of the MoS₂-MoO_x heterostructure is estimated through a finite element analysis (FEA; Fig. 2.22). The minimization of the induced strains by using ultrathin and neutral mechanical plane designs results in good device performance even after repetitive deformation with a bending radius as low as 3 mm (Fig. 2.22).

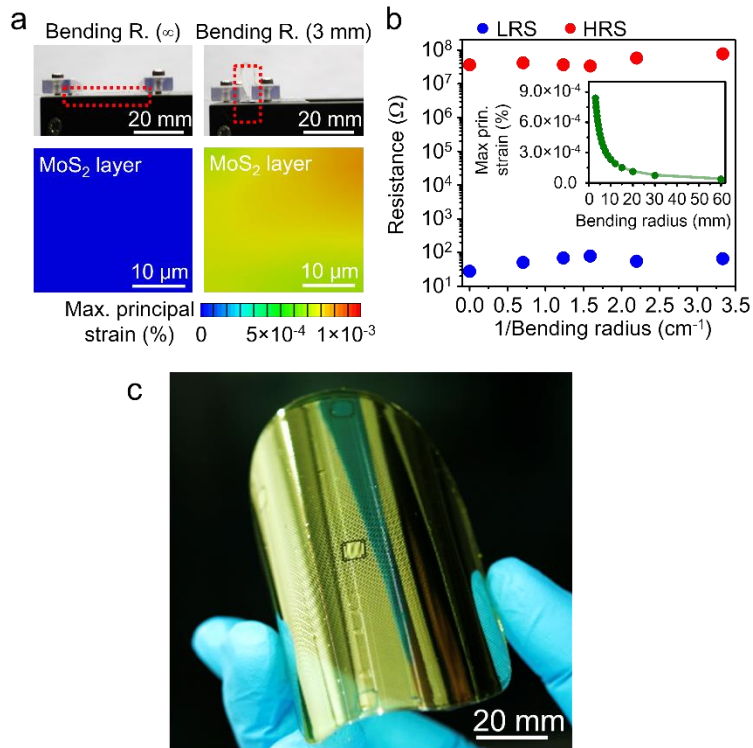


Figure 2.20 (a) Bending test images (top) of the MoS₂ RRAM device and the corresponding strain distributions (bottom) obtained through FEA at the bending radii of ∞ to 3 mm. (b) The resistance of the MoS₂ RRAM device as a function of the inverse of the bending radius, showing that both the LRS and the HRS are maintained even after the flexible device has been bent with a radius as small as 3 mm. A plot of the maximum principal strain of the MoS₂-MoO_x heterostructure as a function of the bending radius is shown in the inset. (c) A photograph of the flexible MoS₂ RRAM arrays formed on a PET substrate.

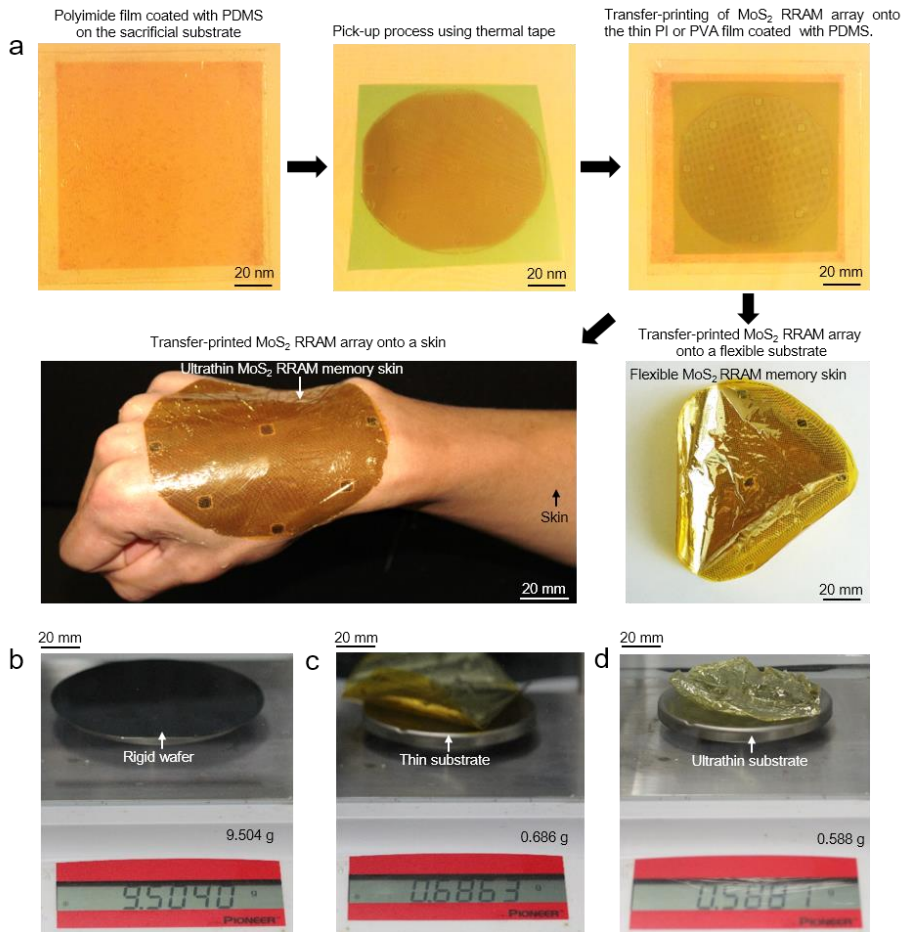


Figure 2.21 (a) Images of the transfer process of the MoS₂ array from the mother substrate onto skin using a thermal release tape. The weight of the RRAM arrays on (b) a rigid substrate (PI/RRAM/PI/SiO₂/Si wafer), (c) a thin PI film (PI/RRAM/PI/PI film) and (d) an ultrathin substrate (PI/RRAM/PI).

2.4 Conclusion

In summary, uniform colloidal MoS₂ nanosheets were synthesized at large-scale by using a hot-injection process, and their physical and chemical properties were extensively characterized by TEM, XRD, XPS, and UV-vis and Raman spectroscopy. The statistical analysis of the characterization data confirmed that the synthesized MoS₂ nanosheets exhibit significantly higher morphological uniformity than exfoliated MoS₂. Such material uniformity allowed the wafer-scale fabrication of a MoS₂ RRAM array with excellent and uniform performance. It also enables the fabrication of a novel flexible data storage. These advances will provide many new opportunities in the fabrication of wearable and/or mobile electronics.

Parts of this chapter were published in the article, “Colloidal Synthesis of Uniform-Sized Molybdenum Disulfide Nanosheets for Wafer-Scale Flexible Nonvolatile Memory.” (*Advanced Materials* **2016, 28, 9326)

2.5 References

- [1] Jin, S. H.; Dunham, S. N.; Song, J.; Xie, X.; Kim, J.-H.; Lu, C.; Islam, A.; Du, F.; Kim, J.; Felts, J.; Li, Y.; Xiong, F.; Wahab, M. A.; Menon, M.; Cho, E.; Grosse, K. L.; Lee, D. J.; Chung, H. U.; Pop, E.; Alam, M. A.; King, W. P.; Huang, Y.; Rogers, J. A. Using nanoscale thermocapillary flows to create arrays of purely semiconducting single-walled carbon nanotubes. *Nat. Nanotechnol.* **2013**, *8*, 347.
- [2] Tao, L.; Cinquanta, E.; Chiappe, D.; Grazianetti, C.; Fanciulli, M.; Dubey, M.; Molle, A.; Akinwande, D. Silicene field-effect transistors operating at room temperature. *Nat. Nanotechnol.* **2015**, *10*, 227.
- [3] Cheng, R.; Jiang, S.; Chen, Y.; Liu, Y.; Weiss, N.; Cheng, H.-C.; Wu, H.; Huang, Y.; Duan, X. Few-layer molybdenum disulfide transistors and circuits for high-speed flexible electronics. *Nat. Commun.* **2014**, *5*, 5143.
- [4] Nayak, A. P.; Pandey, T.; Voiry, D.; Liu, J.; Moran, S. T.; Sharma, A.; Tan, C.; Chen, C.-H.; Li, L.-J.; Chhowalla, M.; Lin, J.-F.; Singh, A. K.; Akinwande, D. Pressure-dependent optical and vibrational properties of monolayer molybdenum disulfide. *Nano Lett.* **2015**, *15*, 346.

- [5] Lopez-Sanchez, O.; Lembke, D.; Kayci, M.; Radenovic, A.; Kis, A. Ultrasensitive photodetectors based on monolayer MoS₂. *Nat. Nanotechnol.* **2013**, *8*, 497.
- [6] Tee, B. C.-K.; Chortos, A.; Berndt, A.; Nguyen, A. K.; Tom, A.; McGuire, A.; Lin, Z. C.; Tien, K.; Bae, W.-G.; Wang, H.; Mei, P.; Chou, H.-H.; Cui, B.; Deisseroth, K.; Ng, T. N.; Bao, Z. A skin-inspired organic digital mechanoreceptor. *Science* **2015**, *350*, 313.
- [7] Kim, D.-H.; Lu, N.; Ma, R.; Kim, Y.-S.; Kim, R.-H.; Wang, S.; Wu, J.; Won, S. M.; Tao, H.; Islam, A.; Yu, K. J.; Kim, T.-I.; Chowdhury, R.; Ying, M.; Xu, L.; Li, M.; Chung, H.-J.; Keum, H.; McCormick, M.; Liu, P.; Zhang, Y.-W.; Omenetto, F. G.; Huang, Y.; Coleman, T.; Rogers, J. A. Epidermal electronics. *Science* **2011**, *333*, 838.
- [8] Son, D.; Lee, J.; Qiao, S.; Ghaffari, R.; Kim, J.; Lee, J. E.; Song, C.; Kim, S. J.; Lee, D. J.; Jun, S. W.; Yang, S.; Park, M.; Shin, J.; Do, K.; Lee, M.; Kang, K.; Hwang, C. S.; Lu, N.; Hyeon, T.; Kim, D.-H. Multifunctional wearable devices for diagnosis and therapy of movement disorders. *Nat. Nanotechnol.* **2014**, *9*, 397.
- [9] Kaltenbrunner, M.; Sekitani, T.; Reeder, J.; Yokota, T.; Kuribara, K.; Tokuhara, T.; Drack, M.; Schwödiauer, R.; Graz, I.; Bauer-Gogonea, S.; Bauer, S.; Someya, T. An ultra-lightweight design for

- imperceptible plastic electronics. *Nature* **2013**, *499*, 458.
- [10] Sekitani, T.; Yokota, T.; Zschieschang, U.; Klauk, H.; Bauer, S.; Takeuchi, K.; Takamiya, M.; Sakurai, T.; Someya, T. Organic nonvolatile memory transistors for flexible sensor arrays. *Science* **2009**, *326*, 1516.
- [11] Eda, G.; Yamaguchi, H.; Voiry, D.; Fujita, T.; Chen, M.; Chhowalla, M. Photoluminescence from chemically exfoliated MoS₂. *Nano Lett.* **2011**, *11*, 5111.
- [12] Wu, S.; Ross, J. S.; Liu, G.-B.; Aivazian, G.; Jones, A.; Fei, Z.; Zhu, W.; Xiao, D.; Yao, W.; Cobden, D.; Xu, X. Electrical tuning of valley magnetic moment through symmetry control in bilayer MoS₂. *Nat. Phys.* **2013**, *9*, 149.
- [13] Kang, K.; Xie, S.; Huang, L.; Han, Y.; Huang, P. Y.; Mak, K. F.; Kim, C.-J.; Muller, D.; Park, J. High-mobility three-atom-thick semiconducting films with wafer-scale homogeneity. *Nature* **2015**, *520*, 656.
- [14] Radisavljevic, B.; Radenovic, A.; Brivio, J.; Giacometti, V.; Kis, A. Single-layer MoS₂ transistors. *Nat. Nanotechnol.* **2011**, *6*, 147.
- [15] Wu, W.; Wang, L.; Li, Y.; Zhang, F.; Lin, L.; Niu, S.; Chenet, D.; Zhang, X.; Hao, Y.; Heinz, T. F.; Hone, J.; Wang, Z. L.

- Piezoelectricity of single-atomic-layer MoS₂ for energy conversion and piezotronics. *Nature* **2014**, *514*, 470.
- [16] Novoselov, K. S.; Jiang, D.; Schedin, F.; Booth, T. J.; Khotkevich, V. V.; Morozov, S. V.; Geim, A. K. Two-dimensional atomic crystals. *Proc. Natl. Acad. Sci. U.S.A.* **2005**, *102*, 10451.
- [17] Splendiani, A.; Sun, L.; Zhang, Y.; Li, T.; Kim, J.; Chim, C.-Y.; Galli, G.; Wang, F. Emerging photoluminescence in monolayer MoS₂. *Nano Lett.* **2010**, *10*, 1271.
- [18] Amani, M.; Lien, D.-H.; Kiriya, D.; Xiao, J.; Azcatl, A.; Noh, J.; Madhvapathy, S. R.; Addou, R.; Santosh, K. C.; Dubey, M.; Cho, K.; Wallace, R. M.; Lee, S.-C.; He, J.-H.; Ager, J. W.; Zhang, X.; Yablonovitch, E.; Javey, A. Near-unity photoluminescence quantum yield in MoS₂. *Science* **2015**, *350*, 1065.
- [19] Bessonov, A. A.; Kirikova, M. N.; Petukhov, D. I.; Allen, M.; Ryhanen, T.; Bailey, M. J. A. Layered memristive and memcapacitive switches for printable electronics. *Nat. Mater.* **2015**, *14*, 199.
- [20] Kwon, J.; Hong, Y. K.; Han, G.; Omkaram, I.; Choi, W.; Kim, S.; Yoon, Y. Giant photoamplification in indirect-bandgap multilayer MoS₂ phototransistors with local bottom-gate structures. *Adv. Mater.*

2015, 27, 2224.

- [21] Roy, T.; Tosun, M.; Cao, X.; Fang, H.; Lien, D.-H.; Zhao, P.; Chen, Y.-Z.; Chueh, Y.-L.; Guo, J.; Javey, A. Dual-gated MoS₂/WSe₂ van der Waals tunnel diodes and transistors. *ACS Nano* **2015**, 9, 2071.
- [22] Coleman, J. N.; Lotya, M.; O'Neill, A.; Bergin, S. D.; King, P. J.; Khan, U.; Young, K.; Gaucher, A.; De, S.; Smith, R. J.; Shvets, I. V.; Arora, S. K.; Stanton, G.; Kim, H.-Y.; Lee, K.; Kim, G. T.; Duesberg, G. S.; Hallam, T.; Boland, J. J.; Wang, J. J.; Donegan, J. F.; Grunlan, J. C.; Moriarty, G.; Shmeliov, A.; Nicholls, R. J.; Perkins, J. M.; Grievson, E. M.; Theuwissen, K.; McComb, D. W.; Nellist, P. D.; Nicolosi, V. Two-dimensional nanosheets produced by liquid exfoliation of layered materials. *Science* **2011**, 331, 568.
- [23] Jeong, S.; Yoo, D.; Ahn, M.; Miro, P.; Heine, T.; Cheon, J. Tandem intercalation strategy for single-layer nanosheets as an effective alternative to conventional exfoliation processes. *Nat. Commun.* **2015**, 6, 5763.
- [24] Ithurria, S.; Tessier, M. D.; Mahler, B.; Lobo, R. P. S. M.; Dubertret, B.; Efron, A. L. Colloidal nanoplatelets with two-dimensional electronic structure. *Nat. Mater.* **2011**, 10, 936.
- [25] Lhuillier, E.; Pedetti, S.; Ithurria, S.; Heuclin, H.; Nadal, B.; Robin,

- A.; Patriarche, G.; Lequeux, N.; Dubertret, B. Electrolyte-gated field effect transistor to probe the surface defects and morphology in films of thick CdSe colloidal nanoplatelets. *ACS Nano* **2014**, *8*, 3813.
- [26] Wang, H.; Meng, F.; Zhu, B.; Leow, W. R.; Liu, Y.; Chen, X. Resistive Switching Memory Devices Based on Proteins. *Adv. Mater.* **2015**, *27*, 7670.
- [27] Tan, C.; Liu, Z.; Huang, W.; Zhang, H. Non-volatile resistive memory devices based on solution-processed ultrathin two-dimensional nanomaterials. *Chem. Soc. Rev.* **2015**, *44*, 2615.
- [28] Chianelli, R. R.; Prestridge, E. B.; Pecoraro, T. A.; Deneufville, J. P. Molybdenum disulfide in the poorly crystalline "rag" structure. *Science* **1979**, *203*, 1105.
- [29] Li, H.; Zhang, Q.; Yap, C. C. R.; Tay, B. K.; Edwin, T. H. T.; Olivier, A.; Baillargeat, D. From Bulk to Monolayer MoS₂: Evolution of Raman Scattering. *Adv. Funct. Mater.* **2012**, *22*, 1385.
- [30] Hong, J.; Hu, Z.; Probert, M.; Li, K.; Lv, D.; Yang, X.; Gu, L.; Mao, N.; Feng, Q.; Xie, L.; Zhang, J.; Wu, D.; Zhang, Z.; Jin, C.; Ji, W.; Zhang, X.; Yuan, J.; Zhang, Z. Exploring atomic defects in molybdenum disulphide monolayers. *Nat. Commun.* **2015**, *6*, 6293.

- [31] Jung, W.; Lee, S.; Yoo, D.; Jeong, S.; Miro, P.; Kuc, A.; Heine, T.; Cheon, J. Colloidal synthesis of single-layer MSe_2 ($M = Mo, W$) nanosheets via anisotropic solution-phase growth approach. *J. Am. Chem. Soc.* **2015**, *137*, 7266.
- [32] Yin, Z.; Li, H.; Li, H.; Jiang, L.; Shi, Y.; Sun, Y.; Lu, G.; Zhang, Q.; Chen, X.; Zhang, H. Single-layer MoS_2 phototransistors. *ACS Nano* **2012**, *6*, 74.
- [33] Lee, S.; Kim, H.; Yun, D.-J.; Rhee, S.-W.; Yong, K. Resistive switching characteristics of ZnO thin film grown on stainless steel for flexible nonvolatile memory devices. *Appl. Phys. Lett.* **2009**, *95*, 262113.
- [34] Lin, C.-C.; Tseng, Z.-L.; Lo, K.-Y.; Huang, C.-Y.; Hong, C.-S.; Chu, S.-Y.; Chang, C.-C.; Wu, C.-J. Unipolar resistive switching behavior of $Pt/Li_xZn_{1-x}O/Pt$ resistive random access memory devices controlled by various defect types. *Appl. Phys. Lett.* **2012**, *101*, 203501.
- [35] Kukreja, L. M.; Das, A. K.; Misra, P. Studies on nonvolatile resistance memory switching in ZnO thin films. *Bull. Mater. Sci.* **2009**, *32*, 247.
- [36] Cho, B.; Yun, J.-M.; Song, S.; Ji, Y.; Kim, D.-Y.; Lee, T. Direct

- Observation of Ag Filamentary Paths in Organic Resistive Memory Devices. *Adv. Funct. Mater.* **2011**, *21*, 3976.
- [37] Yang, J.; Gu, Y.; Lee, E.; Lee, H.; Park, S. H.; Cho, M.-H.; Kim, Y. H.; Kim, Y.-H.; Kim, H. Wafer-scale synthesis of thickness-controllable MoS₂ films via solution-processing using a dimethylformamide/n-butylamine/2-aminoethanol solvent system. *Nanoscale* **2015**, *7*, 9311.
- [38] Sawa, A. Resistive switching in transition metal oxides. *Mater. Today* **2008**, *11*, 28.
- [39] Kim, J.; Lee, M.; Shim, H. J.; Ghaffari, R.; Cho, H. R.; Son, D.; Jung, Y. H.; Soh, M.; Choi, C.; Jung, S.; Chu, K.; Jeon, D.; Lee, S.-T.; Kim, J. H.; Choi, S. H.; Hyeon, T.; Kim, D.-H. Stretchable silicon nanoribbon electronics for skin prosthesis. *Nat. Commun.* **2014**, *5*, 5747.
- [40] Lee, H.; Choi, T. K.; Lee, Y. B.; Cho, H. R.; Ghaffari, R.; Wang, L.; Choi, H. J.; Chung, T. D.; Lu, N.; Hyeon, T.; Choi, S. H.; Kim, D.-H. A graphene-based electrochemical device with thermoresponsive microneedles for diabetes monitoring and therapy. *Nat. Nanotechnol.* **2016**, *11*, 566.
- [41] Kim, J.; Son, D.; Lee, M.; Song, C.; Song, J.-K.; Koo, J. H.; Lee, D.

J.; Shim, H. J.; Kim, J. H.; Lee, M.; Hyeon, T.; Kim, D.-H. A wearable multiplexed silicon nonvolatile memory array using nanocrystal charge confinement. *Sci. Adv.* **2016**, *2*, e1501101.

[42] Schwartz, G.; Tee, B. C.-K.; Mei, J.; Appleton, A. L.; Kim, D. H.; Wang, H.; Bao, Z. Flexible polymer transistors with high pressure sensitivity for application in electronic skin and health monitoring. *Nat. Commun.* **2013**, *4*, 1859.

Chapter 3. Synthesis and Surface Treatment of SnSe Nanoplates for Thermoelectric Application

3.1 Introduction

Over the past decades, nanochemistry has provided effective ways to synthesize inorganic semiconductor nanomaterials with unique properties resulting from particular structures and compositions.^[1-2] Recently, controlling the defects such as point defects (doping), dislocations, and grain boundaries in nanocrystals has emerged as an important issue.^[3-4] Defects have profound effects on all physicochemical properties of a material, thus serving as a tool to achieve the performance of the nanocrystals required for a variety of applications including catalysts,^[5-6] optics,^[7] and thermoelectric devices.^[8-11] For examples, the nanocrystals with stacking faults and twin boundaries, where thermal transport is hindered, have resulted in the decrease of thermal conductivity, thereby improving the thermoelectric efficiency.^[8,11] In this regard, the development of the synthetic methods for defect-introduced nanomaterials is one of the important goals in nanoscience.

Aside from the defect engineering of the inorganic nanocrystals, optimizing the surface chemistry of nanocrystals is another critical step toward obtaining high-quality materials for their use in many applications.^[12] Typically, on the surface of the nanocrystals synthesized through colloidal chemistry, surfactants used to control the formation of nanocrystals remain and provide colloidal stability. However, they can limit interparticle connectivity and impede the access of reactants toward the nanocrystal surface, making it detrimental to use in optoelectronics,^[13–15] thermoelectrics,^[8,16–20] and catalysis.^[21] Therefore, surface treatment to remove surfactants has continuously been in demand. In addition, it has increasingly become clear that the surface chemistry of nanocrystals can act as a powerful platform to influence the properties of nanocrystals. Current studies have revealed that surface reactions for the introduction of various organic and inorganic ligands can be employed to control the physical properties of nanocrystals such as absolute energy levels,^[22] doping levels,^[18,23] and carrier types.^[24] Further, the surface ligands of the nanocrystals affect the sintering behavior of the nanocrystals^[25] and also provide additional functionalities by generating structural disorders^[19] and secondary

phases.^[20] Accordingly, the control of surface ligands is important and highly desired to achieve high performance device.

Recently, tin selenide (SnSe) nanocrystals have attracted considerable attention as a promising p-type IV–VI semiconductor that can replace nanocrystals containing cadmium and lead due to their earth abundance and low toxicity. The absorption of SnSe nanocrystals in the near-infrared spectral region has made them potential in optoelectronics.^[26–28] Moreover, recent reports have demonstrated the remarkable thermoelectric performance of SnSe crystals due to their unique band structure and structural chemistry and led to the research on SnSe nanocrystals as thermoelectric materials.^[29–30]

Herein, we will demonstrate the large-scale colloidal synthesis of dislocation-introduced SnSe nanoplates *via* a facile heat-up method and effective surface treatment to enhance thermoelectric performance. Using transmission electron microscopy (TEM), it is revealed that the grains of SnSe nanoplates contain a high density of dislocations ($\sim 2 \times 10^{11} \text{ cm}^{-2}$) that has not been observed in previous SnSe nanomaterials and pristine SnSe. It is also observed that during the growth of SnSe nanoplates, imperfect oriented

attachment,^[31] which is proposed to explain the defect generation in nanocrystals, contributes to the dislocation formation in SnSe nanoplates

For thermoelectric characterization, SnSe nanoplates were consolidated into a dense pellet by spark-plasma sintering (SPS). The pellet shows relatively low thermal conductivity (κ_{tot}) but poor electrical conductivity (σ) due to low hole concentration ($\sim 1.5 \times 10^{14} \text{ cm}^{-3}$). It is hypothesized that the low hole concentration results from the surface impurities of SnSe nanoplates such as native organic ligands, iodide ligands, and unwanted surface oxides, which are revealed by thermogravimetric analysis (TGA) and X-ray photoelectron spectroscopy (XPS). In order to remove these impurities, the nanoplates were treated with ammonia solution. Ammonia is an inorganic molecular ligand that is produced worldwide and can be easily removed during sintering due to its low boiling point. We will refer to the SnSe nanoplates treated with ammonia solution as NH_3 -SnSe nanoplates. TGA and XPS data show that after ammonia treatment, the surface impurities mentioned above are effectively removed. Inductively coupled plasma atomic emission spectroscopy (ICP-AES) and Raman

spectroscopy reveal that the loss of Sn occurs along with the elimination of iodide ligands and surface oxides. Subsequent consolidation of NH₃-SnSe nanoplates produces the dense pellets. As a result of the removal of surface impurities, carrier concentration of the resultant pellet dramatically increases up to $\sim 2.1 \times 10^{17} \text{ cm}^{-3}$ without significant damage to mobility, thereby enhancing the electrical conductivity. In addition, TEM studies show that our unique nanoplates produce a high density of dislocations ($\sim 3 \times 10^{11} \text{ cm}^{-2}$) and mesoscale grains in the sintered NH₃-SnSe. These structural elements result in ultralow lattice thermal conductivity ($\sim 0.23 \text{ W m}^{-1} \text{ K}^{-1}$) comparable to that of a SnSe single crystal and a high thermoelectric figure of merit ($ZT = (S^2\sigma/\kappa_{tot})T$, where S is the Seebeck coefficient and T is the absolute temperature) of ~ 1.1 is achieved at 873 K.

3.2 Experimental Section

3.2.1 Starting Materials

Tin chunk (99.999%, American Elements, US), tin(II) oxide (99.9%, Alfa Aesar), tin (IV) oxide (99.9%, Sigma-Aldrich), iodine (99.99%, Alfa Aesar), selenium (99.99%, Sigma-Aldrich), calcium hydride (95%, Alfa Aesar), oleylamine (70%, Sigma-Aldrich), trioctylphosphine (97%, Sigma-Aldrich), 7 N ammonia in methanol (Sigma-Aldrich), toluene (99.8%, anhydrous, Sigma-Aldrich), acetonitrile (99.8%, anhydrous, Sigma-Aldrich), methanol (99.8%, anhydrous, Sigma-Aldrich). Hydrochloric acid (35–37%, Samchun Chemical). All chemicals were used without any further purification, except for oleylamine, which was degassed at 100 °C for 3 h under vacuum followed by drying with calcium hydride for 5 days.

3.2.2 Preparation of Tin Iodide

Tin iodide was prepared following a modified procedure.^[32] Briefly, 25 g of tin and 150 mL of 2 M hydrochloric acid was loaded in a 3-necked 250 mL bottom-round flask under Ar flow followed by addition of 35 g of iodine. The mixture was refluxed. When iodine vapor disappeared, 25 mL of 2 M hydrochloric acid was added. A small amount

of tin chunk was added until a yellow solution was obtained and unreacted tin chunk became lustrous. The unreacted tin chunk was separated from yellow solution by decanting the solution to another 250 mL 3-necked flask under Ar flow. The solution left to cool overnight. Shiny, needle-shaped, red crystals were separated by suction filtration in the vacuum under Ar flow followed by drying in the vacuum at 50 °C overnight. The dry crystals were transferred in fused silica tube (300 mm length and 18 mm OD). The tube was placed in a heating jacket and heated to 350 °C under vacuum. After cooling, the tube was transferred and stored in an Ar-filled glovebox and tin iodide was used after grinding.

3.2.3 Synthesis of SnSe Nanoplates and NH₃-SnSe Nanoplates

All the syntheses were carried out under inert atmosphere using standard Schlenk line technique and glove box. 6.706 g of tin iodide and 1.421 g of selenium were added in 180 mL of dry oleylamine. The solution was heated up to 150 °C, followed by aging for 5 h. After cooling the solution, the product was separated and washed several times using centrifugation at 9000 rpm. The product was dried overnight under vacuum. For the synthesis of NH₃-SnSe nanoplates, the as-prepared

SnSe nanoplates were reacted with 7 N ammonia in methanol under stirring for 12 h. Finally, the product was washed with methanol and dried under vacuum.

3.2.4 Spark Plasma Sintering

The SnSe nanopowders were annealed at 350 °C under 5% H₂/95% Ar flow for 1 h to remove residues. The annealed powders were ground and loaded into a graphite die in the glove box. The graphite die was taken out of the glovebox and placed in a spark plasma system (SPS-211Lx, Fuji Electronic Industrial Co., Japan). The sample chamber was evacuated to a vacuum of $\sim 2.0 \times 10^{-2}$ torr, and the samples in graphite die were sintered at 783 K for 10 min under an axial pressure of 50 MPa under vacuum.

3.2.5 Characterizations

Transmission electron microscopy (TEM) and high-resolution TEM (HRTEM) images were obtained using a JEM-2100F (JEOL) operating at 200 kV. Scanning TEM (STEM) and energy dispersive X-ray spectroscopy (EDS) analysis were performed using a Tecnai F20 (FEI) equipped with an EDAX Tecnai 136-5 detector. The cross-sectional sample was prepared by focused ion beam (FIB, Helios 650, FEG, FEI)

with a dual beam microscope using gallium ion milling. Atomic resolution images and elemental mappings were obtained using a spherical aberration-corrected JEM ARM-200F microscope (Cold FEG Type, JEOL) equipped with a SDD type EDS detector at 200 kV. The field emission scanning electron microscopy (SEM) images were collected using MERLIN Compact (Zeiss). XRD patterns were obtained using a D/Max-3C diffractometer (Rigaku) equipped with a rotating anode and a Cu K α radiation source ($\lambda = 0.15418$ nm). The XPS spectra were recorded using a K-Alpha XPS System (Thermo Fisher Scientific) equipped with an Al K α (1486.6 eV) X-ray source. All spectra were corrected using the binding energy of adventitious carbon 1s at 284.6 eV. Thermogravimetric analysis (TGA) were conducted on a SDT Q600 apparatus (TA instrument) under Ar flow heating up to 900 K at a heating rate of 10 K min⁻¹. Differential scanning calorimeter (DSC) data were taken on a DSC 214 Polyma instrument (Netzsch) in an aluminum crucible with a lid under Ar flow heating up to 823 °C at a heating rate of 10 K min⁻¹ and cooling to room temperature at the same rate. The elemental compositions were characterized by inductively coupled plasma-atomic emission spectrometry (ICP-AES, OPTIMA 8300, Perkin-Elmer). The powders were dissolved in aqua regia and diluted

with deionized water. Elemental analyses (C, H, and N) were performed on a Flash2000 (Thermo Fisher Scientific). Fourier transform infrared spectroscopy (FTIR) analysis were conducted on a Vertex 70 FT-IR spectrometer (Bruker) equipped with a DLATGS detector and a KBr substrate with a multilayer coating beam splitter. The Raman spectrum was collected using a LabRam Aramis (Horiba Jobin Yvon) system equipped with a 785 nm diode laser.

3.2.6 Electrical and Thermal Transport Property Measurements

The pellets produced after SPS process were cut and polished into various shapes and dimensions (Fig. 3.11). The electrical conductivity and Seebeck coefficient were simultaneously measured for bar-shaped samples with dimensions of $\sim 13 \text{ mm} \times 8 \text{ mm} \times 1 \text{ mm}$ under an Ar atmosphere in the temperature range of $\sim 300 \text{ K}$ to $\sim 873 \text{ K}$ using a Netzsch SBA 458 Nemesis system. Hall effect measurements were conducted using a Lake Shore HMS8407 Hall effect measurement system under a magnetic field of 1.5 T. Thermal diffusivities were taken for disk-shaped samples with a diameter of 6 mm and a thickness of 1 mm using a laser flash diffusivity method on a Netzsch LFA 457

instrument. The surface of samples were coated with graphite. The total thermal conductivity was obtained by the equation $\kappa_{tot} = \rho \cdot D \cdot C_p$, where ρ is the mass density, D is the thermal diffusivity, and C_p is the specific heat capacity. The mass density was calculated from the geometrical dimensions and mass of the sample and C_p was obtained from the previous report.^[33] The total thermal conductivity is the sum of electronic thermal (κ_{elec}) and lattice (κ_{latt}) conductivity. κ_{elec} is obtained using the Wiedemann–Franz law, $\kappa_{elec} = L \cdot \sigma \cdot T$, where L is the temperature-dependent Lorenz number and T is the absolute temperature.

3.3 Results and Discussion

In a typical synthesis of SnSe nanoplates, the reaction mixture loaded with SnI₂, Se, and oleylamine was heated at 150 °C for 5 h. Selenium powders were used as Se precursors to replace organophosphine selenide and SeO₂, which have been used for the synthesis of SnSe nanocrystals in previous reports.^[26,28,34] Synthesis for the SnSe nanocrystals usually proceeds at high temperature of 250 °C, whereas the high reactivity of the selenium powders enables the decrease of reaction temperature to 150 °C. Oleylamine was treated with CaH₂ prior to use in the reaction because oxygen-containing impurities present in the as-received oleylamine can easily oxidize Sn(II) to Sn(IV).^[35] Otherwise, the formation of SnSe₂ is intermittently observed in XRD (Fig. 3.1c and d). Due to a facile heat-up method, the synthesis of SnSe nanoplates allows high yield (>90%) and scalability with the production of ~3.4 g per batch (Fig. 3.1b). TEM images show that SnSe nanoplates are composed of small-plate structures, exhibiting a nearly rectangular morphology and a side length of 100–150 nm with a thickness of ~25 nm (Fig. 3.1a). Powder XRD pattern of SnSe nanoplates is clearly indexed to orthorhombic SnSe structure,

with no noticeable impurities such as SnSe₂ (Fig. 3.1c). The intensity ratio of (400) peak to (011) peak for SnSe nanoplates, which corresponds to the *a*-axis and the *bc*-plane, respectively, is smaller than that for standard reference, displaying their anisotropic nature. Chemical composition of SnSe nanoplates determined by ICP-AES agrees well with the nominal composition of SnSe.

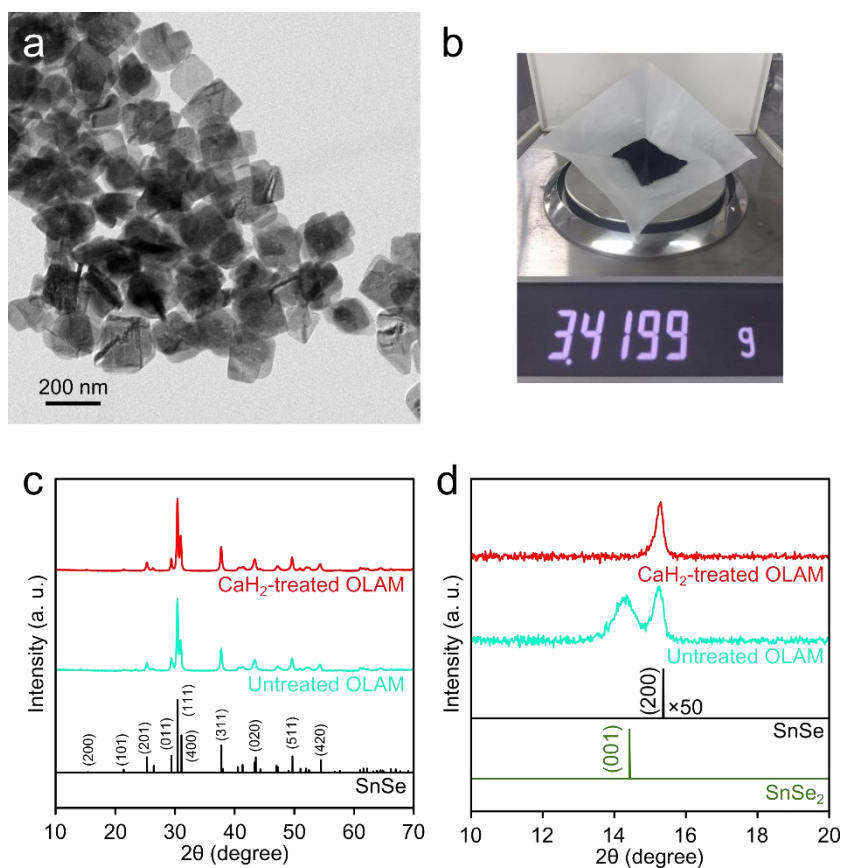


Figure 3.1 (a) TEM image of as-synthesized SnSe nanoplates. (b) Photograph showing a production scale for nanopowders of ~3.4 g per batch. (c) Powder XRD patterns of SnSe nanoplates synthesized by using CaH₂-treated oleylamine (OLAM) and untreated OLAM. (d) Magnified XRD pattern of 2θ between 10° and 20° in (c). Standard reference XRD peaks of SnSe and SnSe₂ are represented in black line (JCPDS 48-1224) and green line (JCPDS 23-0602), respectively.

For the structural analysis, we performed high-resolution TEM (HRTEM) studies on the SnSe nanoplates (Fig. 3.2). HRTEM image of SnSe nanoplates shows polycrystalline nature (Fig. 3.2b). While fast-Fourier transform (FFT) patterns taken from Area I and Area I' are same, the FFT patterns obtained from Area I and Area II, show different orientations (Fig. 3.2c). It is regarded that Area I and Area I' share the same grain, but the grain of Area II is misoriented with that of Area I with a high-angle of $\sim 87^\circ$. Interestingly, the array of dislocations is observed at the interface between Area I and Area II (Fig. 3.2d and e). Moreover, the lattices of the Area I' and Area II have a mirror-image relationship. To understand the atomic arrangement near the interfaces between three regions, the atomic positions of Sn and Se are schematically illustrated in Fig. 3.2f. Assuming that Area I' and Area II have a twinning relationship with a $\{011\}$ twin boundary, the angle between (002) planes from Area I and Area II is calculated to be 86.01° , which is comparable to the observed value. Furthermore, twinning induces an open gap between the Area I and Area II, marked by a white circle in Fig. 3.2f. Therefore, we suggest that twinning can provide a way to introduce the dislocations to fill the

gap. In addition to the dislocations in the grain boundary, we observed the dislocations that are located in the grain of SnSe nanoplates (Fig. 3.3). The average dislocation density inside the grains is estimated to be $\sim 2 \times 10^{11} \text{ cm}^{-2}$ from collected images, which is much higher than that typically measured in semiconductors ($10^3\text{--}10^6 \text{ cm}^{-2}$).^[3]

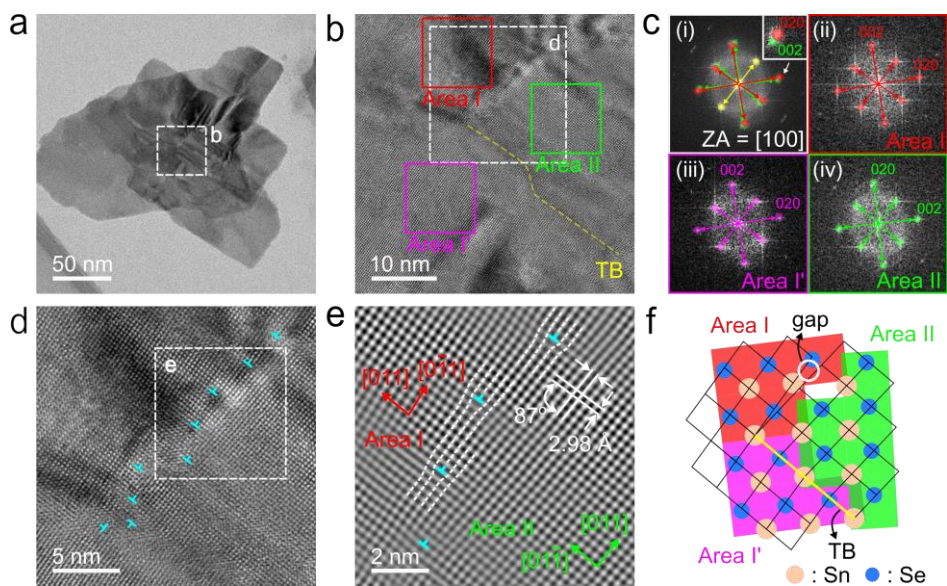


Figure 3.2 (a) Medium-magnification TEM image of SnSe nanoplates. (b) High-magnification TEM image in the box marked in (a). A yellow dashed line roughly shows a twin boundary (TB). (c) FFT patterns in (i) whole area, (ii) Area I, (iii) Area I', and (iv) Area II in (b). The inset of (i) shows the magnified patterns marked by arrow. (d) High-magnification TEM image in the box of (b). The dislocations are shown by a T-shaped symbol. (e) Inverse FFT image of the white box in (d) clearly showing a dislocation-introduced region. White dashed lines are overlaid on the $\{011\}$ planes as guides. (f) Schematic illustration of the twinned structure in (b). The edges of rhombus are $\{011\}$ planes and a yellow line shows the twin boundary.

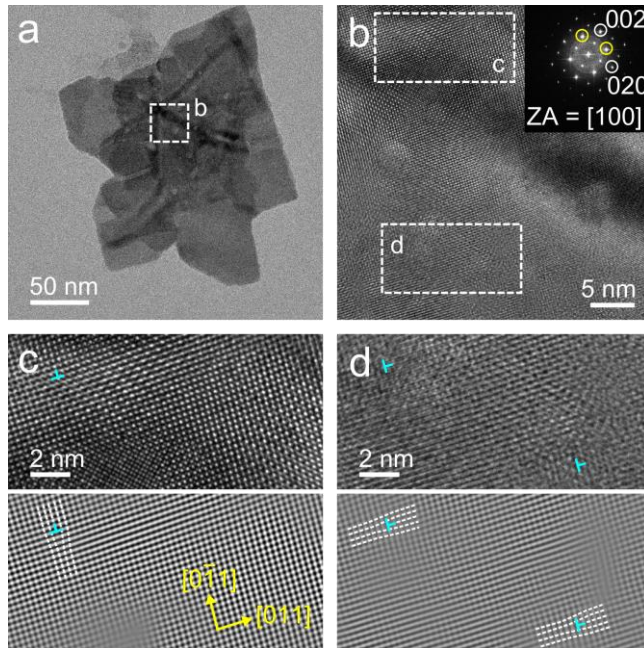


Figure 3.3 (a) Medium-magnification TEM image of SnSe nanoplates. (b) High-magnification TEM image in the box of (a). The inset shows a corresponding FFT pattern along the [100] axis. (c, d) Enlarged high-magnification TEM image (upper) from the box and corresponding inverse FFT image (bottom) in (b). The dislocations are shown by a T-shaped symbol. White dashed lines are overlaid on the (011) planes as guides.

In an effort to understand the formation mechanism of the dislocations, we investigated TEM images of aliquots taken at different aging times (Fig. 3.4). The nanoplates of 10–40 nm in size and amorphous nanoparticles of 2–5 nm in diameter produced in the early growth stage are gradually crystallized and fused to grow into the assembled SnSe nanoplates. This growth process is analogous to the oriented attachment growth observed in the formation of PbS and SnSe nanosheets.^[34,36] Because the two colliding nanoparticles are very unlikely to be perfectly aligned, defects such as dislocations and twin boundaries often occur at the interface of the attached nanoparticles.^[31,37] We similarly observed the dislocations at the interface of the attached nanoplates in the early stage that are misaligned (Fig. 3.5). Twinning is identified in the attached nanoplates, and the misorientation angle between the (002) planes of each nanoplate is found to be $\sim 87^\circ$, which is consistent with the observation in the as-synthesized SnSe nanoplates. Previous reports showed that misaligned nanoparticles become typically single-crystalline by structural rearrangements that remove defects during merging process.^[38,39] However, in our synthetic conditions, the dislocations are not eliminated from the

SnSe nanoplates because twin boundaries usually hinder the dislocation motion, and the low reaction temperature may not provide sufficient driving force to diffuse out the dislocations.^[40,41] As a result, the dislocations and the misaligned regions are present in the SnSe nanoplates as observed during the nanoplates growth. Furthermore, the dislocations inside the grain seem to be produced in a similar way. In the aspect of thermoelectric performance, dense dislocations act as an effective scattering point for phonons, reducing thermal conductivity.^[10,42]

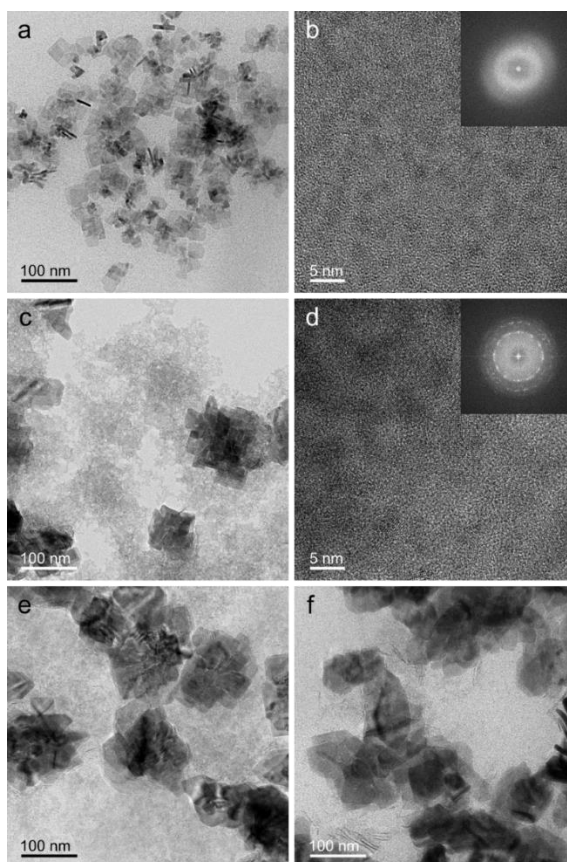


Figure 3.4 Time-dependent growth of SnSe nanoplates. TEM images of the aliquots sampled from the reaction batch at (a, b) 0 min, (c, d) 10 min, (e) 30 min, and (f) 2 h at 150 °C. The insets in (b) and (d) show corresponding FFT patterns, indicating amorphous and crystalline nanoparticles, respectively. The nanoplates with the size of 10–40 nm and nanoparticles with the diameter of 2–5 nm formed in the early growth stage are continuously fused to grow into the SnSe nanoplates.

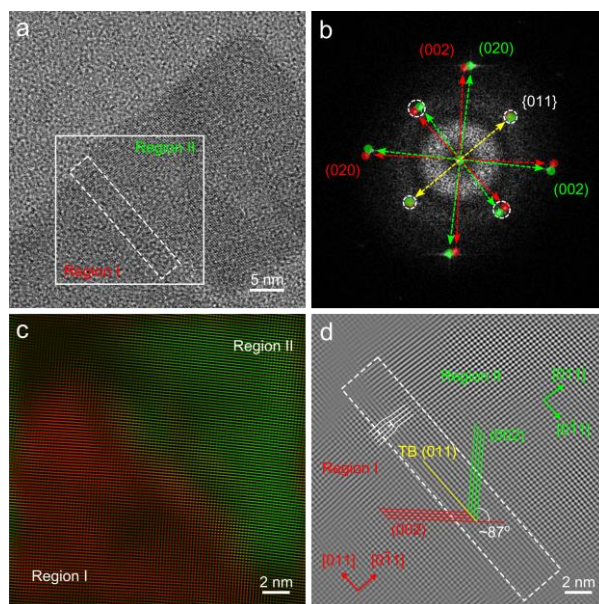


Figure 3.5 (a) HRTEM of attached SnSe nanoplates observed in the early stage of growth. White dashed box shows the interface of the attached nanoplates. (b) FFT pattern of the white solid box in (a). Colored circles with arrows show different SnSe grains (Red: Region I, green: Region II). (c) Inverse FFT image of an white solid box by applying masks on (020) and (002) spots from each region. (d) Inverse FFT image of the selected area of an white solid box by applying masks on {011} spots. The dislocations are shown by a T-shaped symbol. White lines are overlaid on the {011} planes as guides. Red and green lines show the (002) planes in Region I and Region II, respectively. Twin boundary (TB) is shown by a yellow line.

Nanocrystals synthesized *via* colloidal methods typically are stabilized by bulky organic ligands, which bind on the surface. Fourier transform infrared (FTIR) spectroscopy was performed to identify the organic ligands on SnSe nanoplates (Fig. 3.6a). In the spectra of SnSe nanoplates, the absorptions at 2800–3000 cm^{-1} and 1463 cm^{-1} are ascribed to the stretching and deformation vibration of C–H bonds, respectively. The broad band at 3434 cm^{-1} and absorptions at 1630 cm^{-1} are assigned to the stretching and deformation vibration of N–H bonds. The broadening of N–H absorption for SnSe nanoplates compared to that for free oleylamine describes that SnSe nanoplates are capped with oleylamine. Because organic ligands inhibit charge carrier transport, oleylamine needs to be replaced with shorter ligands or removed from the surface of nanocrystals. To remove oleylamine, we treated SnSe nanoplates with methanolic ammonia solution. Hydrazine is typically used to displace the organic ligands from nanocrystals, but its strong reductive power makes SnSe completely decomposed.^[43] Owing to nonreductive property of ammonia solution, on the other hand, it has been successfully employed to strip the native ligands of nanocrystals, such as $\text{Sb}_{(2-x)}\text{Bi}_x\text{Te}_3$ nanoplatelets and PbTe

nanocrystals.^[17,44] With the modification of the previous procedure, SnSe nanoplates were stirred in 7 N methanolic ammonia solution overnight under Ar atmosphere. After the reaction, the nanopowders were washed with methanol and dried overnight. The intensity of C–H stretching vibration for the resultant powders in FTIR spectrum decreases in comparison to that for as-prepared nanoplates (Fig. 3.6a). TGA quantitatively supports that ~60% of organic ligands are removed after ammonia treatment, consistent with the results obtained from elemental analysis (Fig. 3.6b and 3.7a). The elemental analysis data show that carbon and hydrogen contents decrease, whereas nitrogen content is almost maintained after ammonia treatment, meaning that oleylamine is detached from the surface of nanoplates. Because ammonia and methanol are neutral molecules in ammonia solution, exposure of SnSe nanoplates to excess ammonia and methanol can drive the exchange of oleylamine on the surface with electrical neutrality satisfied.^[12]

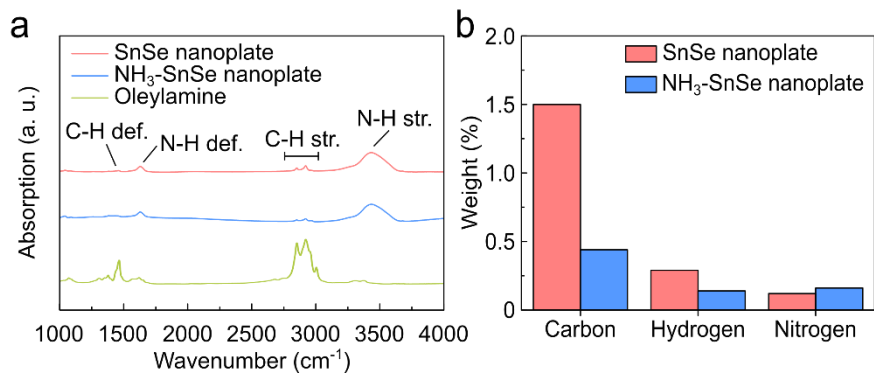


Figure 3.6 (a) Fourier transform infrared spectroscopy (FTIR) spectra of oleylamine, as-synthesized SnSe nanoplates, and NH₃-SnSe nanoplates. (b) Elemental analysis of SnSe nanoplates and NH₃-SnSe nanoplates.

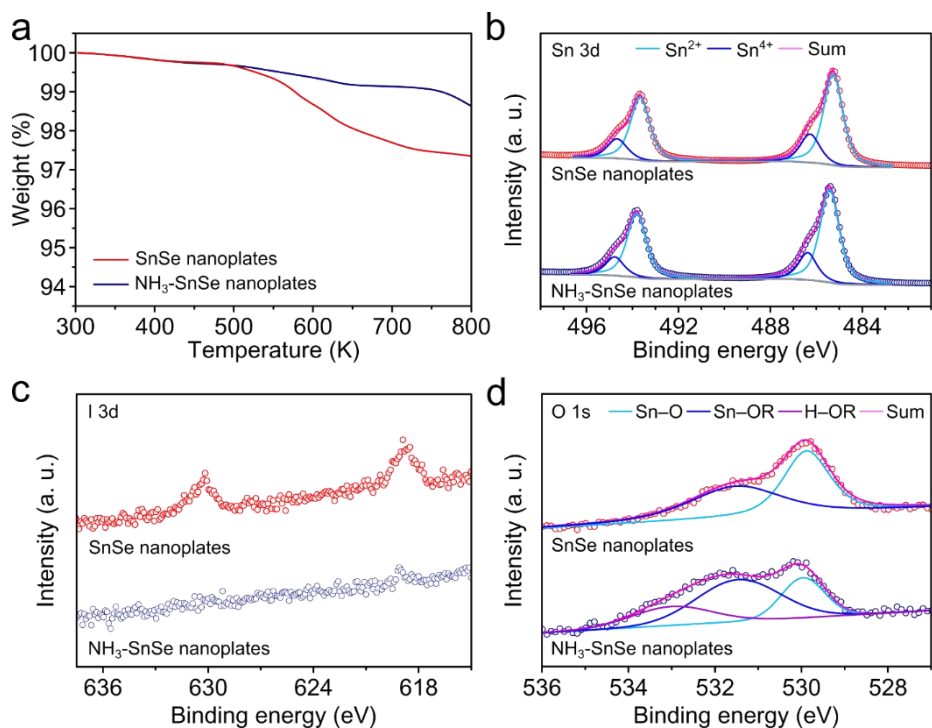


Figure 3.7 (a) Thermogravimetric analysis (TGA) of SnSe nanoplates and NH₃-SnSe nanoplates under Ar flow at a rate of 10 K min⁻¹ up to 800 K. (b–e) X-ray photoelectron spectra (XPS) of SnSe nanoplates and NH₃-SnSe nanoplates. The spectra of (b) Sn 3d, (c) I 3d, and (d) O 1s binding energy regions for SnSe nanoplates (upper) and NH₃-SnSe nanoplates (bottom). R refers to alkyl group and hydrogen in (d). The intensity of XPS spectra is normalized to the peak area of Sn 3d.

To figure out the chemical states on the surface, we performed high resolution XPS analysis and compared the spectra of SnSe nanoplates and NH₃-SnSe nanoplates. We deconvoluted the spectrum of Sn 3d core level for SnSe nanoplates into two profiles, indicating that there are two different oxidation states of Sn corresponding to Sn²⁺ (3d_{5/2} at 485.3 eV) and Sn⁴⁺ (3d_{5/2} at 486.2 eV) (Fig. 3.7b).^[45] The ratio of Sn²⁺ to Sn⁴⁺ remains almost identical as ~80% before and after ammonia treatment. The proportion is consistent with that of tin chalcogenide nanocrystals previously established by ¹¹⁹Sn-Mössbauer spectroscopy.^[46] The spectrum for SnSe nanoplates in Fig. 3.7c shows the peak at 618.8 eV corresponding to I 3d_{5/2} core level because iodide ligands derived from Sn precursor, SnI₂, are left on the surface after the synthesis of SnSe nanoplates. After ammonia treatment, the peak intensity significantly decreases, meaning that iodide ligands are detached from the surface by ligand exchange reaction. Considering the charge neutrality during the ligand exchange process, iodide ligands can be removed as a neutral metal-ligand complex.^[12] To support the principle, we separated and analyzed supernatant from NH₃-SnSe nanoplates by centrifugation after

ammonia treatment. The vibration of Sn–I from supernatant is observed in a Raman spectrum and both Sn and I are detected in XPS (Fig. S8a–c). Because iodine can act as an n-type dopant, removal of iodide ligands is necessary for SnSe to be a p-type semiconductor.^[47] The evidence for the decrease of undesired oxide species during ammonia treatment is found in the O 1s core level spectra (Fig. 3.7d). The O 1s spectrum for SnSe nanoplates is fitted with two profiles, which correspond to Sn–O (529.9 eV) and Sn–OH (531.5 eV), respectively.^[48] Both peaks are likely to arise from a trace of inevitable moisture during synthesis and purification, though all process was conducted under inert atmosphere. The O 1s spectrum for NH₃-SnSe nanoplates is deconvoluted into three peaks, which are assigned to Sn–O (530.0 eV), Sn–OR (531.5 eV, R refers to methyl group and hydrogen), and H–OR (533.0 eV). The appearance of H–OR peak is ascribed to methanol which originates from ammonia solution. Interestingly, the peak area of Sn–O species decreases almost in half after ammonia treatment, suggesting that SnO_x is partially dissolved during the surface treatment (Table 3.1). Because both Sn²⁺ and Sn⁴⁺ have amphoteric properties, SnO_x can be dissolved in basic ammonia solution. To

support the observation on the decrease of Sn–O species, we investigated the solubility of 1 mmol of SnO, SnO₂, and SnSe nanoplates in 4 mL methanolic ammonia solution. Sn concentration in supernatant was measured by ICP-AES. According to the result, dissolution of SnO, SnO₂, and SnSe nanoplates is identified, and its Sn concentration from each supernatant is 2.6, 0.74, and 3.8 μmol/mL, respectively (Fig. 3.8d). The high Sn concentration of SnSe nanoplates can be explained by both the dissolution of SnO_x and the loss of Sn during the removal of iodide ligands. The elemental composition of NH₃-SnSe nanoplates determined from ICP-AES shows the decrease in the ratio of Sn to Se, which agrees with the Sn concentration of SnSe nanoplates in ammonia solution (Table 3.2).

Table 3.1 Fitting results of O1s XPS spectra of SnSe and NH₃-SnSe nanoplates in Fig. 3.7d

Samples	Component	Peak (eV)	Area (%)	O/Sn atomic ratio
SnSe nanoplates	Sn-O	529.9	50	0.24
	Sn-OR	531.5	50	
NH ₃ -SnSe nanoplates	Sn-O	530.0	26	0.27
	Sn-OR	531.5	52	
	H-OR	533.0	22	

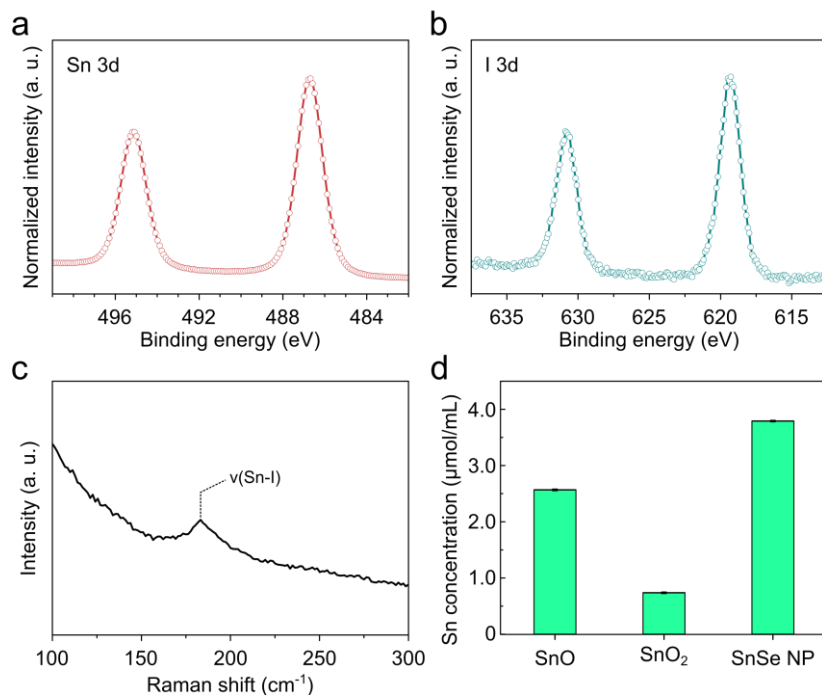


Figure 3.8. XPS spectra of (a) Sn 3d and (b) I 3d binding energy regions for the supernatant dried on SiO₂/Si wafer. (c) Raman spectrum for the supernatant. The Raman signal was amplified by surface-enhanced Raman scattering (SERS).^[49] Supernatant was dried on the substrate coated with gold nanoparticles. (d) Sn concentration in supernatant obtained from the ammonia treatment of SnO, SnO₂, and SnSe nanoplates (SnSe NP). Each powder (1 mmol) was stirred in the 4 mL of methanolic NH₃ solution for 12 h under Ar atmosphere, and the supernatant was separated by precipitating the powders using centrifugation.

Table 3.2 Chemical composition of SnSe nanoplates, NH₃-SnSe nanoplates, SPSed SnSe, and SPSed NH₃-SnSe analyzed by inductively coupled plasma atomic emission spectroscopy (ICP-AES).

Samples	ICP-AES
SnSe nanoplates	Sn _{0.99(1)} Se _{1.00}
NH ₃ -SnSe nanoplates	Sn _{0.98(2)} Se _{1.00}
SPSed SnSe	Sn _{1.023(1)} Se _{1.00}
SPSed NH ₃ -SnSe	Sn _{1.03(1)} Se _{1.00}

TEM images and elemental mapping images *via* energy dispersive X-ray spectroscopy (EDS) show that $\text{NH}_3\text{-SnSe}$ nanoplates retain their size and shape in ammonia solution, and homogeneous elemental distribution of Sn and Se is kept similarly, indicating that ammonia solution is not as destructive to SnSe as hydrazine (Fig. 3.9). The crystallinity of $\text{NH}_3\text{-SnSe}$ is preserved during ammonia treatment (Fig. 3.10). On the basis of the above results, we find out that the treatment with ammonia solution serves to remove not only organic ligands but also iodide ligands and tin oxides from the surface of SnSe nanoplates.

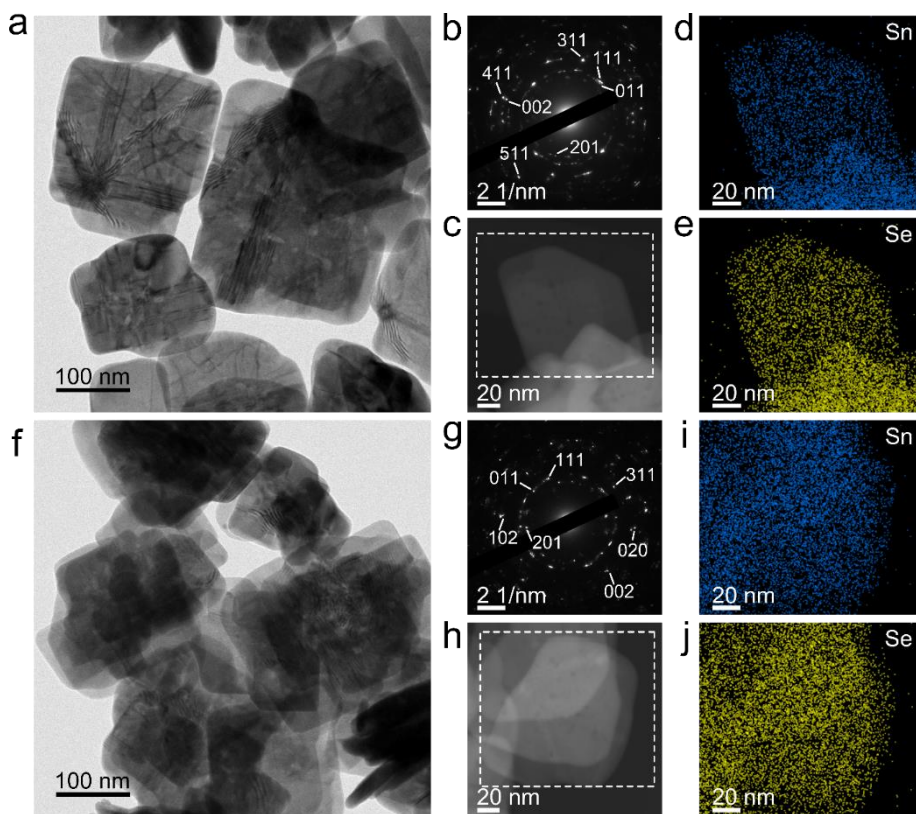


Figure 3.9 (a, f) TEM images, (b, g) selected area electron diffraction (SAED) patterns, and (c–e, h–j) scanning TEM (STEM) images with corresponding elemental mappings for (a–e) SnSe nanoplates and (f–j) NH_3 -SnSe nanoplates. There is no noticeable change in size, morphology, and crystallinity of SnSe nanoplates before and after ammonia treatment. Uniform distribution of Sn (blue) and Se (yellow) is retained after surface treatment.

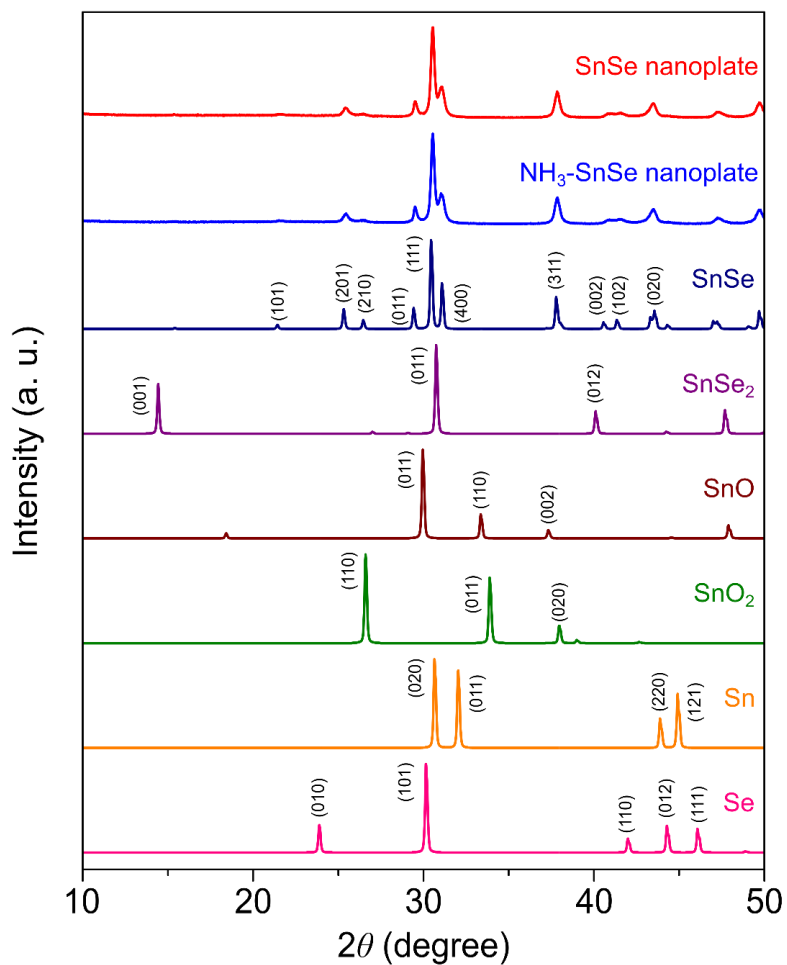


Figure 3.10 Powder XRD patterns of as-synthesized SnSe nanoplates and $\text{NH}_3\text{-SnSe}$ nanoplates along with those of the standard references (SnSe, SnSe_2 , SnO, SnO_2 , Sn, and Se). Difference in the XRD pattern between SnSe nanoplates and $\text{NH}_3\text{-SnSe}$ nanoplates cannot be found.

To verify our strategy of enhancing thermoelectric properties of SnSe nanoplates by defect and surface engineering, we firstly produced bulk SnSe by sintering the nanopowders *via* SPS. SnSe nanoplates and NH₃-SnSe nanoplates powders were consolidated into a dense pellet (5.87 and 6.06 g/cm³, respectively), and each sample is named as SPSed SnSe and SPSed NH₃-SnSe (Fig. 3.11). Scanning electron microscopy (SEM) images of SPSed SnSe and SPSed NH₃-SnSe show dense and flat surface with a few scratches which were produced during polishing process (Fig. 3.12a and b). Uniform distribution of elements, Sn and Se, of both samples in microscale is identified in SEM-EDS elemental mapping. The powder XRD patterns of SPSed samples match well with the standard reference (Fig. 3.13). According to the IR spectrum, we cannot find any fingerprints of organic species in the samples after SPS, which could be harmful for solution-processed nanomaterials during thermoelectric operation (Fig. 3.14).

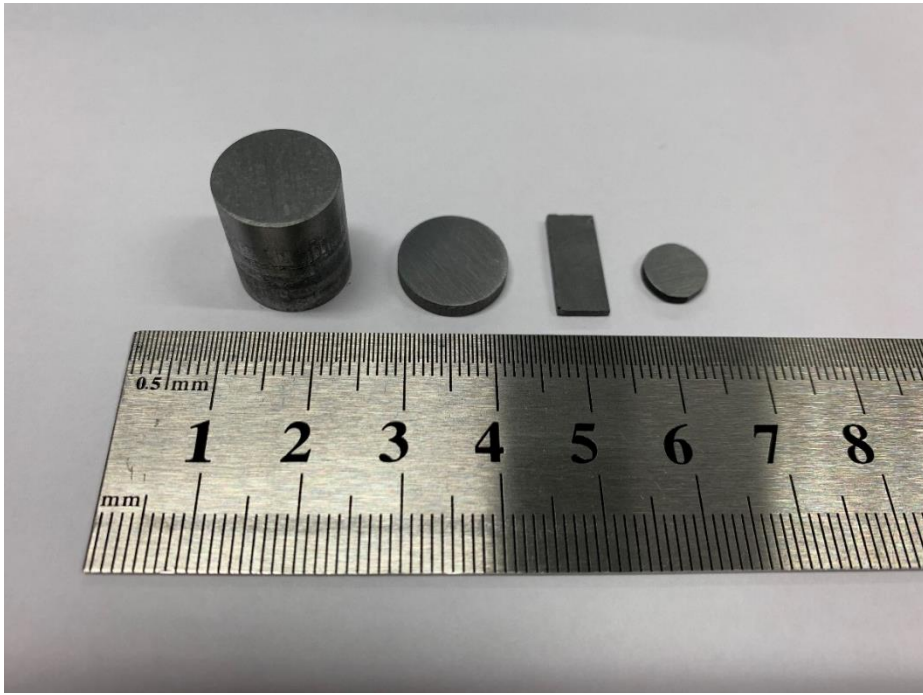


Figure 3.11 A photograph of dense pellet of sintered $\text{NH}_3\text{-SnSe}$ by spark plasma sintering (SPS) with a typical diameter of 13 mm and a thickness of ~13 to 14 mm and specimens cut for measuring electrical and thermal transport properties.

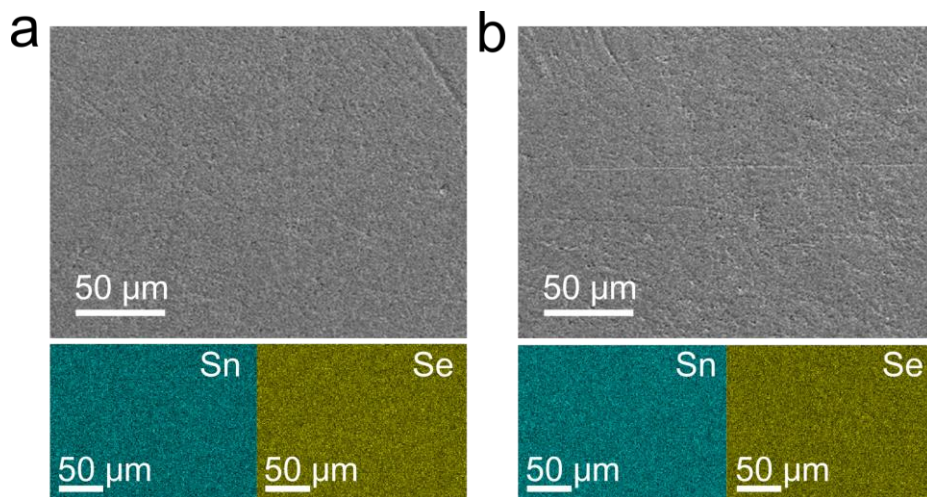


Figure 3.12 Scanning electron microscopy (SEM) images of (a) SPSed SnSe and (b) SPSed NH₃-SnSe and elemental mappings of Sn (bottom left, blue) and Se (bottom right, yellow) at the whole area in the SEM image, examined by energy dispersive X-ray spectroscopy (EDS).

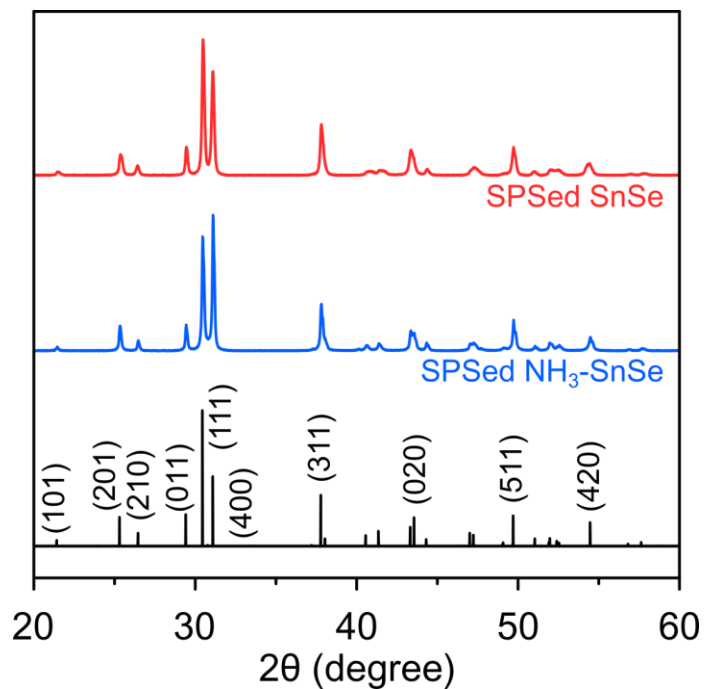


Figure 3.13 Powder XRD patterns of SPSed SnSe (red) and SPSed NH₃-SnSe (blue). Standard reference XRD peaks of SnSe are displayed in black line (JCPDS 48-1224).

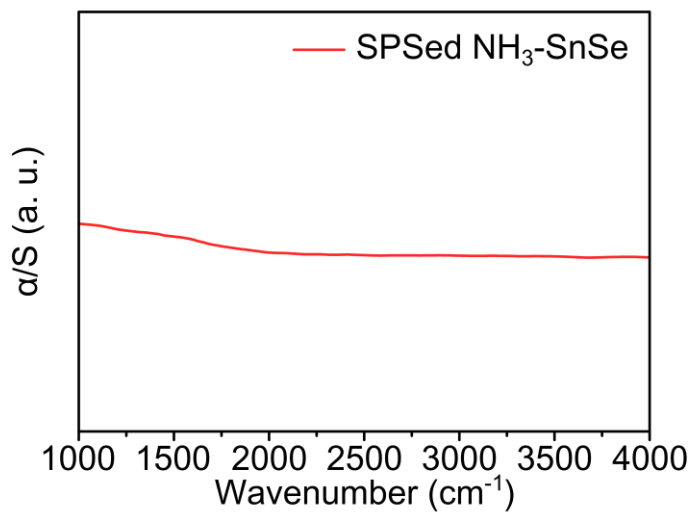


Figure 3.14 FTIR spectrum of SPSed NH₃-SnSe.

The cross-sectional scanning TEM (STEM) image of the SPSed $\text{NH}_3\text{-SnSe}$ viewed along the $[001]$ axis shows typical SnSe structure (Fig. 3.15). Elemental mapping by STEM-EDS verifies the locations of Sn and Se atoms. The TEM image in Fig. 3.16a reveals that SPSed $\text{NH}_3\text{-SnSe}$ consists of mesoscale grains and the average size is ~ 370 nm. In addition, we found that dislocations are present in SnSe by performing HRTEM analysis. The HRTEM image viewed along $[01\bar{1}]$ is shown in Fig. 3.16b, and the corresponding FFT image is indexed as the orthorhombic structure. The inverse FFT image of the (111) planes, taken from the dashed box area in Fig. 3.16b, clearly shows dense dislocations marked by the T-shaped symbols. Their average density, which is estimated from the images, is in the same order of magnitude ($\sim 3 \times 10^{11} \text{ cm}^{-2}$) as that in SnSe nanoplates. It is higher than that observed in normal semiconductor including SnSe crystal.^[50] In addition to the dislocations introduced in the SnSe nanoplates, Sn vacancies produced during ammonia treatment seem to create dislocations.^[42] The dislocations and mesoscale grains can significantly decrease lattice thermal conductivity through effective phonon scattering.^[51]

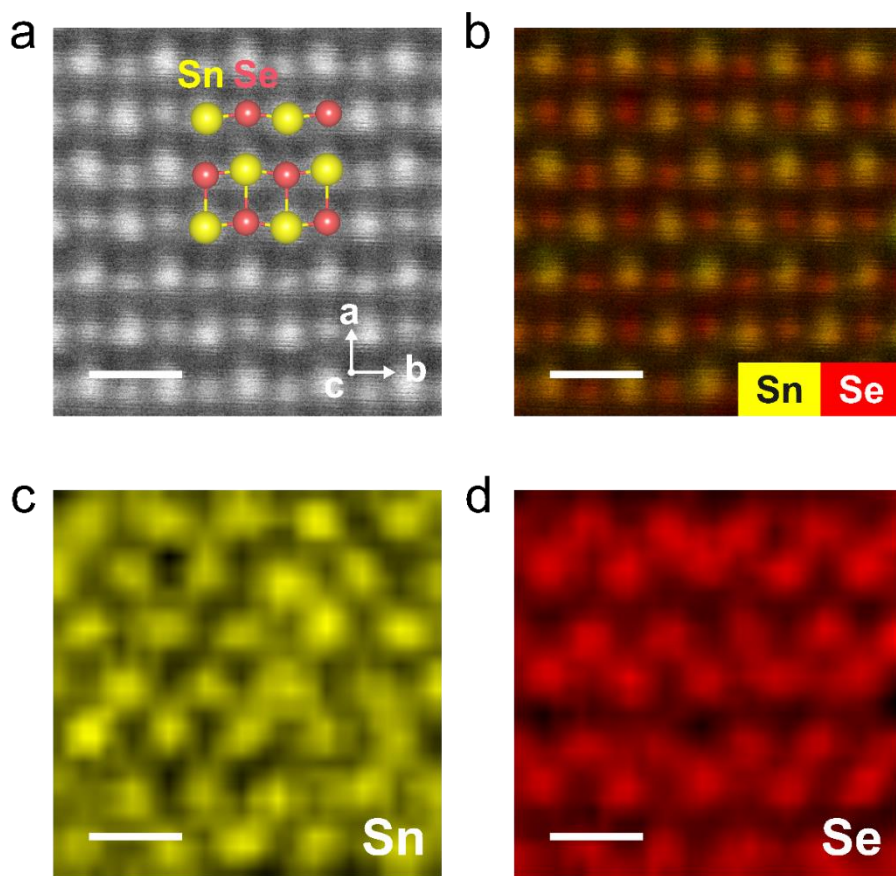


Figure 3.15 (a) A typical cross-sectional STEM image with crystal structure of SnSe and (b–d) elemental mappings of SPSed NH_3 -SnSe. The atomic-scale image is viewed along the [001] axis. Yellow and red spheres in (a) indicate Sn and Se atoms, respectively. Scale bar, 0.5 nm.

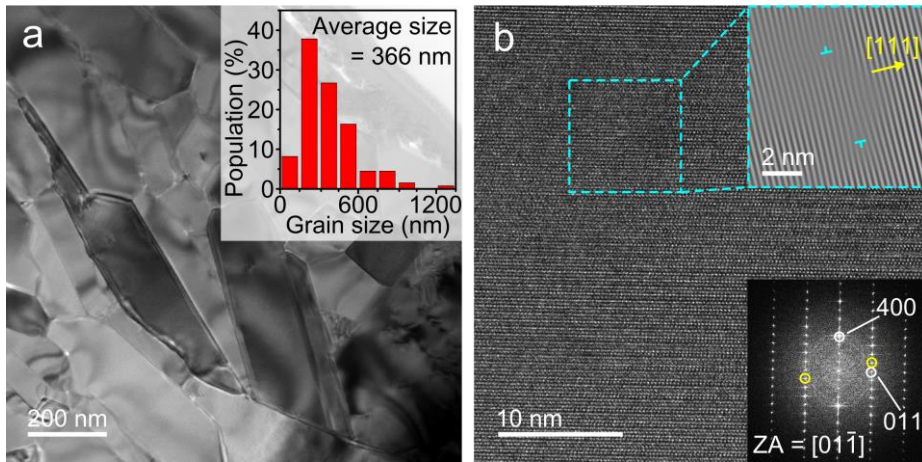


Figure 3.16 (a) Cross-sectional TEM image of SPSed $\text{NH}_3\text{-SnSe}$ showing mesoscale grains. The inset displays the size distribution of grains. (b) Typical cross-sectional HRTEM image of SPSed $\text{NH}_3\text{-SnSe}$. Corresponding FFT pattern is shown in the bottom inset. Inverse FFT images of the selected area is shown in the upper right inset. The dislocations are shown by a T-shaped symbol.

On account of two-dimensional structure of SnSe, XRD patterns of densified SnSe pellets show the preferred orientation of crystallites, which can result in highly anisotropic thermoelectric properties (Fig. 3.17a).^[52,53] Hence, we measured charge and thermal transport properties both parallel and perpendicular to the press direction. Because a ZT along the former direction is higher than that along the latter direction, we mainly discuss thermoelectric properties of the materials developed in this work parallel to the press direction. Their thermoelectric properties along the other direction are presented in Fig. 3.17b–f.

The temperature-dependent electrical conductivity (σ) of SPSed SnSe and SPSed NH₃-SnSe keeps almost constant up to ~673 K and rises afterward (Fig. 3.18a). The increase can be attributed to the structural phase transition from Pnma to Cmc₂m.^[54,55] For example, the σ of SPSed NH₃-SnSe increases from 0.08 S cm⁻¹ at room temperature to 49.4 S cm⁻¹ at 873 K. However, this enhancement for SPSed SnSe is much smaller than that of SPSed NH₃-SnSe, which results in ~5 times lower σ at 873 K. The Hall effect measurement reveals that the carrier concentration (n_H) is key in this enhancement. The n_H dramatically increases from $\sim 1.5 \times 10^{14}$

cm^{-3} for the SPSed SnSe to $\sim 2.1 \times 10^{17} \text{ cm}^{-3}$ for the SPSed NH_3 -SnSe, respectively, and the corresponding mobility (μ_{H}) slightly increases from ~ 2.0 to $\sim 2.2 \text{ cm}^2 \text{ V}^{-1} \text{ s}^{-1}$ (Fig. 3.19). The improvement of n_{H} arises from the contribution by the surface treatment. The ammonia treatment removes the residual iodide ligands that are left on the surface of SnSe nanoplates, which is confirmed by XPS results. It is also verified by XPS analysis that the iodine content in SPSed NH_3 -SnSe dramatically decreases compared with that in SPSed SnSe (Fig. 3.20). It was reported that iodine introduced into SnSe structure acts as an n-type dopant.^[47] Therefore, the elimination of iodide ligands by ammonia treatment can improve the hole concentration.

The temperature-dependent Seebeck coefficients (S) of SPSed samples display positive values in the whole temperature range, suggesting p-type conduction (Fig. 3.18b). It is shown that SPSed NH_3 -SnSe has a lower S value than SPSed SnSe because the S is inversely proportional to the n_{H} . The maximum power factor (PF) for SPSed NH_3 -SnSe is $3.81 \mu\text{W cm}^{-1} \text{ K}^{-2}$ at 873 K, which is comparable to that for polycrystalline SnSe prepared by high temperature solid-state reaction (Fig. 3.16c).^[56]

The total thermal conductivity (κ_{tot}) of SPSed samples gradually decreases with increasing temperature and slightly increases afterward because of bipolar conduction, which is consistent with the charge transport properties (Fig. 3.18d). Fig. 3.18e clearly indicates that the thermal transport is mainly dominated by heat-carrying phonons. We obtained the lattice thermal conductivity (κ_{latt}) of $\sim 0.23 \text{ W m}^{-1} \text{ K}^{-1}$ at 873 K for SPSed $\text{NH}_3\text{-SnSe}$, which is $\sim 50\%$ lower than that of polycrystalline SnSe. As described above, this can be explained by various structural elements observed in TEM images, such as mesoscale grains, dislocations, and atomic defects in the SPSed $\text{NH}_3\text{-SnSe}$. The dislocations and mesoscale grains can serve as effective phonon-scattering centers for short- and long-wavelength phonons, respectively.^[51,54] A thermoelectric figure of merit ZT value of SPSed $\text{NH}_3\text{-SnSe}$ increases with rising temperature and the highest ZT of ~ 1.1 at 873 K is obtained (Fig. 3.18f). The high thermoelectric performance is attributed to ultralow κ_{tot} with the PF comparable to that of polycrystalline SnSe.

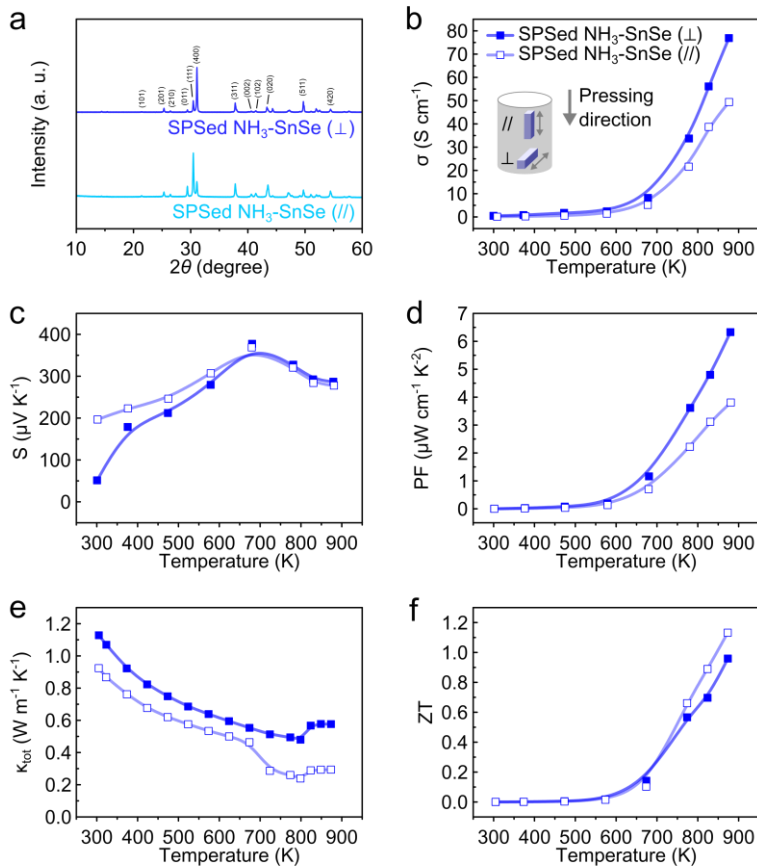


Figure 3.17 (a) XRD patterns of SPSed NH₃-SnSe pellets measured heading to the plane perpendicular (\perp) and parallel ($//$) to the press direction of SPS. The Lotgering factor (F_{h00}) is 0.274, showing that (400) planes are preferentially oriented along the press direction. (b) σ , (c) S , (d) PF , (e) κ_{tot} , and (f) ZT values of SPSed NH₃-SnSe measured along the plane perpendicular (\perp) and parallel ($//$) to the press direction of SPS.

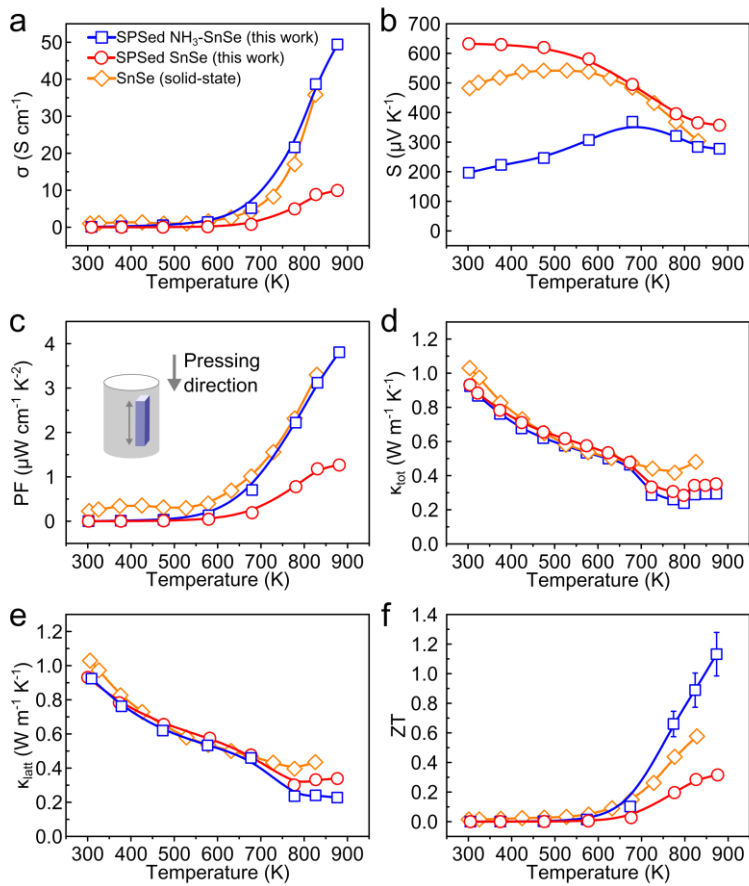


Figure 3.18 Temperature-dependent thermoelectric properties for SPSed SnSe and SPSed $\text{NH}_3\text{-SnSe}$. (a) Electrical conductivity (σ), (b) Seebeck coefficient (S), (c) power factor (PF), (d) thermal conductivity (κ_{tot}), (e) lattice thermal conductivity (κ_{latt}), and (f) ZT values. Thermoelectric properties of SPSed samples in this work are compared with those of SnSe synthesized via solid-state reaction.^[56]

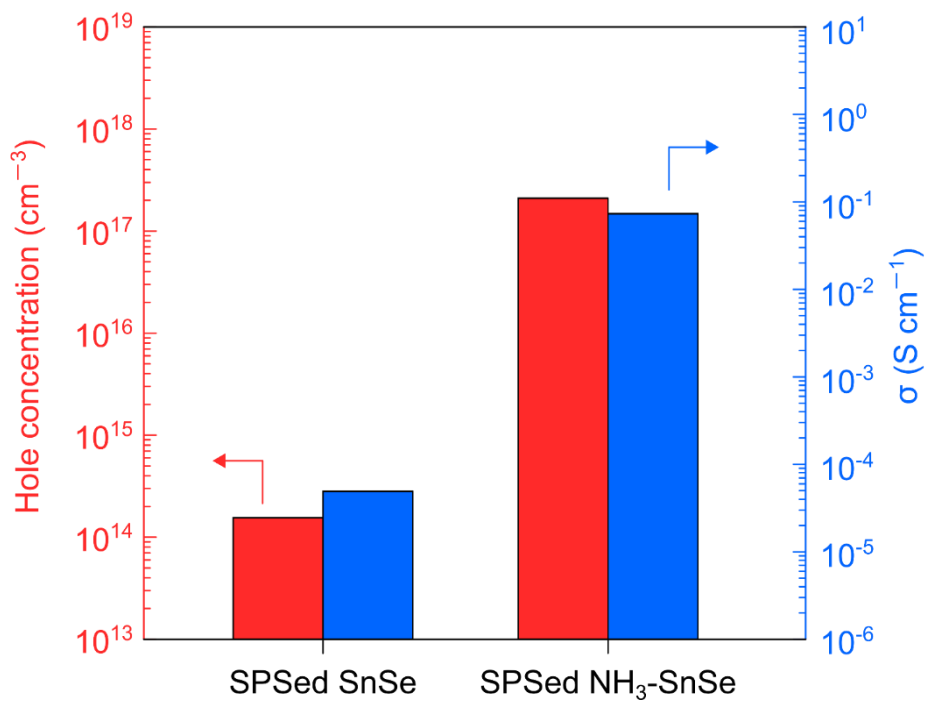


Figure 3.19 Hole concentration and electrical conductivity of SPSed SnSe and NH_3 -SnSe at room temperature.

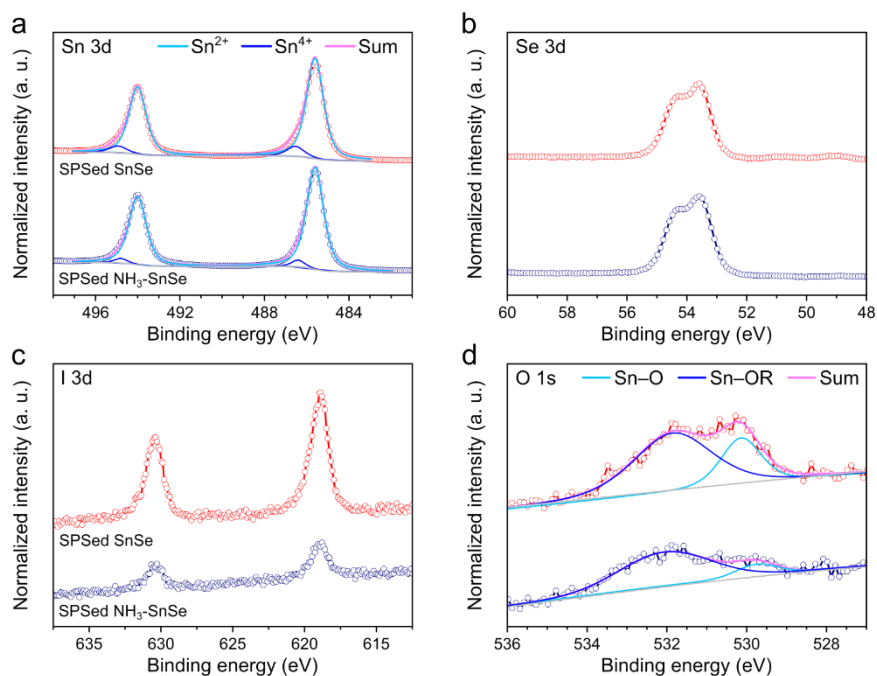


Figure 3.20 The XPS spectra of (a) Sn 3d, (b) Se 3d, (c) I 3d, and (d) O 1s binding energy regions for SPSed SnSe (upper) and SPSed NH₃-SnSe (bottom). R refers to alkyl group and hydrogen in (d). The intensity of XPS spectra is normalized to the peak area of Sn 3d. The surface composition of SPSed SnSe and SPSed NH₃-SnSe is Sn_{1.44}SeO_{0.31}I_{0.06} and Sn_{1.32}SeO_{0.18}I_{0.02}, respectively. The ratio of Sn²⁺ in SPSed SnSe and SPSed NH₃-SnSe is 91% and 95%, respectively.

3.4 Conclusion

In this study, we report on the synthesis, surface treatment, and thermoelectric characterization of dislocation-introduced SnSe nanoplates. Using our current synthetic method, dislocations are produced in the grain and the grain boundary of the SnSe nanoplates. Imperfect oriented attachments during aggregative crystal growth create dislocations in the SnSe nanoplates. Importantly, the use of reactive selenium powders makes it possible to lower the reaction temperature, probably preventing the removal of dislocations in the SnSe nanoplates. Even after the consolidation of SnSe nanoplates, many dislocations are found in SnSe. We also demonstrate that surface treatment with ammonia solution eliminates surface impurities. After the surface treatment, the hole concentration increases in the sintered SnSe nanoplates, resulting in the increase of the electrical conductivity. Various structural elements such as dislocations and mesoscale grains observed in the TEM contribute to ultralow thermal conductivity, and ZT of ~ 1.1 at 873 K is achieved. Our strategy can provide a new pathway to control the structural elements in bulk materials *via* nanochemistry.

3.5 References

- [1] Kovalenko, M. V.; Manna, L.; Cabot, A.; Hens, Z.; Talapin, D. V.; Kagan, C. R.; Klimov, V. I.; Rogach, A. L.; Reiss, P.; Milliron, D. J.; Guyot-Sionnest, P.; Konstantatos, G.; Parak, W. J.; Hyeon, T.; Korgel, B. A.; Murray, C. B.; Heiss, W. *ACS Nano* **2015**, *9*, 1012.
- [2] Talapin, D. V.; Lee, J. S.; Kovalenko, M. V.; Shevchenko, E. V. *Chem. Rev.* **2010**, *110*, 389.
- [3] Ponce, F. A.; Bour, D. P. *Nature* **1997**, *386*, 351.
- [4] Queisser, H. J.; Haller, E. E. *Science* **1998**, *281*, 945.
- [5] Li, X.; Sun, Y.; Xu, J.; Shao, Y.; Wu, J.; Xu, X.; Pan, Y.; Ju, H.; Zhu, J.; Xie, Y. *Nat. Energy* **2019**, *4*, 690.
- [6] Feng, X.; Jiang, K.; Fan, S.; Kanan, M. W. *J. Am. Chem. Soc.* **2015**, *137*, 4606.
- [7] Lounis, S. D.; Runnerstrom, E. L.; Llordes, A.; Milliron, D. J. *J. Phys. Chem. Lett.* **2014**, *5*, 1564.
- [8] Zhang, A.; Zhang, B.; Lu, W.; Xie, D.; Ou, H.; Han, X.; Dai, J.; Lu, X.; Han, G.; Wang, G.; Zhou, X. *Adv. Funct. Mater.* **2018**, *28*, 1705117.
- [9] Li, Z.; Xiao, C.; Zhu, H.; Xie, Y. *J. Am. Chem. Soc.* **2016**, *138*, 14810.
- [10] Zhou, C.; Lee, Y. K.; Cha, J.; Yoo, B.; Cho, S. P.; Hyeon, T.; Chung, I. *J. Am. Chem. Soc.* **2018**, *140*, 9282.

- [11] Jin, Q.; Jiang, S.; Zhao, Y.; Wang, D.; Qiu, J.; Tang, D. M.; Tan, J.; Sun, D. M.; Hou, P. X.; Chen, X. Q.; Tai, K.; Gao, N.; Liu, C.; Cheng, H. M.; Jiang, X. *Nat. Mater.* **2019**, *18*, 62.
- [12] Boles, M. A.; Ling, D.; Hyeon, T.; Talapin, D. V. *Nat. Mater.* **2016**, *15*, 141.
- [13] Yakunin, S.; Dirin, D. N.; Protesescu, L.; Sytnyk, M.; Tollabimazraehno, S.; Humer, M.; Hackl, F.; Fromherz, T.; Bodnarchuk, M. I.; Kovalenko, M. V.; Heiss, W. *ACS Nano* **2014**, *8*, 12883.
- [14] Ning, Z.; Voznyy, O.; Pan, J.; Hoogland, S.; Adinolfi, V.; Xu, J.; Li, M.; Kirmani, A. R.; Sun, J. P.; Minor, J.; Kemp, K. W.; Dong, H.; Rollny, L.; Labelle, A.; Carey, G.; Sutherland, B.; Hill, I.; Amassian, A.; Liu, H.; Tang, J.; Bakr, O. M.; Sargent, E. H. *Nat. Mater.* **2014**, *13*, 822.
- [15] Lee, J. S.; Kovalenko, M. V.; Huang, J.; Chung, D. S.; Talapin, D. V. *Nat. Nanotechnol.* **2011**, *6*, 348.
- [16] Kovalenko, M. V.; Spokoyny, B.; Lee, J. S.; Scheele, M.; Weber, A.; Perera, S.; Landry, D.; Talapin, D. V. *J. Am. Chem. Soc.* **2010**, *132*, 6686.
- [17] Scheele, M.; Oeschler, N.; Veremchuk, I.; Peters, S. O.; Littig, A.; Kornowski, A.; Klinke, C.; Weller, H. *ACS Nano* **2011**, *5*, 8541.
- [18] Ibanez, M.; Korkosz, R. J.; Luo, Z.; Riba, P.; Cadavid, D.; Ortega, S.; Cabot, A.; Kanatzidis, M. G. *J. Am. Chem. Soc.* **2015**, *137*, 4046.

- [19] Park, K.; Ahn, K.; Cha, J.; Lee, S.; Chae, S. I.; Cho, S.-P.; Ryee, S.; Im, J.; Lee, J.; Park, S.-D.; Han, M. J.; Chung, I.; Hyeon, T. *J. Am. Chem. Soc.* **2016**, *138*, 14458.
- [20] Ibanez, M.; Hasler, R.; Genc, A.; Liu, Y.; Kuster, B.; Schuster, M.; Dobrozhan, O.; Cadavid, D.; Arbiol, J.; Cabot, A.; Kovalenko, M. V. *J. Am. Chem. Soc.* **2019**, *141*, 8025.
- [21] Cargnello, M.; Chen, C.; Diroll, B. T.; Doan-Nguyen, V. V.; Gorte, R. J.; Murray, C. B. *J. Am. Chem. Soc.* **2015**, *137*, 6906.
- [22] Brown, P. R.; Kim, D.; Lunt, R. R.; Zhao, N.; Bawendi, M. G.; Grossman, J. C.; Bulovic, V. *ACS Nano* **2014**, *8*, 5863.
- [23] Ibanez, M.; Hasler, R.; Liu, Y.; Dobrozhan, O.; Nazarenko, O.; Cadavid, D.; Cabot, A.; Kovalenko, M. V. *Chem. Mater.* **2017**, *29*, 7093.
- [24] Oh, S. J.; Berry, N. E.; Choi, J. H.; Gauldin, E. A.; Lin, H.; Paik, T.; Diroll, B. T.; Muramoto, S.; Murray, C. B.; Kagan, C. R. *Nano Lett.* **2014**, *14*, 1559.
- [25] Zhang, H.; Kurley, J. M.; Russell, J. C.; Jang, J.; Talapin, D. V. *J. Am. Chem. Soc.* **2016**, *138*, 7464.
- [26] Baumgardner, W. J.; Choi, J. J.; Lim, Y. F.; Hanrath, T. *J. Am. Chem. Soc.* **2010**, *132*, 9519.
- [27] Franzman, M. A.; Schlenker, C. W.; Thompson, M. E.; Brutchey, R.

- L. J. Am. Chem. Soc.* **2010**, *132*, 4060.
- [28] Li, L.; Chen, Z.; Hu, Y.; Wang, X.; Zhang, T.; Chen, W.; Wang, Q. *J. Am. Chem. Soc.* **2013**, *135*, 1213.
- [29] Zhao, L. D.; Lo, S. H.; Zhang, Y. S.; Sun, H.; Tan, G. J.; Uher, C.; Wolverton, C.; Dravid, V. P.; Kanatzidis, M. G. *Nature* **2014**, *508*, 373.
- [30] Chandra, S.; Banik, A.; Biswas, K. *Acs Energy Lett.* **2018**, *3*, 1153.
- [31] Penn, R. L.; Banfield, J. F. *Science* **1998**, *281*, 969.
- [32] Yokoyama, T.; Cao, D. H.; Stoumpos, C. C.; Song, T. B.; Sato, Y.; Aramaki, S.; Kanatzidis, M. G. *J. Phys. Chem. Lett.* **2016**, *7*, 776.
- [33] Zhao, L. D.; Lo, S. H.; Zhang, Y.; Sun, H.; Tan, G.; Uher, C.; Wolverton, C.; Dravid, V. P.; Kanatzidis, M. G. *Nature* **2014**, *508*, 373.
- [34] Vaughn, D. D., 2nd; In, S. I.; Schaak, R. E. *ACS Nano* **2011**, *5*, 8852.
- [35] Baranov, D.; Lynch, M. J.; Curtis, A. C.; Carollo, A. R.; Douglass, C. R.; Mateo-Tejada, A. M.; Jonas, D. M. *Chem. Mater.* **2019**, *31*, 1223.
- [36] Schliehe, C.; Juarez, B. H.; Pelletier, M.; Jander, S.; Greshnykh, D.; Nagel, M.; Meyer, A.; Foerster, S.; Kornowski, A.; Klinke, C.; Weller, H. *Science* **2010**, *329*, 550.
- [37] Yuk, J. M.; Park, J.; Ercius, P.; Kim, K.; Hellebusch, D. J.; Crommie, M. F.; Lee, J. Y.; Zettl, A.; Alivisatos, A. P. *Science* **2012**, *336*, 61.
- [38] Ondry, J. C.; Hauwiller, M. R.; Alivisatos, A. P. *ACS Nano* **2018**, *12*,

3178.

- [39] van Huis, M. A.; Kunneman, L. T.; Overgaag, K.; Xu, Q.; Pandraud, G.; Zandbergen, H. W.; Vanmaekelbergh, D. *Nano Lett.* **2008**, *8*, 3959.
- [40] Tsai, M. H.; Chen, S. Y.; Shen, P. *Nano Lett.* **2004**, *4*, 1197.
- [41] Zhang, Z.; Sheng, H.; Wang, Z.; Gludovatz, B.; Zhang, Z.; George, E. P.; Yu, Q.; Mao, S. X.; Ritchie, R. O. *Nat. Commun.* **2017**, *8*, 14390.
- [42] Chen, Z.; Ge, B.; Li, W.; Lin, S.; Shen, J.; Chang, Y.; Hanus, R.; Snyder, G. J.; Pei, Y. *Nat. Commun.* **2017**, *8*, 13828.
- [43] Mitzi, D. B. *Adv. Mater.* **2009**, *21*, 3141.
- [44] Scheele, M.; Oeschler, N.; Veremchuk, I.; Reinsberg, K. G.; Kreuziger, A. M.; Kornowski, A.; Broekaert, J.; Klinke, C.; Weller, H. *ACS Nano* **2010**, *4*, 4283.
- [45] Heo, S. H.; Jo, S.; Kim, H. S.; Choi, G.; Song, J. Y.; Kang, J. Y.; Park, N. J.; Ban, H. W.; Kim, F.; Jeong, H.; Jung, J.; Jang, J.; Lee, W. B.; Shin, H.; Son, J. S. *Nat. Commun.* **2019**, *10*, 864.
- [46] de Kergommeaux, A.; Faure-Vincent, J.; Pron, A.; de Bettignies, R.; Malaman, B.; Reiss, P. *J. Am. Chem. Soc.* **2012**, *134*, 11659.
- [47] Zhang, Q.; Chere, E. K.; Sun, J.; Cao, F.; Dahal, K.; Chen, S.; Chen, G.; Ren, Z. *Adv. Energy Mater.* **2015**, *5*, 1500360.
- [48] Tian, R.; Zhang, Y.; Chen, Z.; Duan, H.; Xu, B.; Guo, Y.; Kang, H.;

- Li, H.; Liu, H. *Sci. Rep.* **2016**, *6*, 19195.
- [49] Sperling, R. A.; Rivera Gil, P.; Zhang, F.; Zanella, M.; Parak, W. J. *Chem. Soc. Rev.* **2008**, *37*, 1896.
- [50] Wang, Z.; Fan, C.; Shen, Z.; Hua, C.; Hu, Q.; Sheng, F.; Lu, Y.; Fang, H.; Qiu, Z.; Lu, J.; Liu, Z.; Liu, W.; Huang, Y.; Xu, Z. A.; Shen, D. W.; Zheng, Y. *Nat. Commun.* **2018**, *9*, 47.
- [51] Cha, J.; Zhou, C.; Lee, Y. K.; Cho, S. P.; Chung, I. *ACS Appl. Mater. Interfaces* **2019**, *11*, 21645.
- [52] Wei, W.; Chang, C.; Yang, T.; Liu, J.; Tang, H.; Zhang, J.; Li, Y.; Xu, F.; Zhang, Z.; Li, J. F.; Tang, G. *J. Am. Chem. Soc.* **2018**, *140*, 499.
- [53] Chandra, S.; Biswas, K. *J. Am. Chem. Soc.* **2019**, *141*, 6141.
- [54] Biswas, K.; He, J.; Blum, I. D.; Wu, C. I.; Hogan, T. P.; Seidman, D. N.; Dravid, V. P.; Kanatzidis, M. G. *Nature* **2012**, *489*, 414.
- [55] Lee, Y. K.; Ahn, K.; Cha, J.; Zhou, C.; Kim, H. S.; Choi, G.; Chae, S. I.; Park, J. H.; Cho, S. P.; Park, S. H.; Sung, Y. E.; Lee, W. B.; Hyeon, T.; Chung, I. *J. Am. Chem. Soc.* **2017**, *139*, 10887.
- [56] Lee, Y. K.; Luo, Z.; Cho, S. P.; Kanatzidis, M. G.; Chung, I. *Joule* **2019**, *3*, 719.

Bibliography

1. International Publications

- 1) Donghee Son, **Sue In Chae**, Myungbin Kim, Moon Kee Choi, Jiwoong Yang, Kunsu Park, Vinayak S. Kale, Ja Hoon Koo, Changsoon Choi, Minbaek Lee, Ji Hoon Kim, Taeghwan Hyeon, Dae-Hyeong Kim,
"Colloidal Synthesis of Uniform-Sized Molybdenum Disulfide Nanosheets for Wafer-Scale Flexible Nonvolatile Memory"
Advanced Materials **2016**, 28, 9326.
- 2) **Sue In Chae**, Joonil Cha, Sanghwa Lee, Hogeun Chang, Yong Kyu Lee, Sung-Pyo Cho, In Chung, and Taeghwan Hyeon
"Synthesis and Surface Treatment of SnSe Nanoplates for Thermoelectric Application"
Manuscript in Preparations
- 3) Kunsu Park, Kyunghan Ahn, Joonil Cha, Sanghwa Lee, **Sue In Chae**, Sung-Pyo Cho, Siheon Ryee, Jino Im, Jaeki Lee, Su-Dong Park, Myung Joon Han, In Chung, Taeghwan Hyeon,
"Extraordinary Off-Stoichiometric Bismuth Telluride for

Enhanced n-Type Thermoelectric Power Factor”

Journal of the American Chemical Society **2016**, *138*, 14458.

- 4) Vinayak S. Kale, Minsik Hwang, Hogeun Chang, Jeongmin Kang, **Sue In Chae**, Youngmoo Jeon, Jiwoong Yang, Jonghoon Kim, Yoon-Joo Ko, Yuanzhe Piao, Taeghwan Hyeon,

“Microporosity-Controlled Synthesis of Heteroatom Codoped Carbon Nanocages by Wrap-Bake-Sublime Approach for Flexible All-Solid-State-Supercapacitors”

Advanced Functional Materials **2018**, *28*, 1803786.

- 5) Vinayak S. Kale, Uk Sim, Jiwoong Yang, Kyoungsuk Jin, **Sue In Chae**, Woo Je Chang, Arun Kumar Sinha, Heonjin Ha, Chancuk Hwang, Junghyun An, Hyo-Ki Hong, Zonghoon Lee, Ki Tae Nam, Taeghwan Hyeon,

“Sulfur-Modified Graphitic Carbon Nitride Nanostructures as an Efficient Electrocatalyst for Water Oxidation”

Small **2017**, *13*, 1603893.

- 6) Yong Kyu Lee, Kyunghan Ahn, Joonil Cha, Chongjian Zhou, Hyo Seok Kim, Garam Choi, **Sue In Chae**, Jae-Hyuk Park, Sung-Pyo Cho, Sang Hyun Park, Yung-Eun Sung, Won Bo Lee, Taeghwan Hyeon, In Chung,

“Enhancing p-Type Thermoelectric Performances of Polycrystalline SnSe via Tuning Phase Transition Temperature”
Journal of the American Chemical Society **2017**, *139*, 10887.

- 7) Hogeun Chang, Byung Hyo Kim, Hu Young Jeong, Jeong Hee Moon, Minwoo Park, Kwangsoo Shin, **Sue In Chae**, Jisoo Lee, Taegyung Kang, Back Kyu Choi, Jiwoong Yang, Megalamane S. Bootharaju, Hyoin Song, Seong Hee An, Kyung Man Park, Joo Yeon Oh, Hoonkyung Lee, Myung Soo Kim, Jungwon Park, Taeghwan Hyeon,

“Molecular-Level Understanding of Continuous Growth from Iron-Oxo Clusters to Iron Oxide Nanoparticles”
Journal of the American Chemical Society **2019**, *141*, 7037.

- 8) Moon Kee Choi, Jiwoong Yang, Kwanghun Kang, Dong Chan Kim, Changsoon Choi, Chaneui Park, Seok Joo Kim, **Sue In Chae**, Tae-Ho Kim, Ji Hoon Kim, Taeghwan Hyeon, Dae-Hyeong Kim,

“Wearable red–green–blue quantum dot light-emitting diode array using high-resolution intaglio transfer printing”
Nature Communications **2015**, *6*, 7149.

- 9) Euiyeon Jung, Yuwon Park, Kunsu Park, Mi-Sook Kwon,

Mihyun Park, Arun Kumar Sinha, Byoung-Hoon Lee, Jiheon Kim, Hyeon Seok Lee, **Sue In Chae**, Sung-Pyo Cho, Kyu Tae Lee, Taeghwan Hyeon,

“Synthesis of nanostructured $P2-Na_{2/3}MnO_2$ for high performance sodium-ion batteries”

Chemical Communications **2019**, 55, 4757.

2. International Conference

1) **Sue In Chae**, Taeghwan Hyeon

“Colloidal Synthesis and Integration of Uniform-sized Molybdenum Disulfide Nanosheets for Wafer-scale Nonvolatile Memory”

The 2017 MRS Fall Meeting, Boston, U.S.A., November 26-December 1, 2017. (Post Presentation Award, 2nd place)

2) **Sue In Chae**, Taeghwan Hyeon

“Colloidal Synthesis of Molybdenum Disulfide Nanosheets for Nonvolatile Resistive Memory Device”

Nano Korea, KINTEX, Ilsan, Korea, July 12-14, 2017.

3) Kunsu Park, **Sue In Chae**, Sanghwa Lee, In Chung, Taeghwan

Hyeon

“Synthesis of Doped Bismuth Telluride for Enhanced Thermoelectric Performance”

Materials Challenges in Alternative and Renewable Energy Conference (MCARE) 2017, LOTTE Hotel, Jeju, Korea, February 20-24, 2017. (Best Poster Award, Bronze)

초 록

이차원 나노 물질은 그것이 갖는 독특한 특성으로 인해서 다양한 분야의 연구자들에게 큰 관심을 받고 있다. 최근에, 콜로이드 화학을 이용하여 이차원 반도체 나노 물질을 합성하는 방법에 대한 연구가 보고되고 있다. 이 학위 논문에서는 콜로이드 화학을 통한 이차원 나노 구조의 이황화 몰리브데넘 (MoS_2)와 셀레늄화 주석 (SnSe)을 대용량 합성을 다루었으며, 이를 각각 메모리 소자와 열전 재료로 응용 및 분석한 결과에 대하여 논의하였다.

첫 번째로, 균일한 크기의 MoS_2 나노면을 콜로이드 화학을 통한 대용량 합성에 대한 연구를 진행하였으며, 이 나노면을 이용해서 유연한 저항 랜덤 액세스 메모리 (RRAM) 어레이의 집적에 대해 논의하였다. 합성된 MoS_2 나노면은 비교군인 박리를 통해 얻은 MoS_2 보다 훨씬 작은 크기 및 두께 분포를 가짐으로써 균일한 크기 및 두께 성질을 보였다. 게다가 합성된 MoS_2 나노면의 콜로이드 안정성과 합성법의 높은 재현성에 의해 메모리 소재의 용액 기반 공정이 가능하였다. 합성된 MoS_2 나노면 기반의 RRAM은 박리된 MoS_2 기반의 RRAM에 비해 약 10000 배 높은 on/off 전류 비율을 보였다. 더욱이 콜로이드 MoS_2 나노면의 균일성은 대면적의 RRAM 어레이를 가능케 하

였으며 유연한 소자의 제조를 하는데 기여를 했다.

두 번째로, 전위 (dislocation)을 갖는 SnSe 나노판의 합성 및 표면 처리와 열전 성능 분석에 대하여 연구하였다. 간단한 용액 합성을 통해 SnSe 나노판에 전위를 형성시킬 수 있었다. spark plasma sintering에 의한 소결 과정 거친 SnSe의 그레인 내부에서 많은 전위가 존재하는 것을 투과 전자 현미경을 통해 확인하였다. 또한, 암모니아 용액을 통한 표면처리는 나노판의 표면에 남아있는 긴 유기 리간드, 요오드화 리간드와 원하지 않는 표면 산화물들을 효과적으로 제거하였다. 이로 인해 정공의 농도가 증가하였으며, 소결된 펠렛의 전기전도도가 향상하였다. 소결된 벌크 물질의 독특한 나노 구조에 의해 매우 낮은 격자 열전도도 ($\sim 0.23 \text{ W m}^{-1} \text{ K}^{-1}$)를 보였으며, 이는 873 K에서 1.1의 높은 열전 성능 지수 ZT 를 달성하는데 도움을 주었다.

주요 단어: MoS₂, 나노면, RRAM, SnSe, 나노판, dislocations, 표면 처리, 열전 성질.

학번: 2012-23981